

Technical Design Report for:

The Forward Straw Tube Tracker
of

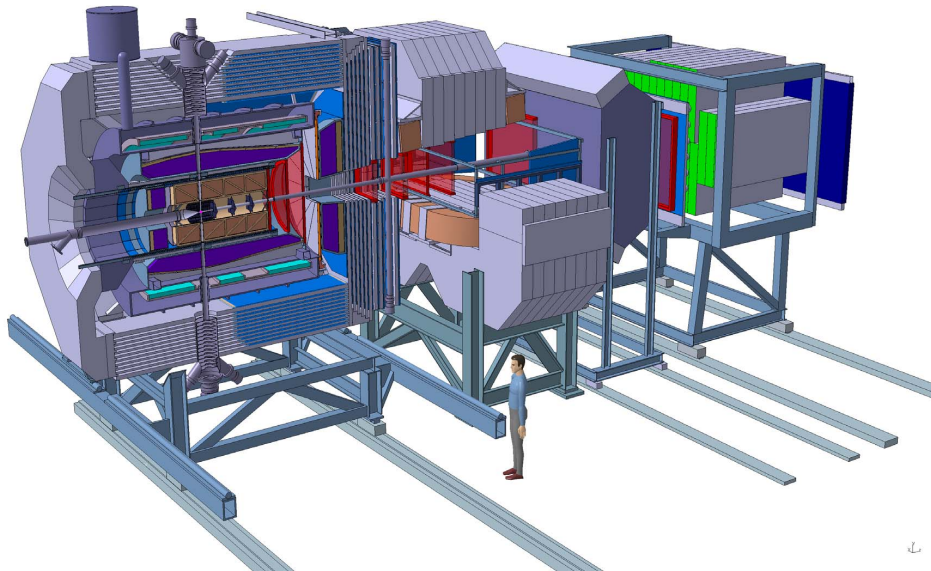
$\bar{\text{P}}\text{ANDA}$ Experiment

(AntiProton Annihilations at Darmstadt)

Strong Interaction Studies with Antiprotons

$\bar{\text{P}}\text{ANDA}$ Collaboration

February 15, 2012



The \overline{P} ANDA Collaboration

Universität **Basel**, Switzerland

W. Erni, I. Keshelashvili, B. Krusche, M. Steinacher

Institute of High Energy Physics, Chinese Academy of Sciences, **Beijing**, China

Y. Heng, Z. Liu, H. Liu, X. Shen, Q. Wang, H. Xu

Universität **Bochum**, I. Institut für Experimentalphysik, Germany

A. Aab, M. Albrecht, J. Becker, A. Csapó, F. Feldbauer, M. Fink, P. Friedel, F.H. Heinsius, T. Held,
L. Klask, H. Koch, B. Kopf, S. Leiber, M. Leyhe, C. Motzko, M. Pelizäus, J. Pychy, B. Roth,
T. Schröder, J. Schulze, C. Sowa, M. Steinke, T. Triffterer, U. Wiedner, J. Zhong

Rheinische Friedrich-Wilhelms-Universität **Bonn**, Germany

R. Beck, S. Bianco, K.T. Brinkmann, C. Hammann, F. Hinterberger, D. Kaiser, R. Kliemt, M. Kube,
A. Pitka, T. Quagli, C. Schmidt, R. Schmitz, R. Schnell, U. Thoma, P. Vlasov, D. Walther, C. Wendel,
T. Würschig, H.G. Zaunick

Università di **Brescia**, Italy

A. Bianconi

Institutul National de C&D pentru Fizica si Inginerie Nucleara "Horia Hulubei", **Bukarest-Magurele**,
Romania

M. Bragadireanu, M. Caprini, D. Pantea, D. Pantelica, D. Pietreanu, L. Serbina, P.D. Tarta

IIT, Illinois Institute of Technology, **Chicago**, U.S.A.

D. Kaplan

AGH, University of Science and Technology, **Cracow**, Poland

T. Fiutowski, M. Idzik, B. Mindur, D. Przyborowski, K. Swientek

IFJ, Institute of Nuclear Physics PAN, **Cracow**, Poland

B. Czech, M. Kistryn, S. Kliczewski, A. Kozela, P. Kulesa, P. Lebiedowicz, K. Pysz, W. Schäfer,
R. Siudak, A. Szczurek

Instytut Fizyki, Uniwersytet Jagiellonski, **Cracow**, Poland

S. Jowzaee, M. Kajetanowicz, B. Kamys, S. Kistryn, G. Korcyl, K. Korcyl, W. Krzemien, A. Magiera,
P. Moskal, M. Palka, Z. Rudy, P. Salabura, J. Smyrski, A. Wrońska

Gesellschaft für Schwerionenforschung GmbH, **Darmstadt**, Germany

M. Al-Turany, R. Arora, I. Augustin, H. Deppe, H. Flemming, A. Gerhardt, K. Götz, A.F. Jordi,
G. Kalicy, R. Karabowicz, D. Lehmann, B. Lewandowski, J. Lühning, F. Maas, H. Orth, M. Patsyuk,
K. Peters, T. Saito, G. Schepers, C.J. Schmidt, L. Schmitt, C. Schwarz, J. Schwiening, B. Voss,
P. Wiczorek, A. Wilms, M. Zühlsdorf

Veksler-Baldin Laboratory of High Energies (VBLHE), Joint Institute for Nuclear Research. **Dubna**,
Russia

V.M. Abazov, G. Alexeev, A. Arefiev, V.I. Astakhov, M.Yu. Barabanov, B.V. Batyunya, Yu.I. Davydov,
V.Kh. Dodokhov, A.A. Efremov, A.G. Fedunov, A.A. Festchenko, A.S. Galoyan, S. Grigoryan,
A. Karmakov, E.K. Koshurnikov, V.I. Lobanov, Yu.Yu. Lobanov, A.F. Makarov, L.V. Malinina,
V.L. Malyshev, G.A. Mustafaev, A. Olshevskiy, M.A. Pasyuk, E.A. Perevalova, A.A. Piskun,
T.A. Pocheptsov, G. Pontecorvo, V.K. Rodionov, Yu.N. Rogov, R.A. Salmin, A.G. Samartsev,
M.G. Sapozhnikov, G.S. Shabratova, A.N. Skachkova, N.B. Skachkov, E.A. Stokovsky,
M.K. Suleimanov, R.Sh. Teshev, V.V. Tokmenin, V.V. Uzhinsky, A.S. Vodopyanov, S.A. Zaporozhets,
N.I. Zhuravlev, A.G. Zorin

University of **Edinburgh**, United Kingdom

D. Branford, D. Glazier, D. Watts, P. Woods

Friedrich Alexander Universität **Erlangen-Nürnberg**, Germany

A. Britting, W. Eyrich, A. Lehmann, F. Uhlig

Northwestern University, **Evanston**, U.S.A.

S. Dobbs, Z. Metreveli, K. Seth, A. Tomaradze, T. Xiao

Università di Ferrara and INFN Sezione di Ferrara, **Ferrara**, Italy

D. Bettoni, V. Carassiti, A. Cotta Ramusino, P. Dalpiaz, A. Drago, E. Fioravanti, I. Garzia, M. Savriè,
G. Stancari

INFN Laboratori Nazionali di **Frascati**, Italy

N. Bianchi, P. Gianotti, C. Guaraldo, V. Lucherini, D. Orecchini, E. Pace

INFN Sezione di **Genova**, Italy

A. Bersani, G. Bracco, M. Macri, R.F. Parodi

Justus Liebig-Universität **Gießen**, II. Physikalisches Institut, Germany

D. Bremer, V. Dormenev, P. Drexler, M. Düren, T. Eissner, K. Föhl M. Galuska, T. Gessler,
A. Hayrapetyan, J. Hu, P. Koch, B. Kröck, W. Kühn, S. Lange, Y. Liang, O. Merle, V. Metag,
M. Moritz, D. Münchow, M. Nanova, R. Novotny, B. Spruck, H. Stenzel, T. Ullrich, M. Werner, H. Xu

University of **Glasgow**, United Kingdom

C. Euan, M. Hoek, D. Ireland, T. Keri, R. Montgomery, D. Protopopescu, G. Rosner, B. Seitz

Kernfysisch Versneller Instituut, University of **Groningen**, Netherlands

M. Babai, A. Glazenberg-Kluttig, M. Kavatsyuk, P. Lemmens, M. Lindemulder, H. Löhner,
J. Messchendorp, H. Moeini, P. Schakel, F. Schreuder, H. Smit, G. Tambave, J.C. van der Weele,
R. Veenstra

Fachhochschule Südwestfalen **Iserlohn**, Germany

H. Sohlbach

Forschungszentrum Jülich, Institut für Kernphysik, **Jülich**, Germany

M. Büscher, D. Deermann, R. Dosdall, S. Esch, A. Gillitzer, F. Goldenbaum, D. Grunwald, S. Henssler,
A. Herten, Q. Hu, G. Kemmerling, H. Kleines, A. Lehrach, R. Maier, M. Mertens, H. Ohm, D. Prasuhn,
T. Randriamalala, J. Ritman, S. Schadmand, V. Serdyuk, G. Sterzenbach, T. Stockmanns, P. Wintz,
P. Wüstner, H. Xu

University of Silesia, **Katowice**, Poland

J. Kisiel

Chinese Academy of Science, Institute of Modern Physics, **Lanzhou**, China

S. Li, Z. Li, Z. Sun, H. Xu

INFN Laboratori Nazionali di **Legnaro**, Italy

V. Rigato

Lunds Universitet, Department of Physics, **Lund**, Sweden

S. Fissum, K. Hansen, L. Isaksson, M. Lundin, B. Schröder

Johannes Gutenberg-Universität, Institut für Kernphysik, **Mainz**, Germany

P. Achenbach, S. Bleser, U. Cahit, M. Cardinali, A. Denig, M. Distler, M. Fritsch, D. Kangh,
A. Karavdina, W. Lauth, H. Merkel, M. Michel, M.C. Mora Espi, U. Müller, J. Pochodzalla,
J. Prometheus, S. Sanchez, A. Sanchez-Lorente, S. Schlimme, C. Sfienti, M. Thiel, T. Weber

Research Institute for Nuclear Problems, Belarus State University, **Minsk**, Belarus

V.I. Dormenev, A.A. Fedorov, M.V. Korzhik, O.V. Missevitch

Institute for Theoretical and Experimental Physics, **Moscow**, Russia

V. Balanutsa, V. Chernetsky, A. Demekhin, A. Dolgolenko, P. Fedorets, A. Gerasimov, V. Goryachev,
V. Varentsov

Moscow Power Engineering Institute, **Moscow**, Russia

A. Boukharov, O. Malyshev, I. Marishev, A. Semenov

Technische Universität **München**, Germany

F. Böhmer, S. Dörheim, B. Ketzer, I. Konorov, S. Paul

Westfälische Wilhelms-Universität **Münster**, Germany
A.K. Hergemöller, A. Khoukaz, E. Köhler, A. Täschner, J. Wessels

IIT Bombay, Department of Physics, **Mumbai**, India
R. Varma

Bhabha Atomic Research Center, **Mumbai**, India
A. Chatterjee, V. Jha, S. Kailas, B. Roy

Suranaree University of Technology, **Nakhon Ratchasima**, Thailand
Y. Yan, K. Chinorat, K. Khanchai, L. Ayut, S. Pomrad

Budker Institute of Nuclear Physics of Russian Academy of Science, **Novosibirsk**, Russia
E. Baldin, K. Kotov, S. Peleganchuk, Yu. Tikhonov

Institut de Physique Nucléaire, **Orsay**, France
J. Boucher, V. Chambert, A. Dbeyssi, T. Hennino, M. Imre, R. Kunne, C. Le Galliard, B. Ma,
D. Marchand, A. Maroni, S. Ong, B. Ramstein, P. Rosier, M. Sudol, E. Tomasi-Gustafsson,
J. Van de Wiele

Dipartimento di Fisica Nucleare e Teorica, Università di Pavia, INFN Sezione di Pavia, **Pavia**, Italy
G. Boca, A. Braghieri, S. Costanza, P. Genova, L. Lavezzi, P. Montagna, A. Rotondi

Institute for High Energy Physics, **Protvino**, Russia
V. Abramov, N. Belikov, A. Davidenko, A. Derevschikov, Y. Goncharenko, V. Grishin, V. Kachanov,
D. Konstantinov, V. Kormilitsin, Y. Melnik, A. Levin, N. Minaev, V. Mochalov, D. Morozov, L. Nogach,
S. Poslavskiy, A. Ryazantsev, S. Ryzhikov, P. Semenov, I. Shein, A. Uzunian, A. Vasiliev, A. Yakutin

Kungliga Tekniska Höskolan, **Stockholm**, Sweden
T. Bäck, B. Cederwall

Stockholms Universitet, **Stockholm**, Sweden
K. Makónyi, P.E. Tegnér, K.M. von Würtemberg

Petersburg Nuclear Physics Institute of Russian Academy of Science, Gatchina, **St. Petersburg**, Russia
S. Belostotski, G. Gavrillov, A. Itzotov, A. Kashchuk, A. Kisselev, P. Kravchenko, O. Levitskaya,
S. Manaenkov, O. Miklukho, Y. Naryshkin, D. Veretennikov, V. Vikhrov, A. Zhadanov

Università di Torino and INFN Sezione di Torino, **Torino**, Italy
D. Alberto, A. Amoroso, M.P. Bussa, L. Busso, F. De Mori, M. Destefanis, L. Fava, L. Ferrero,
M. Greco, M. Maggiora, S. Marcello, S. Sosio, S. Spataro, L. Zotti

INFN Sezione di Torino, **Torino**, Italy
D. Calvo, S. Coli, P. De Remigis, A. Filippi, G. Giraudo, S. Lusso, G. Mazza, O. Morra, A. Rivetti,
R. Wheadon

Politecnico di Torino and INFN Sezione di Torino, **Torino**, Italy
F. Iazzi, A. Lavagno, H. Younis

Università di Trieste and INFN Sezione di Trieste, **Trieste**, Italy
R. Birsa, F. Bradamante, A. Bressan, A. Martin

Universität Tübingen, **Tübingen**, Germany
H. Clement

The Svedberg Laboratory, **Uppsala**, Sweden
B. Galander

Uppsala Universitet, Institutionen för Strålningsvetenskap, **Uppsala**, Sweden
L. Caldeira Balkestal, H. Calén, K. Fransson, T. Johansson, A. Kupsc, P. Marciniwski, E. Thomé,
M. Wolke, J. Zlomanczuk

Universitat de **Valencia**, Dpto. de Física Atómica, Molecular y Nuclear, Spain
J. Díaz, A. Ortiz

University of Technology, Institute of Atomic Energy Otwock-Swierk, **Warsaw**, Poland
K. Dmowski, R. Korzeniewski, D. Przemyslaw, B. Slowinski

Soltan Institute for Nuclear Studies, **Warsaw**, Poland

A. Chlopik, Z. Guzik, K. Kosinski, D. Melnychuk, A. Wasilewski, M. Wojciechowski, S. Wronka,
A. Wysocka, B. Zwieglinski

Österreichische Akademie der Wissenschaften, Stefan Meyer Institut für Subatomare Physik, **Wien**,
Austria

P. Bühler, O. Hartman, P. Kienle, J. Marton, K. Suzuki, E. Widmann, J. Zmeskal

Editors:	Mauro Savrie Jerzy Smyrski	Email: savrie@fe.infn.it Email: jerzy.smyrski@uj.edu.pl
Technical Coordinator: Deputy:	Lars Schmitt Bernd Lewandowski	Email: l.schmitt@gsi.de Email: b.lewandowski@gsi.de
Physics Coordinator: Deputy:	Diego Bettoni Albrecht Gillitzer	Email: diego.bettoni@fe.infn.it Email: a.gillitzer@fz-juelich.de
Computing coordinator: Deputy:	Johan Messchendorp Stefano Spataro	Email: messchendorp@kvi.nl Email: stefano.spataro@to.infn.it
Spokesperson: Deputy:	Ulrich Wiedner Paola Gianotti	Email: ulrich.wiedner@ruhr-uni-bochum.de Email: paola.gianotti@lnf.infn.it

Preface

This document describes the technical layout and the expected performance of the Forward Tracker (FT) of the $\overline{\text{PANDA}}$ experiment. This is one of the detectors that constitute the $\overline{\text{PANDA}}$ charged particle tracking system, a composite layout that includes different sub-detectors in the Target and in the Forward Spectrometer. The FT will detect charged particles emitted at the most forward angles covered by the Forward Spectrometer reconstructing their trajectories and momenta. Design choices and test measurements are here discussed and compared with Monte Carlo simulations. The road map for the detector realisation is outlined.

The use of registered names, trademarks, *etc.* in this publication does not imply, even in the absence of specific statement, that such names are exempt from the relevant laws and regulations and therefore free for general use.

Contents

Preface	vii	4.2.3	Analog front-end electronics . . .	37
		4.2.4	Time-to-digit converters	40
1 The $\bar{\text{PANDA}}$ Experiment and its Tracking Concept	1	4.3	Data rate	43
1.1 The $\bar{\text{PANDA}}$ Experiment	1	4.4	The power systems	45
1.1.1 The Scientific Program	2	4.4.1	High-voltage system	45
1.1.2 High Energy Storage Ring – HESR	4	4.4.2	Low-voltage system	45
1.1.3 Targets	6	4.5	Detector integration	46
1.1.4 Luminosity Considerations	7	4.5.1	Mechanical supports	46
1.2 The $\bar{\text{PANDA}}$ Detector	11	4.5.2	Cables routing	46
1.2.1 Target Spectrometer	11	4.5.3	Gas tubes routing	46
1.2.2 Forward Spectrometer	15	4.5.4	Installation and alignment	46
1.2.3 Data Acquisition	17	4.5.5	Access	46
1.2.4 Infrastructure	17	4.6	Monitoring	47
1.3 The Charged Particle Tracking System	18	5 Tests of prototypes		48
1.3.1 Basic Approach	18	5.1	Jülich small-scale setup	48
1.3.2 Optimisation Criteria	18	5.1.1	Experimental setup	48
References	22	5.1.2	Spatial resolution	48
2 Overview of the Forward Tracker	24	5.1.3	Single tube resolution	50
2.1 Basic requirements and performance goals	24	5.1.4	Contribution of tubes mispositioning to spatial resolution . . .	50
2.2 General layout	25	5.1.5	Detector performance at high counting rates	51
2.2.1 Straw tube description	25	5.1.6	Aging tests	52
2.2.2 Straw tube module	29	5.2	The COSY-TOF Straw Tube Tracker	57
2.2.3 Layer arrangement	29	5.3	Ferrara prototype modules	60
3 Construction of tracking stations	31	5.4	Krakow prototype module	61
3.1 Tracking stations before the dipole magnet	31	5.4.1	Construction	61
3.2 Tracking stations inside the dipole magnet gap	32	5.4.2	Tests with radioactive sources . .	61
3.3 Tracking stations after the dipole magnet	33	5.5	Summary and conclusions	63
4 Infrastructure	34	6 Computer simulations and expected performance		64
4.1 The gas system	34	6.1	The single straw tube simulation . . .	64
4.2 The readout electronics	36	6.1.1	The charge released into the tube	64
4.2.1 Requirements	36	6.1.2	The drift process from GARFIELD	64
4.2.2 General concept	36	6.1.3	Simulation of the drift process . .	66
		6.1.4	The electrical signal	66

6.1.5	Simulation of the self-calibration procedure	67
6.1.6	Full and fast simulation	68
6.1.7	Performance in magnetic field . .	68
6.2	Simulation and reconstruction software	71
6.3	Track and momentum reconstruction	72
6.4	Optimization of the tracking system .	73
6.5	Physics channels analysis	74
7	Organization	75
7.1	Production logistics	75
7.1.1	Production of straws	75
7.1.2	Assembly of straw tube modules and detection layers	75
7.1.3	Quality control	75
7.2	Work-packages	76
7.3	Timelines	77
8	Appendices	78
.1	Description of geometry of tracking stations	78
	References	82
	Acknowledgements	83
	List of Acronyms	85
	List of Figures	87
	List of Tables	91

1 The $\bar{\text{P}}\text{ANDA}$ Experiment and its Tracking Concept

The following sections contain a general introduction to the $\bar{\text{P}}\text{ANDA}$ experiment and, in particular, a short description of the implemented overall tracking concept. They belong to a common introductory part for the volumes of all individual tracking systems.

1.1 The $\bar{\text{P}}\text{ANDA}$ Experiment

The $\bar{\text{P}}\text{ANDA}$ (AntiProton ANnihilation at DArmstadt) experiment [?] is one of the key projects at the future Facility for Antiproton and Ion Research (FAIR) [?][?], which is currently under construction at GSI, Darmstadt. For this new facility the present GSI accelerators will be upgraded and further used as injectors. The completed accelerator facility will feature a complex structure of new accelerators and storage rings. An overview of the FAIR facility is given in Fig. 1.1. Further details of the accelerator complex are described in [?]. The FAIR accelerators will deliver primary proton and ion beams as well as secondary beams of antiprotons or radioactive ions, all with high energy, high intensity and high quality. Experiments to be installed at the facility will address a wide range of physics topics in the fields of nuclear and hadron physics as well as in atomic and plasma physics. An executive summary of the main FAIR projects can be found in [?] and [?].

The $\bar{\text{P}}\text{ANDA}$ experiment will perform precise studies of antiproton-proton annihilations and reactions of antiprotons with nucleons of heavier nuclear targets. It will benefit from antiproton beams with unprecedented intensity and quality. The covered centre-of-mass energy between 2.3 GeV and 5.5 GeV allows for very accurate measurements, especially in the charm quark sector. Based on a broad physics program, studying the non-perturbative regime, it will be possible to explore the nature of the strong interaction and to obtain a significant progress in our understanding of the QCD spectrum and hadron structure.

Nowadays these studies are carried out mainly at electron machines that offer the advantage of kinematically clean reactions but at the price of a reduced set of final states and reduced cross-sections.

Also the future experiments currently planned as upgrade at existing high-energy physics facilities will not deliver high-precision data over the full charm spectrum. In this context, the $\bar{\text{P}}\text{ANDA}$ experiment will be a unique tool to improve both statistics and precision of existing data and to further explore the physics in the charm quark sector. Moreover, the $\bar{\text{P}}\text{ANDA}$ collaboration is in the ideal situation to be able to benefit from the expertise gained during the construction of the LHC detectors and of the B-factory experiments, which have determined a significant progress in the detector technology due to the performed optimisation or the introduction of completely new concepts and instruments.

In the first section of this chapter the scientific program of $\bar{\text{P}}\text{ANDA}$ will be summarised. It ranges from charmonium spectroscopy to the search for exotic hadrons and the study of nucleon structure, from the study of in-medium modifications of hadron masses to the physics of hypernuclei. Therefore, antiproton beams in the momentum range from 1.5 GeV/c to 15 GeV/c will be provided by the high-energy storage ring (HESR) to the experiment. An overview of this accelerator and storage ring will be given in the second section. To explore the broad physics program, the $\bar{\text{P}}\text{ANDA}$ collaboration wants to build a state-of-the-art general purpose detec-

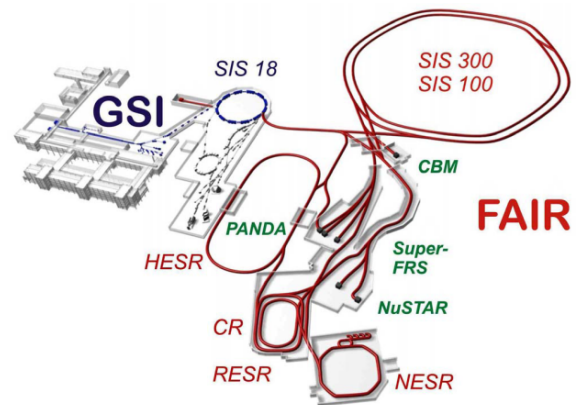


Figure 1.1: Overview of the future FAIR facility. The upgraded accelerators of the existing GSI facility will act as injectors. New accelerator and storage rings are highlighted in red, experimental sites are indicated with green letters.

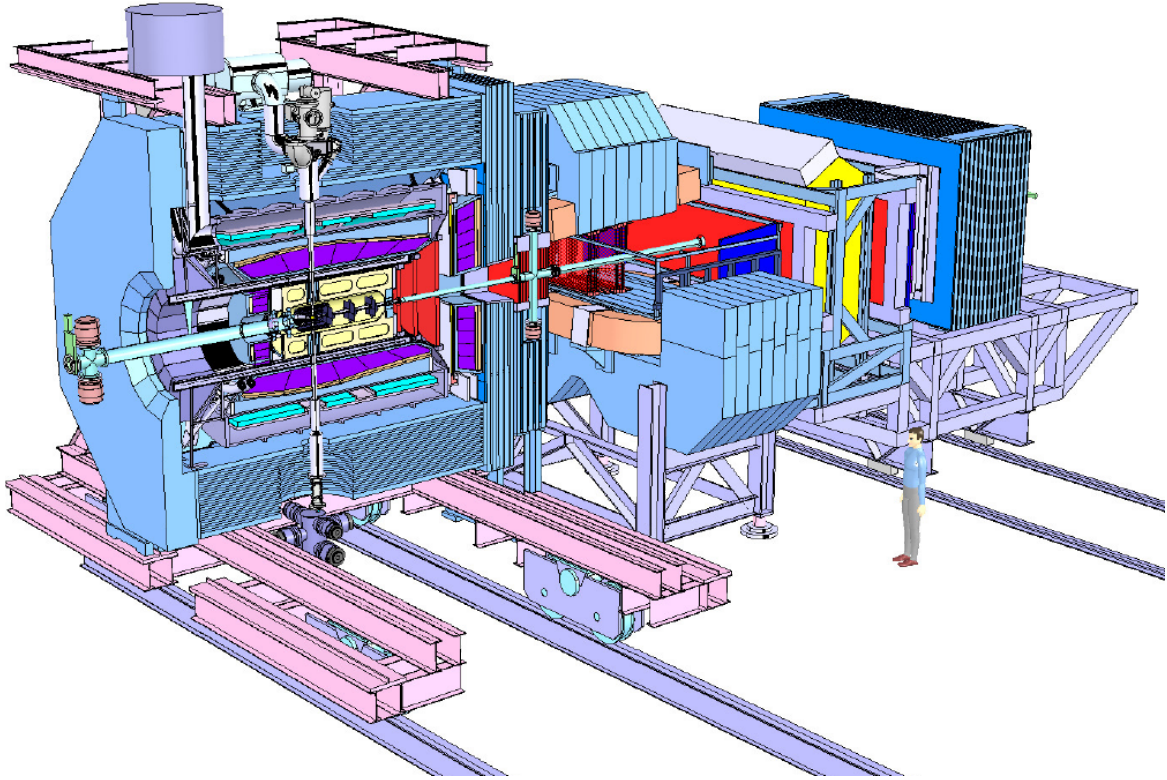


Figure 1.2: Layout of the \bar{P} ANDA detector consisting of a Target Spectrometer, surrounding the interaction region, and a Forward Spectrometer to detect particles emitted in the forward region. The HESR antiproton beam enters the apparatus from the left side.

tor studying annihilation reactions of antiprotons with protons ($\bar{p}p$) and in nuclear matter ($\bar{p}A$). The different target systems will be discussed in section 1.1.3. The \bar{P} ANDA apparatus consists of a set of systems surrounding an internal target placed in one of the two straight sections of the HESR. Fig. 1.2 shows the layout of the \bar{P} ANDA detector. It consists of a 4 m long and 2 T strong superconducting solenoid instrumented to detect both charged and neutral particles emitted at large and backward angles (Target Spectrometer, TS) and of a 2 Tm resistive dipole magnetic spectrometer to detect charged and neutral particles emitted at angles between zero and twenty degrees (Forward Spectrometer, FS) with respect to the beam axis. A complex detector arrangement is necessary in order to reconstruct the complete set of final states, relevant to achieve the proposed physics goals. With the installed setup, a good particle identification with an almost complete solid angle will be combined with excellent mass, momentum and spatial resolution. More details of the \bar{P} ANDA detector will be described in section 1.2.

1.1.1 The Scientific Program

One of the most challenging and fascinating goals of modern physics is the achievement of a fully quantitative understanding of the strong interaction, which is the subject of hadron physics. Significant progress has been achieved over the past few years thanks to considerable advances in experiment and theory. New experimental results have stimulated a very intense theoretical activity and a refinement of the theoretical tools.

Still there are many fundamental questions which remain basically unanswered. Phenomena such as the confinement of quarks, the existence of glueballs and hybrids, the origin of the masses of hadrons in the context of the breaking of chiral symmetry are long-standing puzzles and represent the intellectual challenge in our attempt to understand the nature of the strong interaction and of hadronic matter.

Experimentally, studies of hadron structure can be performed with different probes such as electrons, pions, kaons, protons or antiprotons. In antiproton-proton annihilation, particles with gluonic degrees

of freedom as well as particle-antiparticle pairs are copiously produced, allowing spectroscopic studies with very high statistics and precision. Therefore, antiprotons are an excellent tool to address the open problems.

The $\bar{\text{PANDA}}$ experiment is being designed to fully exploit the extraordinary physics potential arising from the availability of high-intensity, cooled antiproton beams. Main experiments of the rich and diversified hadron physics program are briefly itemised in the following. More details can be found in the $\bar{\text{PANDA}}$ physics booklet [?].

- **Charmonium Spectroscopy**

A precise measurement of all states below and above the open charm threshold is of fundamental importance for a better understanding of QCD. All charmonium states can be formed directly in $\bar{p}p$ annihilation. At full luminosity $\bar{\text{PANDA}}$ will be able to collect several thousand $c\bar{c}$ states per day. By means of fine scans it will be possible to measure masses with accuracies of the order of 100 keV and widths to 10% or better. The entire energy region below and above the open charm threshold will be explored.

- **Search for Gluonic Excitations**

One of the main challenges of hadron physics is the search for gluonic excitations, i.e. hadrons in which the gluons can act as principal components. These gluonic hadrons fall into two main categories: glueballs, i.e. states of pure glue, and hybrids, which consist of a $q\bar{q}$ pair and excited glue. The additional degrees of freedom carried by gluons allow these hybrids and glueballs to have J^{PC} exotic quantum numbers: in this case mixing effects with nearby $q\bar{q}$ states are excluded and this makes their experimental identification easier. The properties of glueballs and hybrids are determined by the long-distance features of QCD and their study will yield fundamental insight into the structure of the QCD vacuum. Antiproton-proton annihilations provide a very favourable environment in which to look for gluonic hadrons.

- **Study of Hadrons in Nuclear Matter**

The study of medium modifications of hadrons embedded in hadronic matter is aiming at understanding the origin of hadron masses in the context of spontaneous chiral symmetry breaking in QCD and its partial restoration in a hadronic environment. So far experiments have been focussed on the light quark sector. The high-intensity \bar{p} beam of up to 15 GeV/c will al-

low an extension of this program to the charm sector both for hadrons with hidden and open charm. The in-medium masses of these states are expected to be affected primarily by the gluon condensate.

Another study which can be carried out in $\bar{\text{PANDA}}$ is the measurement of J/ψ and D meson production cross sections in \bar{p} annihilation on a series of nuclear targets. The comparison of the resonant J/ψ yield obtained from \bar{p} annihilation on protons and different nuclear targets allows to deduce the J/ψ -nucleus dissociation cross section, a fundamental parameter to understand J/ψ suppression in relativistic heavy ion collisions interpreted as a signal for quark-gluon plasma formation.

- **Open Charm Spectroscopy**

The HESR, running at full luminosity and at \bar{p} momenta larger than 6.4 GeV/c, would produce a large number of D meson pairs. The high yield and the well defined production kinematics of D meson pairs would allow to carry out a significant charmed meson spectroscopy program which would include, for example, the rich D and D_s meson spectra.

- **Hypernuclear Physics**

Hypernuclei are systems in which neutrons or protons are replaced by hyperons. In this way a new quantum number, strangeness, is introduced into the nucleus. Although single and double Λ -hypernuclei were discovered many decades ago, only 6 double Λ -hypernuclei are presently known. The availability of \bar{p} beams at FAIR will allow efficient production of hypernuclei with more than one strange hadron, making $\bar{\text{PANDA}}$ competitive with planned dedicated facilities. This will open new perspectives for nuclear structure spectroscopy and for studying the forces between hyperons and nucleons.

- **Electromagnetic Processes**

In addition to the spectroscopic studies described above, $\bar{\text{PANDA}}$ will be able to investigate the structure of the nucleon using electromagnetic processes, such as Deeply Virtual Compton Scattering (DVCS) and the process $\bar{p}p \rightarrow e^+e^-$, which will allow the determination of the electromagnetic form factors of the proton in the timelike region over an extended q^2 region. Furthermore, measuring the Drell Yan production of muons would give access to the transverse nucleon structure.

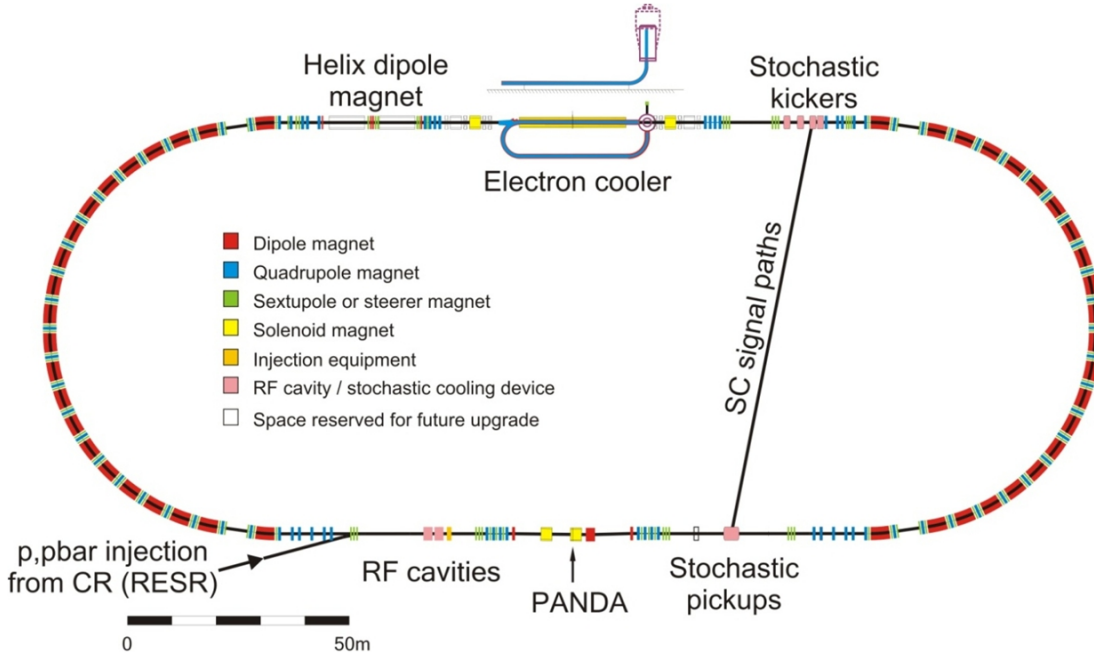


Figure 1.3: Layout of the High Energy Storage Ring HESR. The beam is injected from the left into the lower straight section. The location of the PANDA target is indicated with an arrow.

1.1.2 High Energy Storage Ring – HESR

The HESR is dedicated to supply $\bar{\text{PANDA}}$ with high intensity and high quality antiproton beams over a broad momentum range from 1.5 GeV/c to 15 GeV/c [?]. Table 1.1 summarises the experimental requirements and main parameters of the two operation modes for the full FAIR version. The High Luminosity (HL) and the High Resolution (HR) mode are established to fulfil all challenging specifications for the experimental program of $\bar{\text{PANDA}}$ [?]. The HR mode is defined in the momentum range from 1.5 GeV/c to 9 GeV/c. To reach a relative momentum spread down to the order of 10^{-5} , only 10^{10} circulating particles in the ring are anticipated. The HL mode requires an order of magnitude higher beam intensity with reduced momentum resolution to reach a peak luminosity of $2 \cdot 10^{32} \text{cm}^{-2} \text{s}^{-1}$ in the full momentum range up to 15 GeV/c. To reach these beam parameters a very powerful phase-space cooling is needed. Therefore, high-energy electron cooling [?] and high-bandwidth stochastic cooling [?] will be utilised.

The HESR lattice is designed as a racetrack shaped ring with a maximum beam rigidity of 50 Tm (see Fig. 1.3). It consists of two 180° arcs and two 155 m long straight sections with a total circumference of 575 m [?]. The arc quadrupole magnets will allow for a flexible adjustment of transition energy, hor-

izontal and vertical betatron tune as well as horizontal dispersion. In the straight section opposite to the injection point, an electron cooler will be installed. The $\bar{\text{PANDA}}$ detector with the internal target is placed at the other side. Further components in the straight $\bar{\text{PANDA}}$ section are beam injection kickers, septa and multi-harmonic RF cavities. The latter allow for a compensation of energy losses due to the beam-target interaction, a bunch rotation and the decelerating or accelerating of the beam. Stochastic cooling is implemented via several kickers and opposing high-sensitivity pick-ups on either side of the straight sections.

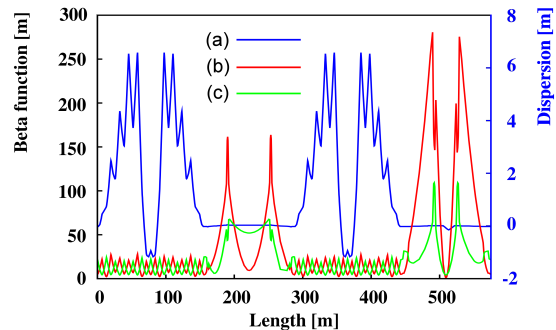


Figure 1.4: Optical functions of the $\gamma_{tr} = 6.2$ lattice: Horizontal dispersion (a), horizontal (b) and vertical (c) betatron function. Electron cooler and target are located at a length of 222 m and 509 m, respectively.

Experimental Requirements	
Ion species	Antiprotons
\bar{p} production rate	$2 \cdot 10^7/\text{s}$ ($1.2 \cdot 10^{10}$ per 10 min)
Momentum / Kinetic energy range	1.5 to 15 GeV/c/ 0.83 to 14.1 GeV
Number of particles	10^{10} to 10^{11}
Betatron amplitude at IP	1 m to 15 m
Betatron amplitude E-Cooler	25 m to 200 m
Operation Modes	
High resolution (HR)	Peak Luminosity of $2 \cdot 10^{31} \text{cm}^{-2} \text{s}^{-1}$ for $10^{10} \bar{p}$ assuming $\rho_{\text{target}} = 4 \cdot 10^{15} \text{atoms/cm}^2$ RMS momentum spread $\sigma_p/p \leq 4 \cdot 10^{-5}$, 1.5 to 8.9 GeV/c
High luminosity (HL)	Peak Luminosity up to $2 \cdot 10^{32} \text{cm}^{-2} \text{s}^{-1}$ for $10^{11} \bar{p}$ assuming $\rho_{\text{target}} = 4 \cdot 10^{15} \text{atoms/cm}^2$ RMS momentum spread $\sigma_p/p \sim 10^{-4}$, 1.5 to 15 GeV/c

Table 1.1: Experimental requirements and operation modes of HESR for the full FAIR version.

Special requirements for the lattice are low dispersion in the straight sections and small betatron amplitudes in the range between 1 m and 15 m at the internal interaction point (IP) of the $\bar{\text{P}}\text{ANDA}$ detector. In addition, the betatron amplitude at the electron cooler must be adjustable within a large range between 25 m and 200 m. Examples of the optical functions for one of the defined optical settings are shown in Fig. 1.4. The deflection of the spectrometer dipole magnet of the $\bar{\text{P}}\text{ANDA}$ detector will be compensated by two dipole magnets that create a beam chicane. These will be placed 4.6 m upstream and 13 m downstream the $\bar{\text{P}}\text{ANDA}$ IP thus defining a boundary condition for the quadrupole elements closest to the experiment. For symmetry reasons, they have to be placed at ± 14 m with respect to the IP. The asymmetric placement of the chicane dipoles will result in the experiment axis occurring at a small angle with respect to the axis of the straight section. The $\bar{\text{P}}\text{ANDA}$ solenoid will be compensated by one solenoid magnet. Additional correction dipoles have to be included around the electron cooler due to the toroids that will be used to overlap the electron beam with the antiproton beam. Phase-space coupling induced by the electron cooler solenoid will be compensated by two additional solenoid magnets.

Closed orbit correction and local orbit bumps at dedicated locations in the ring are crucial to meet requirements for the beam-target interaction in terms of maximised ring acceptance and optimum beam-target overlap [?]. The envisaged scheme aims on a reduction of maximum closed orbit deviations to below 5 mm while not exceeding 1 mrad of corrector strength. Therefore, 64 beam position monitors and 48 orbit correction dipoles are

intended to be used. Because a few orbit bumps will have to be used in the straight parts of the HESR, all correction dipoles therein are designed to provide an additional deflection strength of 1 mrad.

Transverse and longitudinal cooling will be used to compensate a transverse beam blow up and to achieve a low momentum spread, respectively. While stochastic cooling will be applicable in the whole momentum range, electron cooling is foreseen in a range from 1.5 GeV/c to 8.9 GeV/c with a possible upgrade to 15 GeV/c. The relative momentum spread can be further improved by combining both cooling systems. Beam losses are dominated by hadronic interactions between antiprotons and target protons, single large-angle Coulomb scattering in the target and energy straggling induced by Coulomb interactions of the antiprotons with target electrons. Mean beam lifetimes for the HESR range between 1540 s and 7100 s. The given numbers correspond to the time, after which the initial beam intensity is reduced by a factor of $1/e$. A detailed discussion of the beam dynamics and beam equilibria for the HESR can be found in [?, ?, ?, ?]. Advanced simulations have been performed for both cooling scenarios. In case of electron cooled beams the RMS relative momentum spread obtained for the HR mode ranges from $7.9 \cdot 10^{-6}$ (1.5 GeV/c) to $2.7 \cdot 10^{-5}$ (8.9 GeV/c), and $1.2 \cdot 10^{-4}$ (15 GeV/c) [?]. With stochastic cooling in a bandwidth of 2 GHz to 6 GHz, the RMS relative momentum spread for the HR mode results in $5.1 \cdot 10^{-5}$ (3.8 GeV/c), $5.4 \cdot 10^{-5}$ (8.9 GeV/c) and $3.9 \cdot 10^{-5}$ (15 GeV/c) [?]. In the HL mode a RMS relative momentum spread of roughly 10^{-4} can be expected. Transverse stochastic cooling can be adjusted independently to ensure sufficient beam-target overlap.

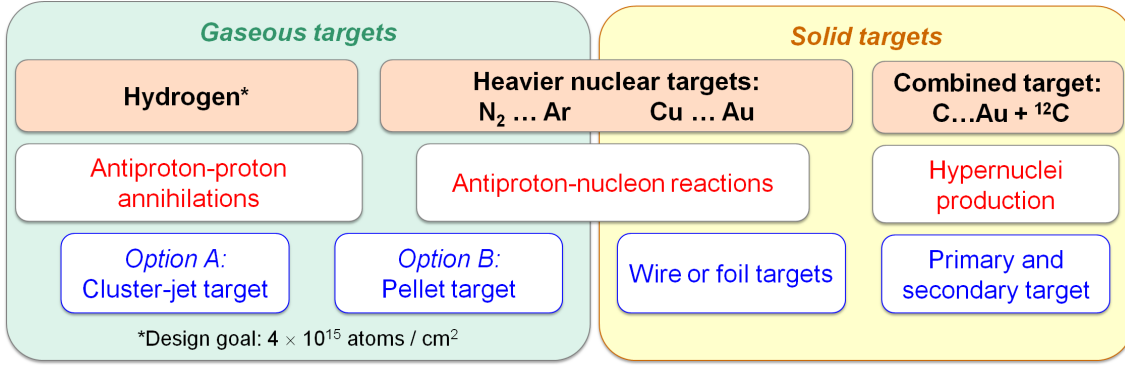


Figure 1.5: Summary of the different target options foreseen at \bar{P} ANDA.

1.1.3 Targets

The design of the solenoid magnet allows for an implementation of different target systems. \bar{P} ANDA will use both gaseous and non-gaseous targets. A very precise positioning of the target is crucial for the exact definition of the primary interaction vertex. In this context, big challenges for either system result from the long distance of roughly 2 m between the target injection point and the dumping system. Hydrogen target systems will be used for the study of antiproton-proton reactions. A high effective target density of about $4 \cdot 10^{15}$ hydrogen atoms per square centimetre must be achieved to fulfill the design goals of the high luminosity mode. Besides the application of hydrogen as target material, an extension to heavier gases such as deuterium, nitrogen or argon is planned for complementary studies with nuclear targets.

At present, two different solutions are under development: a cluster-jet and a pellet target. Both will potentially provide sufficient target thickness but exhibit different properties concerning their effect on the beam quality and the definition of the IP. Solid targets are foreseen for hyper-nuclear studies and the study of antiproton-nucleus interaction using heavier nuclear targets. The different target options are shortly described in the following. Fig. 1.5 gives an overview to all target option foreseen at \bar{P} ANDA.

Cluster Jet Target

Cluster jet targets provide a homogeneous and adjustable target density without any time structure. Optimum beam conditions can be applied in order to achieve highest luminosity. The uncertainty of the IP in a plane perpendicular to the beam axis is defined by the optimised focus of the beam only.

An inherent disadvantage of cluster-jet targets is the lateral spread of the cluster jet leading to an uncertainty in the definition of the IP along the beam axis of several millimetres.

For the target production a pressurised cooled gas is injected into vacuum through a nozzle. The ejected gas immediately condensates and forms a narrow supersonic jet of molecule clusters. The cluster beam typically exposes a broad mass distribution which strongly depends on the gas input pressure and temperature. In case of hydrogen, the average number of molecules per cluster varies from 10^3 to 10^6 . The cluster-jets represent a highly diluted target and offer a very homogenous density profile. Therefore, they may be seen as a localised and homogeneous monolayer of hydrogen atoms being passed by the antiprotons once per revolution, i.e. the antiproton beam can be focused at highest phase space density. The interaction point is thus defined transversely but has to be reconstructed longitudinally in beam direction. At a dedicated prototype cluster target station an effective target density of $1.5 \cdot 10^{15}$ hydrogen atoms per square centimetre has been achieved using the exact \bar{P} ANDA geometry [?]. This value is close to the maximum number required by \bar{P} ANDA. Even higher target densities seem to be feasible and are topic of ongoing R&D work.

Hydrogen Pellet Target

Pellet targets provide a stream of frozen molecule droplets, called pellets, which drip with a fixed frequency off from a fine nozzle into vacuum. The use of pellet targets gives access to high effective target densities. The spatial resolution of the interaction zone can be reduced by skimmers to a few millimetres. A further improvement of this resolution

can be achieved by tracking the individual pellets. However, pellet targets suffer from a non-uniform time distribution, which results in larger variations of the instantaneous luminosity as compared to a cluster-jet target. The maximum achievable average luminosity is very sensitive to deviations of individual pellets from the target axis. The beam must be widened in order to warrant a beam crossing of all pellets. Therefore, an optimisation between the maximum pellet-beam crossing time on the one hand and the beam focusing on the other is necessary.

The design of the planned pellet target is based on the one currently used at the WASA-at-COSY experiment [?]. The specified design goals for the pellet size and the mean lateral spread of the pellet train are given by a radius of $25\ \mu\text{m}$ to $40\ \mu\text{m}$ and a lateral RMS deviation in the pellet train of approximately 1 mm, respectively. At present, typical variations of the interspacing of individual pellets range between 0.5 mm and 5 mm. A new test setup with an improved performance has been constructed [?]. First results have demonstrated the mono-disperse and satellite-free droplet production for cryogenic liquids of H_2 , N_2 and Ar [?]. However, the prototype does not fully include the $\bar{\text{P}}\text{ANDA}$ geometry. The handling of the pellet train over a long distance still has to be investigated in detail. The final resolution on the interaction point is envisaged to be in the order of $50\ \mu\text{m}$. Therefore, an additional pellet tracking system is planned.

Other Target Options

In case of solid target materials the use of wire targets is planned. The hyper-nuclear program requires a separate target station in upstream position. It will comprise a primary and secondary target. The latter must be instrumented with appropriate detectors. Therefore, a re-design of the innermost part of the $\bar{\text{P}}\text{ANDA}$ spectrometer becomes necessary. This also includes the replacement of the MVD.

1.1.4 Luminosity Considerations

The luminosity L describes the flux of beam particles convolved with the target opacity. Hence, an intense beam, a highly effective target thickness and an optimised beam-target overlap are essential to yield a high luminosity in the experiment. The product of L and the total hadronic cross section σ_H delivers the interaction rate R , i.e. the number of antiproton-proton interactions in a specified

time interval, which determines the achievable number of events for all physics channels and allows the extraction of occupancies in different detector regions. These are needed as input for the associated hardware development.

Obviously, the achievable luminosity is directly linked with the number of antiprotons in the HESR. The particles are injected at discrete time intervals. The maximum luminosity thus depends on the antiproton production rate $R_{\bar{p}} = dN_{\bar{p}}/dt$. Moreover, a beam preparation must be performed before the target can be switched on. It includes pre-cooling to equilibrium, the ramping to the desired beam momentum and a fine-tuned focusing in the target region as well as in the section for the electron cooler. Therefore, the operation cycle of the HESR can be separated into two sequences related to the beam preparation time t_{prep} (target off) and the time for data taking t_{exp} (target on), respectively. The beam preparation time t_{prep} also contains the period between the target switch-off and the injection, at which the residual antiprotons are either dumped or transferred back to the injection momentum.

Macroscopic Luminosity Profile

A schematic illustration of the luminosity profile during one operation cycle is given in Fig. 1.6. The maximum luminosity is obtained directly after the target is switched on. During data taking the luminosity decreases due to hadronic interactions, single Coulomb scattering and energy straggling of the circulating beam in the target. Compared to beam-target interaction, minor contributions are related to single intra-beam scattering (Touschek effect). Beam losses caused by residual gas scattering can be neglected, if the vacuum is better than 10^{-9} mbar. A detailed analysis of all beam loss processes can be found in [?, ?]. The relative beam loss rate R_{loss} for the total cross section σ_{tot} is given by the expression

$$R_{\text{loss}} = \tau^{-1} = f_0 \cdot n_t \cdot \sigma_{\text{tot}} \quad (1.1)$$

where τ corresponds to the mean ($1/e$) beam lifetime, f_0 is the revolution frequency of the antiprotons in the ring and n_t is the effective target thickness defined as an area density given in atoms per square centimetre. For beam-target interactions, the beam lifetime is independent of the beam intensity. The Touschek effect depends on the beam equilibria and beam intensity. At low momenta the beam cooling scenario and the ring acceptance have large impact on the achievable beam lifetime.

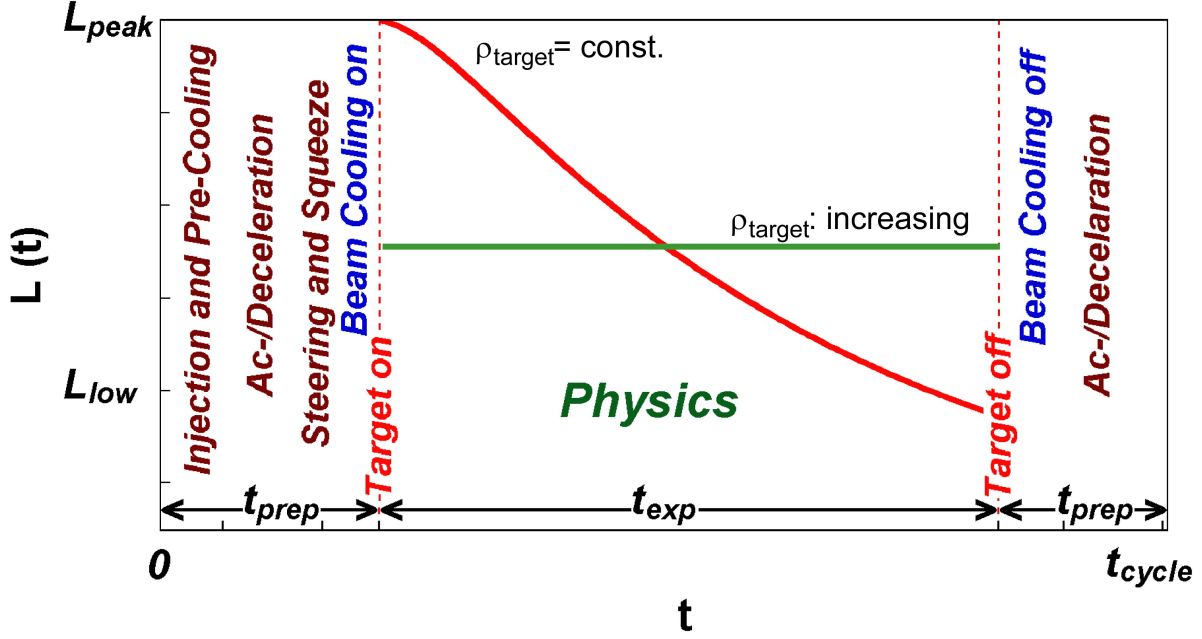


Figure 1.6: Time dependent macroscopic luminosity profile $L(t)$ in one operation cycle for constant (solid red) and increasing (green dotted) target density ρ_{target} . Different measures for beam preparation are indicated. Pre-cooling is performed at 3.8 GeV/c. A maximum ramp of 25 mT/s is specified for beam ac-/deceleration.

	1.5 GeV/c	9 GeV/c	15 GeV/c
Total hadronic cross section/ mbarn	100	57	51
Cluster jet target			
Target density: /cm ⁻²	$8 \cdot 10^{14}$	$8 \cdot 10^{14}$	$8 \cdot 10^{14}$
Antiproton production rate: /s ⁻¹	$2 \cdot 10^7$	$2 \cdot 10^7$	$2 \cdot 10^7$
Beam preparation time: /s	120	140	290
Optimum cycle duration: /s	1280	2980	4750
Mean beam lifetime: /s	~ 5920	~ 29560	~ 35550
Max Cycle Averaged Luminosity: /cm ⁻² s ⁻¹	$0.29 \cdot 10^{32}$	$0.38 \cdot 10^{32}$	$0.37 \cdot 10^{32}$
Pellet target			
Target density: /cm ⁻²	$4 \cdot 10^{15}$	$4 \cdot 10^{15}$	$4 \cdot 10^{15}$
Antiproton production rate: /s ⁻¹	$2 \cdot 10^7$	$2 \cdot 10^7$	$2 \cdot 10^7$
Beam preparation time: /s	120	140	290
Optimum cycle duration: /s	4820	1400	2230
Mean beam lifetime: /s	~ 1540	~ 6000	~ 7100
Max Cycle Averaged Luminosity: /cm ⁻² s ⁻¹	$0.53 \cdot 10^{32}$	$1.69 \cdot 10^{32}$	$1.59 \cdot 10^{32}$

Table 1.2: Calculation of the maximum achievable cycle averaged luminosity for three different beam momenta: Input parameters and final results for different H₂ target setups.

Cycle Average Luminosity

In physics terms, the time-averaged cycle luminosity is most relevant. The maximum average luminosity depends on the ratio of the antiproton production rate to the loss rate and is thus inversely proportional to the total cross section. It can be increased if the residual antiprotons after each cycle are transferred back to the injection momen-

tum and then merged with the newly injected particles. Therefore, a bucket scheme utilising broadband cavities is foreseen for beam injection and the refill procedure. Basically, the cycle average luminosity \bar{L} reads as:

$$\bar{L} = N_{\bar{p},0} \cdot f_0 \cdot n_t \cdot \frac{\tau \left[1 - e^{-\frac{t_{\text{exp}}}{\tau}} \right]}{t_{\text{exp}} + t_{\text{prep}}} \quad (1.2)$$

Target material	\bar{L} ($p_{\text{beam}}=1.5$ GeV/c) [cm ⁻² s ⁻¹]	\bar{L} ($p_{\text{beam}}=15$ GeV/c) [cm ⁻² s ⁻¹]	n_t [atoms/cm ²]
deuterium	$5 \cdot 10^{31}$	$1.9 \cdot 10^{32}$	$3.6 \cdot 10^{15}$
argon	$4 \cdot 10^{29}$	$2.4 \cdot 10^{31}$	$4.6 \cdot 10^{14}$
gold	$4 \cdot 10^{28}$	$2.2 \cdot 10^{30}$	$4.1 \cdot 10^{13}$

Table 1.3: Expected maximum average luminosities, \bar{L} , and required effective target thickness, n_t , for heavier nuclear targets at $\bar{\text{P}}\text{ANDA}$ at minimum and maximum beam momentum p_{beam} . Given numbers refer to an assumed number of 10^{11} antiprotons in the HESR.

where $N_{\bar{p},0}$ corresponds to the number of available particles at the start of the target insertion.

For the calculations, machine cycles and beam preparation times have to be specified. The maximum cycle average luminosity is achieved by an optimisation of the cycle time $t_{\text{cycle}} = t_{\text{exp}} + t_{\text{prep}}$. Constraints are given by the restricted number antiprotons in the HESR, the achievable effective target thickness and the specified antiproton production rate of $R_{\bar{p}} = 2 \cdot 10^7$ s⁻¹ at FAIR.

Main results of calculations performed for different hydrogen targets are summarised in Table 1.2. The total hadronic cross section, $\sigma_H^{\bar{p}p}$, decreases with higher beam momentum from approximately 100 mbarn at 1.5 GeV/c to 50 mbarn at 15 GeV/c. With the limited number of 10^{11} antiprotons, as specified for the high-luminosity mode, cycle averaged luminosities of up to $1.6 \cdot 10^{32}$ cm⁻²s⁻¹ can be achieved at 15 GeV/c for cycle times of less than one beam lifetime. Due to the very short beam lifetimes at lowest beam momenta more than 10^{11} particles can not be provided in average. As a consequence, the average luminosity drops below the envisaged design value at around 2.4 GeV/c to finally roughly $5 \cdot 10^{31}$ s⁻¹cm⁻² at 1.5 GeV/c. Due to the lower assumed target density the achievable luminosity of the cluster-jet target is smaller compared to the pellet operation.

In case of nuclear targets the total hadronic cross section for the interaction of antiprotons with target nucleons can be estimated from geometric considerations taking into account the proton radius of $r_p = 0.9$ fm and the radius of a spherical nucleus R_A , which can be roughly approximated as $R_A = r_0 A^{1/3}$, where $r_0 = 1.2$ fm and A is the mass number. With the assumption that $\sigma_H^{\bar{p}p} = \pi r_p^2$, the required total hadronic cross section, $\sigma_H^{\bar{p}A}$, for a nucleus of mass number A can be extracted from the given values of $\sigma_H^{\bar{p}p}$ for antiproton-proton collisions

as follows:

$$\sigma_H^{\bar{p}A} = \pi(R_A + r_p)^2 = \sigma_H^{\bar{p}p} \cdot \left(\frac{R_A}{r_p} + 1 \right)^2 \quad (1.3)$$

Simulation results on maximum average luminosities based on equation 1.3 are shown in Fig. 1.7. They include adapted beam losses in the target due to single Coulomb scattering and energy straggling. Compared to antiproton-proton experiments, the maximum average luminosity for nuclear targets decreases rapidly with both, higher atomic charge Z and lower beam momenta, by up to three orders of magnitude. Specific values for selected nuclear targets are given in Table 1.3 with the effective target thickness required to reach these numbers.

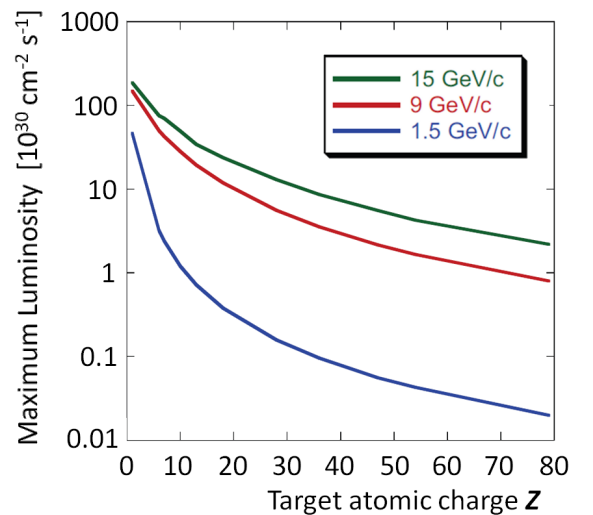


Figure 1.7: Maximum average luminosity vs. atomic charge, Z , of the target for three different beam momenta.

Target material	p_{beam} [GeV/c]	\bar{L}_{exp} [cm ⁻² s ⁻¹]	L_{inst} [cm ⁻² s ⁻¹]	σ_H [mbarn]	\bar{R}_{exp} [s ⁻¹]	$\bar{L}_{\text{peak}}/\bar{L}_{\text{exp}}$ (R_{nom})
hydrogen	1.5	$5.4 \cdot 10^{31}$	$(5.9 \pm 0.6) \cdot 10^{31}$	100	$5.4 \cdot 10^6$	3.7
	15	$1.8 \cdot 10^{32}$	$(2.0 \pm 0.2) \cdot 10^{32}$	51	$9.7 \cdot 10^6$	2.1
argon	1.5	$4.0 \cdot 10^{29}$	$(4.4 \pm 0.4) \cdot 10^{29}$	2020	$8.1 \cdot 10^5$	—
	15	$2.4 \cdot 10^{31}$	$(2.6 \pm 0.3) \cdot 10^{31}$	1030	$2.5 \cdot 10^7$	—
gold	1.5	$4.0 \cdot 10^{28}$	$(4.4 \pm 0.4) \cdot 10^{28}$	7670	$3.1 \cdot 10^6$	—
	15	$2.2 \cdot 10^{30}$	$(2.6 \pm 0.3) \cdot 10^{30}$	3911	$8.6 \cdot 10^6$	—

Table 1.4: Summary of expected event rates at \bar{P} ANDA. Numbers for the hydrogen target correspond to the pellet system (see Table 1.2). The given ratio $\bar{L}_{\text{peak}}/\bar{L}_{\text{exp}}$ corresponds to the maximum value to achieve the nominal interaction rate of $R_{\text{nom}} = 2 \cdot 10^7 \text{ s}^{-1}$. Rough estimates for nuclear targets are based on the numbers given in Table 1.3, with $\bar{L} = \bar{L}_{\text{exp}}$, and σ_H calculated according to equation 1.3.

Event Rates

Besides the cycle-averaged luminosity an evaluation of the instantaneous luminosity during the data taking is indispensable for performance studies of the \bar{P} ANDA detector. Associated event rates define the maximum data load to be handled at different timescales by the individual subsystems. The discussions in this section are based on the following assumptions:

- Nominal antiproton production rate at FAIR:
 $R_{\bar{p}} = 2 \cdot 10^7 \text{ s}^{-1}$
- Effective target density:
 $n_t = 4 \cdot 10^{15} \text{ atoms/cm}^2$
- Maximum number of antiprotons in the HESR:
 $N_{\bar{p},\text{max}} = 10^{11}$
- Recycling of residual antiprotons at the end of each cycle

As indicated in Fig. 1.6 the instantaneous luminosity during the cycle changes on a macroscopic timescale. One elegant way to provide constant event rates in case of a cluster-jet target is given by the possibility to compensate the antiproton consumption during an accelerator cycle by the increase of the effective target density. Alternatively, using a constant target beam density the beam-target overlap might be increased adequately to the beam consumption. With these modifications the instantaneous luminosity during the cycle is expected to be kept constant to a level of 10%.

The values for the luminosity as given in Table 1.2 are averaged over the full cycle time. However, to extract the luminosity during data taking, \bar{L}_{exp} ,

these numbers must be rescaled to consider the time average over the experimental time:

$$\bar{L}_{\text{exp}} = (t_{\text{cycle}}/t_{\text{exp}}) \cdot \bar{L} \quad (1.4)$$

In addition to the fluctuation of the instantaneous luminosity during the operation cycle as discussed above ($\Delta L_{\text{inst}}/L_{\text{inst}} \leq 10\%$), it must be considered that the HESR will be only filled by 90% in case of using a barrier-bucket system. As a consequence, values for L_{inst} during data taking are 10% higher than the ones for \bar{L}_{exp} .

An estimate of peak luminosities, $L_{\text{peak}} > L_{\text{inst}}$, must further include possible effects on a short timescale. Contrary to homogeneous cluster beams, a distinct time structure is expected for the granular volume density distribution of a pellet beam. Such time structure depends on the transverse and longitudinal overlap between single pellets and the circulating antiproton beam in the interaction region. Deviations of the instantaneous luminosity on a microsecond timescale are caused by variations of the pellet size, the pellet trajectory and the interspacing between consecutive pellets. The latter must be well controlled to avoid the possible presence of more than one pellet in the beam at the same instant. The resulting ratio $L_{\text{peak}}/L_{\text{exp}}$ depends on the pellet size. First studies on the expected peak values for the \bar{P} ANDA pellet target have been performed [?]. Results indicate that the peak luminosity stays below $10^{33} \text{ cm}^{-2}\text{s}^{-1}$ if the pellet size is not bigger than $20 \mu\text{m}$.

Finally, for the extraction of event rates the obtained luminosities are multiplied with the hadronic cross section. Table 1.4 summarises the main results for a hydrogen target based on a pellet system, which is expected to deliver upper limits for the occurring event rates. In addition, a rough estimate for nuclear targets based on the input of Table 1.3

and equation 1.3 is given. Even though these values still must be verified by detailed studies, it can be seen that the reduced average luminosity for heavier nuclear targets is counter-balanced by an increased cross-section that results in comparable event rates.

Based on the given assumptions and caveats, as discussed in this section, a nominal interaction rate of $R_{\text{nom}} = 2 \cdot 10^7 \text{ s}^{-1}$ can be defined that all detector systems have to be able to handle. This specification includes the requirement that density fluctuations of the beam-target overlap have to be smaller than a factor of two ($\bar{L}_{\text{peak}}/\bar{L}_{\text{exp}}$). However, in order to avoid data loss it might be important to introduce a generic safety factor that depends on special features of the individual detector subsystems and their position with respect to the interaction region.

1.2 The PANDA Detector

The main objectives of the design of the PANDA experiment are to achieve 4π acceptance, high resolution for tracking, particle identification and calorimetry, high rate capabilities and a versatile readout and event selection. To obtain a good momentum resolution the detector will be composed of two magnetic spectrometers: the *Target Spectrometer (TS)*, based on a superconducting solenoid magnet surrounding the interaction point, which will be used to measure at large polar angles and the *Forward Spectrometer (FS)*, based on a dipole magnet, for small angle tracks. An overview of the detection concept is shown in Fig. 1.8.

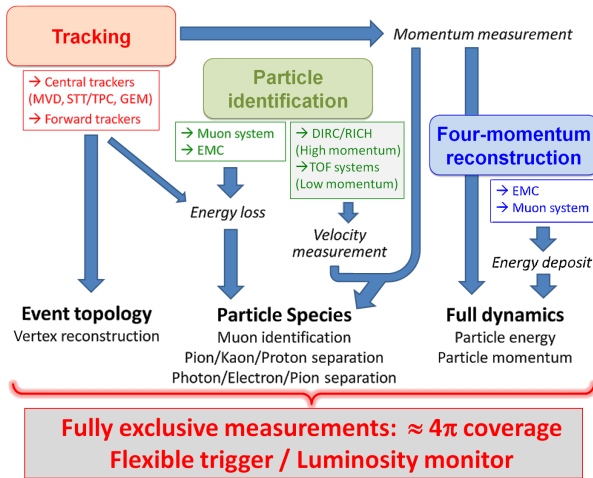


Figure 1.8: Basic detection concept. The main components will be described in chapter 1.2.1 and 1.2.2.

It is based on a complex setup of modular subsystems including tracking detectors (MVD, STT, GEM), electromagnetic calorimeters (EMC), a muon system, Cherenkov detectors (DIRC and RICH) and a time-of-flight (TOF) system. A sophisticated concept for the data acquisition with a flexible trigger is planned in order to exploit at best the set of final states relevant for the PANDA physics objectives.

1.2.1 Target Spectrometer

The Target Spectrometer will surround the interaction point and measure charged tracks in a highly homogeneous solenoidal field. In the manner of a collider detector it will contain detectors in an onion shell like configuration. Pipes for the injection of target material will have to cross the spectrometer perpendicular to the beam pipe.

The Target Spectrometer will be arranged in three parts: the barrel covering angles between 22° and 140° , the forward end cap extending the angles down to 5° and 10° in the vertical and horizontal planes, respectively, and the backward end cap covering the region between about 145° and 170° . Please refer to Fig. 1.9 for an overview.

Beam-Target System

The beam-target system consists of the apparatus for the target production and the corresponding vacuum system for the interaction region. The beam and target pipe cross sections inside the target spectrometer are decreased to an inner diameter of 20 mm close to the interaction region. The innermost parts are planned to be made of beryllium, titanium or a suited alloy which can be thinned to wall thicknesses of $200 \mu\text{m}$. Due to the limited space and the constraints on the material budget close to the IP, vacuum pumps along the beam pipe can only be placed outside the target spectrometer. Insections are foreseen in the iron yoke of the magnet which allow the integration of either a pellet or a cluster-jet target. The target material will be injected from the top. Dumping of the target residuals after beam crossing is mandatory to prevent backscattering into the interaction region. The entire vacuum system is kept variable and allows an operation of both target types. Moreover, an adaptation to non-gaseous nuclear wire targets is possible. For the targets of the planned hypernuclear experiment the whole upstream end cap and parts of the inner detector geometry will be modified. A

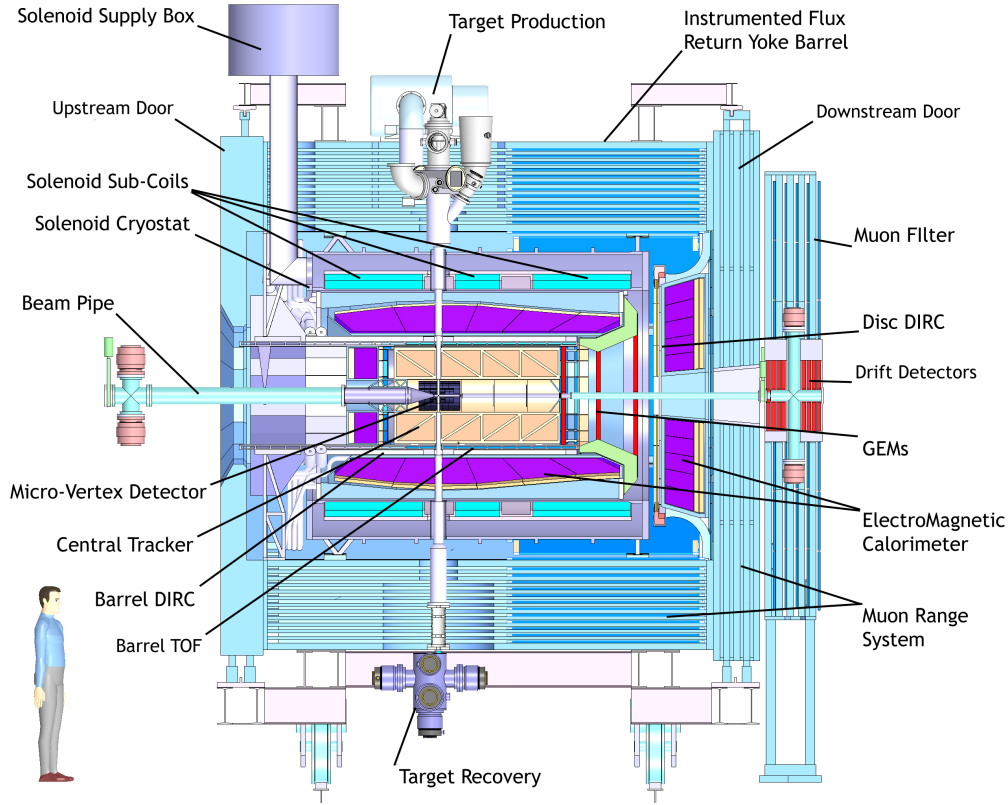


Figure 1.9: Artistic side view of the Target Spectrometer (TS) of \bar{P} ANDA. To the right of this the Forward Spectrometer (FS) follows, which is illustrated in Fig. 1.12.

detailed discussion of the different target options can be found in chapter 1.1.3.

Micro Vertex Detector

The design of the Micro Vertex Detector (MVD) for the Target Spectrometer is optimised for the

Solenoid Magnet

The solenoid magnet of the TS will deliver a very homogeneous solenoid field of 2 T with fluctuations of less than $\pm 2\%$. In addition, a limit of $\int B_r/B_z dz < 2$ mm is specified for the normalised integral of the radial field component. The superconducting coil of the magnet has a length of 2.8 m and an inner diameter of 90 cm, using a laminated iron yoke for the flux return. The cryostat for the solenoid coils is required to have two warm bores of 100 mm diameter, one above and one below the target position, to allow for insertion of internal targets. The load of the integrated inner subsystems can be picked up at defined fixation points. A precise description of the magnet system and detailed field strength calculations can be found in [?].

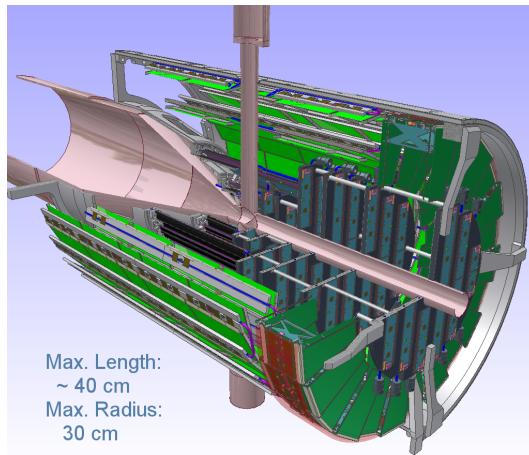


Figure 1.10: The Micro Vertex Detector (MVD) of the Target Spectrometer surrounding the beam and target pipes seen from downstream. To allow a look inside the detector a three-quarters portraits is chosen.

detection of secondary decay vertices from charmed and strange hadrons and for a maximum acceptance close to the interaction point. It will also strongly improve the transverse momentum resolution. The setup is depicted in Fig. 1.10.

The concept of the MVD is based on radiation hard silicon pixel detectors with fast individual pixel readout circuits and silicon strip detectors. The layout foresees a four layer barrel detector with an inner radius of 2.5 cm and an outer radius of 13 cm. The two innermost layers will consist of pixel detectors and the outer two layers will be equipped with double-sided silicon strip detectors.

Six detector wheels arranged perpendicular to the beam will achieve the best acceptance for the forward part of the particle spectrum. While the inner four layers will be made entirely of pixel detectors, the following two will be a combination of strip detectors on the outer radius and pixel detectors closer to the beam pipe.

Additional Forward Disks

Two additional silicon disk layers are considered further downstream at around 40 cm and 60 cm to achieve a better acceptance of hyperon cascades. They are intended to be made entirely of silicon strip detectors. Even though they are not part of the central MVD it is planned, as a first approach, to follow the basic design as defined for the strip disks of the MVD. However, an explicit design optimisation still has to be performed. Two of the critical points to be checked are related to the increased material budget caused by these layers and the needed routing of cables and supplies for these additional disks inside the very restricted space left by the adjacent detector systems.

Straw Tube Tracker (STT)

This detector will consist of aluminised Mylar tubes called *straws*. These will be stiffened by operating them at an overpressure of 1 bar which makes them self-supporting. The straws are to be arranged in planar layers which are mounted in a hexagonal shape around the MVD as shown in Fig. 1.11. In total there are 27 layers of which the 8 central ones are skewed, to achieve an acceptable resolution of 3 mm also in z (parallel to the beam). The gap to the surrounding detectors will be filled with further individual straws. In total there will be 4636 straws around the beam pipe at radial distances between 15 cm and 41.8 cm with an overall length of 150 cm. All straws have a diameter of 10 mm and are made

of a 27 μm thick Mylar foil. Each straw tube is constructed with a single anode wire in the centre that is made of 20 μm thick gold plated tungsten. The gas mixture used will be Argon based with CO_2 as quencher. It is foreseen to have a gas gain not greater than 10^5 in order to warrant long term operation. With these parameters, a resolution in x and y coordinates of less than 150 μm is expected. A thin and light space frame will hold the straws in place, the force of the wire however is kept solely by the straw itself. This overall design results in a material budget of 1.2% of one radiation length.

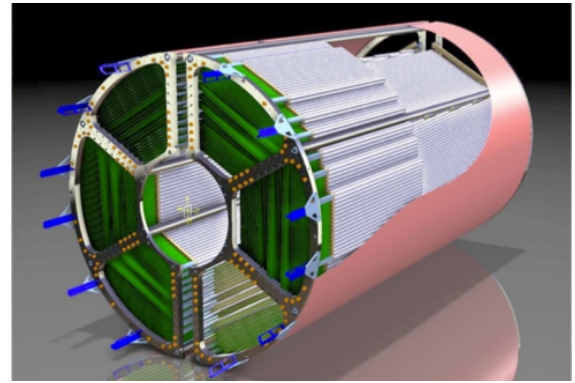


Figure 1.11: Straw Tube Tracker (STT) of the Target Spectrometer with beam and target pipes seen from upstreams.

Forward GEM Detectors

Particles emitted at angles below 22° which are not covered fully by the STT will be tracked by three planar stations placed approximately 1.1 m, 1.4 m and 1.9 m downstream of the target. Each of the station consists of double planes with two projections per plane. The stations will be equipped with Gaseous micro-pattern detectors based on Gas Electron Multiplier (GEM) foils as amplification stages. The chambers have to sustain a high counting rate of particles peaked at the most forward angles due to the relativistic boost of the reaction products as well as due to the small angle $\bar{p}p$ elastic scattering. The maximum expected particle flux in the first chamber in the vicinity of the 5 cm diameter beam pipe will be about $3 \cdot 10^4 \text{ cm}^{-2}\text{s}^{-1}$.

Barrel DIRC

At polar angles between 22° and 140° , particle identification will be performed by the Detection of Internally Reflected Cherenkov (DIRC) light as realised in the BaBar detector [?]. It will consist of

1.7 cm thick fused silica (artificial quartz) slabs surrounding the beam line at a radial distance of 45 cm to 54 cm. At BaBar the light was imaged across a large stand-off volume filled with water onto 11,000 photomultiplier tubes. At \bar{P} ANDA, it is intended to focus the images by lenses onto Micro-Channel Plate PhotoMultiplier Tubes (MCP PMTs) which are insensitive to magnet fields. This fast light detector type allows a more compact design and the readout of two spatial coordinates.

Forward End-Cap DIRC

A similar concept is considered to be employed in the forward direction for particles at polar angles between 5° and 22° . The same radiator, fused silica, is to be employed, however in shape of a disk. The radiator disk will be 2 cm thick and will have a radius of 110 cm. It will be placed directly upstream of the forward end cap calorimeter. At the rim around the disk the Cherenkov light will be measured by focusing elements. In addition measuring the time of propagation the expected light pattern can be distinguished in a 3-dimensional parameter space. Dispersion correction is achieved by the use of alternating dichroic mirrors transmitting and reflecting different parts of the light spectrum. As photon detectors either silicon photomultipliers or microchannel plate PMTs are considered.

Scintillator Tile Barrel (Time-of-Flight)

For slow particles at large polar angles, particle identification will be provided by a time-of-flight (TOF) detector positioned just outside the Barrel DIRC, where it can be also used to detect photon conversions in the DIRC radiator. The detector is based on scintillator tiles of $28.5 \times 28.5 \text{ mm}^2$ size, individually read out by two Silicon PhotoMultipliers per tile. The full system consists of 5,760 tiles in the barrel part and can be augmented also by approximately 1,000 tiles in forward direction just in front of the endcap disc DIRC. Material budget and the dimension of this system are optimised such that a value of less than 2% of one radiation length, including readout and mechanics and less than 2 cm radial thickness will be reached, respectively. The expected time resolution of 100 ps will allow precision timing of tracks for event building and fast software triggers. The detector also provides well timed input with a good spatial resolution for on-line pattern recognition.

Electromagnetic Calorimeters

Expected high count rates and a geometrically compact design of the Target Spectrometer require a fast scintillator material with a short radiation length and Molière radius for the construction of the electromagnetic calorimeter (EMC). Lead tungsten (PbWO_4) is a high density inorganic scintillator with sufficient energy and time resolution for photon, electron, and hadron detection even at intermediate energies [?, ?, ?].

The crystals will be 20 cm long, i.e. approximately $22 X_0$, in order to achieve an energy resolution below 2% at 1 GeV [?, ?, ?] at a tolerable energy loss due to longitudinal leakage of the shower. Tapered crystals with a front size of $2.1 \times 2.1 \text{ cm}^2$ will be mounted in the barrel EMC with an inner radius of 57 cm. This implies 11,360 crystals for the barrel part of the calorimeter. The forward end cap EMC will be a planar arrangement of 3,600 tapered crystals with roughly the same dimensions as in the barrel part, and the backward end cap EMC comprises of 592 crystals. The readout of the crystals will be accomplished by large area avalanche photo diodes in the barrel and in the backward end cap, vacuum photo-triodes will be used in the forward end cap. The light yield can be increased by a factor of about 4 compared to room temperature by cooling the crystals down to -25°C .

The EMC will allow to achieve an e/π ratio of 10^3 for momenta above 0.5 GeV/c. Therefore, e/π -separation will not require an additional gas Cherenkov detector in favour of a very compact geometry of the EMC. A detailed description of the detector system can be found in [?].

Muon Detectors

The laminated yoke of the solenoid magnet acts as a range system for the detection of muons. There are 13 sensitive layers, each 3 cm thick (layer “zero” is a double-layer). They alternate with 3 cm thick iron absorber layers (first and last iron layers are 6 cm thick), introducing enough material for the absorption of pions in the \bar{P} ANDA momentum range and angles. In the forward end cap more material is needed due to the higher momenta of the occurring particles. Therefore, six detection layers will be placed around five iron layers of 6 cm each within the downstream door of the return yoke, and a removable muon filter with additional five layers of 6 cm iron and corresponding detection layers will be moved in the space between the solenoid and the dipole.

As sensors between the absorber layers, rectangular aluminum Mini Drift Tubes (MDT) are foreseen. Basically, these are drift tubes with additional capacitive coupled strips, read out on both ends to obtain the longitudinal coordinate. All together, the laminated yoke of the solenoid magnet and the additional muon filters will be instrumented with 2,600 MDTs and 700 MDTs, respectively.

Hypernuclear Detector

The hypernuclei study will make use of the modular structure of $\bar{\text{PANDA}}$. Removing the backward end cap calorimeter and the MVD will allow to add a dedicated nuclear target station and the required additional detectors for γ spectroscopy close to the entrance of $\bar{\text{PANDA}}$. While the detection of hyperons and low momentum K^\pm can be ensured by the universal detector and its PID system, a specific target system and a γ -detector are additional components required for the hypernuclear studies.

The production of hypernuclei proceeds as a two-stage process. First hyperons, in particular $\Xi\bar{\Xi}$, are produced on a nuclear target. In addition, a secondary target is needed for the formation of a double hypernucleus. The geometry of this secondary target is determined by the short mean life of the Ξ^- of only 0.164 ns. This limits the required thickness of the active secondary target to about 25 mm to 30 mm. It will consist of a compact sandwich structure of silicon micro-strip detectors and absorbing material. In this way the weak decay cascade of the hypernucleus can be detected in the sandwich structure.

An existing germanium-array with refurbished readout will be used for the γ -spectroscopy of the nuclear decay cascades of hypernuclei. The main limitation will be the load due to neutral or charged particles traversing the germanium detectors. Therefore, readout schemes and tracking algorithms are presently being developed which will enable high resolution γ -spectroscopy in an environment of high particle flux.

1.2.2 Forward Spectrometer

The Forward Spectrometer (FS) will cover all particles emitted in vertical and horizontal angles below $\pm 5^\circ$ and $\pm 10^\circ$, respectively. Charged particles will be deflected by an integral dipole field. Cherenkov detectors, calorimeters and muon counters ensure the detection of all particle types. Fig. 1.12 gives an overview to the instrumentation of the FS.

Dipole Magnet

A 2 Tm dipole magnet with a window frame, a 1 m gap, and more than 2 m aperture will be used for the momentum analysis of charged particles in the FS. In the current planning, the magnet yoke will occupy about 1.6 m in beam direction starting from 3.9 m downstream of the target. Thus, it covers the entire angular acceptance of the TS of $\pm 10^\circ$ and $\pm 5^\circ$ in the horizontal and in the vertical direction, respectively. The bending power of the dipole on the beam line causes a deflection of the antiproton beam at the maximum momentum of 15 GeV/c of 2.2° . For particles with lower momenta, detectors will be placed inside the yoke opening. The beam deflection will be compensated by two correcting dipole magnets, placed around the $\bar{\text{PANDA}}$ detection system. The dipole field will be ramped during acceleration in the HESR and the final ramp maximum scales with the selected beam momentum.

Forward Trackers

The deflection of particle trajectories in the field of the dipole magnet will be measured with three pairs of tracking drift detectors. The first pair will be placed in front, the second within and the third behind the dipole magnet. Each pair will contain two autonomous detectors, thus, in total, 6 independent detectors will be mounted. Each tracking detector will consist of four double-layers of straw tubes (see Fig. 1.13), two with vertical wires and two with wires inclined by a few degrees. The optimal angle of inclination with respect to vertical direction will be chosen on the basis of ongoing simulations. The planned configuration of double-layers of straws will allow to reconstruct tracks in each pair of tracking detectors separately, also in case of multi-track events.

Forward Particle Identification

To enable the π/K and K/p separation also at the highest momenta a RICH detector is proposed. The favoured design is a dual radiator RICH detector similar to the one used at HERMES [?]. Using two radiators, silica aerogel and C_4F_{10} gas, provides $\pi/K/p$ separation in a broad momentum range from 2 to 15 GeV/c. The two different indices of refraction are 1.0304 and 1.00137, respectively. The total thickness of the detector is reduced to the freon gas radiator ($5\%X_0$), the aerogel radiator ($2.8\%X_0$), and the aluminum window ($3\%X_0$) by using a lightweight mirror focusing the Cherenkov

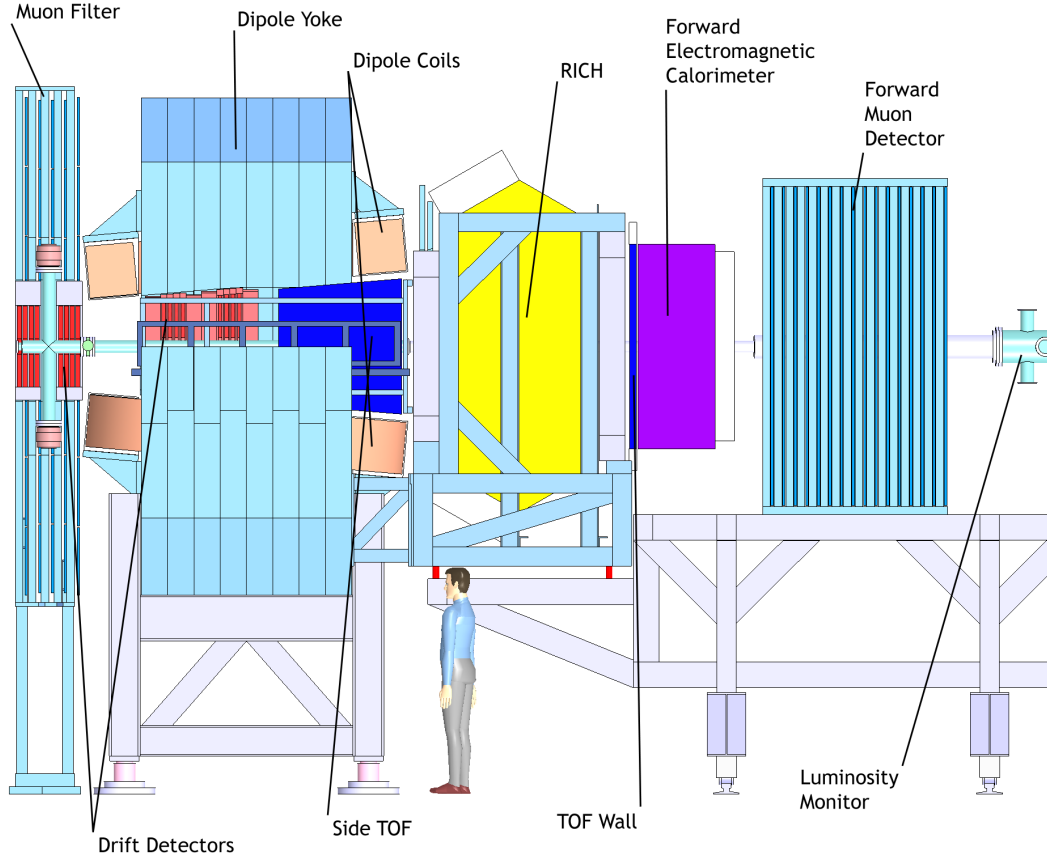


Figure 1.12: Artistic side view of the Forward Spectrometer (FS) of \bar{P} ANDA. It is preceded on the left by the Target Spectrometer (TS), which is illustrated in Fig. 1.9.

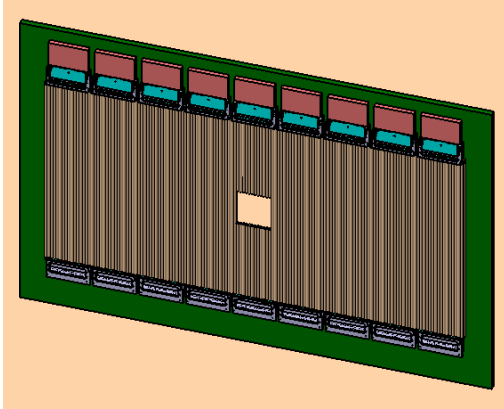


Figure 1.13: Double layer of straw tubes with preamplifier cards and gas manifolds mounted on rectangular support frame. The opening in the middle of the detector is foreseen for the beam pipe.

active volume.

A wall of slabs made of plastic scintillator and read out on both ends by fast photo-tubes will serve as time-of-flight stop counter placed at about 7 m from the target. Similar detectors will be placed inside the dipole magnet opening to detect low momentum particles which do not exit the dipole magnet. The time resolution is expected to be in the order of 50 ps thus allowing a good π/K and K/p separation up to momenta of 2.8 GeV/c and 4.7 GeV/c, respectively.

Forward Electromagnetic Calorimeter

For the detection of photons and electrons a Shashlyk-type calorimeter with high resolution and efficiency will be employed. The detection is based on lead-scintillator sandwiches read out with wavelength shifting fibres passing through the block and coupled to photo-multipliers. The lateral size of one module is 110 mm \times 110 mm and a length of

light on an array of photo-tubes placed outside the

680 mm ($= 20X_0$). A higher spatial resolution will be achieved by sub-dividing each module into 4 channels of $55\text{ mm} \times 55\text{ mm}$ size coupled to 4 PMTs. To cover the forward acceptance, 351 such modules, arranged in 13 rows and 27 columns at a distance of 7.5 m from the target, are required. With similar modules, based on the same technique as proposed for PANDA, an energy resolution of $4\%/\sqrt{E}$ [?] has been achieved.

Forward Muon Detectors

For the very forward part of the muon spectrum, a further range tracking system consisting of interleaved absorber layers and rectangular aluminium drift-tubes is being designed, similar to the muon system of the TS, but laid out for higher momenta. The system allows discrimination of pions from muons, detection of pion decays and, with moderate resolution, also the energy determination of neutrons and anti-neutrons. The forward muon system will be placed at about 9 m from the target.

Luminosity Monitor

The basic concept of the luminosity monitor is to reconstruct the angle of elastically scattered antiprotons in the polar angle range from 3 mrad to 8 mrad with respect to the beam axis corresponding to the Coulomb-nuclear interference region. The luminosity monitor will consist of a sequence of four planes of double-sided silicon strip detectors located in the space between the downstream side of the forward muon system and the HESR dipole needed to redirect the antiproton beam out of the PANDA chicane back into the direction of the HESR straight stretch (i.e. between $z = +11\text{ m}$ and $z = +13\text{ m}$ downstream of the target). The planes are positioned as close to the beam axis as possible and are separated by 20 cm along the beam direction. Each plane consists of four wafers arranged perpendicular surrounding to the beam axis placed at top, down, right and left. In this way, systematic errors can be strongly suppressed. The silicon wafers will be located inside a vacuum chamber to minimise scattering of the antiprotons before traversing the tracking planes. With the proposed detector setup an absolute precision of about 3% on the time integrated luminosity is considered feasible for this detector concept at PANDA.

1.2.3 Data Acquisition

In PANDA, a data acquisition concept is being developed to be as much as possible matched to the complexity of the experiment and the diversity of physics objectives and the rate capability of at least $2 \cdot 10^7$ events/s. Therefore, every sub-detector system is a self-triggering entity. Signals are detected autonomously by the sub-systems and are preprocessed. Only the physically relevant information is extracted and transmitted. This requires hit-detection, noise-suppression and clusterisation at the readout level. The data related to a particle hit, with a substantially reduced rate in the preprocessing step, is marked by a precise time stamp and buffered for further processing. The trigger selection finally occurs in computing nodes which access the buffers via a high-bandwidth network fabric. The new concept provides a high degree of flexibility in the choice of trigger algorithms. It makes trigger conditions available which are outside the capabilities of the standard approach.

1.2.4 Infrastructure

The PANDA experimental hall will be located in the east straight section of HESR. The planned floor space in the hall will be of $43\text{ m} \times 29\text{ m}$. Within the cave, the PANDA detector, the auxiliary equipment, the beam steering magnets and the focusing elements will be housed. To allow for access during HESR operation, the area of the beam line and the detector will be shielded with movable concrete blocks. Controlled access will be provided via a properly designed chicane in the concrete wall. In addition, the experimental hall will provide additional space for components storage and detector parts assembly. The PANDA hall will feature an overhead crane, spanning the whole area and with a maximum load capacity of 25 t. The shielded space for the PANDA detector and the beam line will have an area of $37\text{ m} \times 9.4\text{ m}$ and a height of 8.5 m. The beam line at a height of 3.5 m. The floor level in the HESR tunnel will be 2 m higher. The TS with its front-end electronics will be mounted on rails and movable from the on-beam position to outside the shielded area, to allow simultaneous detector and accelerator maintenance.

In the south-west corner of the PANDA hall, the experiment counting house complex is foreseen. It will be a complex made of five floors. At the first floor, the supplies for power, high voltage, cooling water, gases and other services will be housed. The second floor will provide space for the readout electronics

and data processing and the online processing farm will be housed at the third floor. The hall electricity supply and ventilation will be hosted at the fifth floor, whereas at the fourth floor there will be the space for the shift crew: the control room and a meeting room, with some service rooms, will be at the same level of the surrounding ground. The PANDA experiment will need liquid helium for the TS solenoid and for the compensation solenoid. The refrigeration scheme will be similar to the one used for the BaBar magnet [?]. The cryogenic plant will be built and characterised at FZ Jülich and moved to FAIR with the magnet. In the natural convection refrigeration scheme that has been proposed, the storage-liquefaction Dewar close to the liquefier acts as buffer for the system. With the projected LHe consumption (safety factor on cryogenic losses included), a 2000 *l* storage will allow ~ 10 *h* of operation in case of liquefier failure, giving ample time margin for the magnet discharge. The supply point will be at the north-east area of the building. From that point, the LHe will be delivered to the control Dewar, which can be chosen sufficiently small (~ 30 *l*) to minimise the LHe inventory in the \bar{P} ANDA hall. The helium gas coming out from the thermal shields would be recovered at room temperature and pressure in the low pressure recovery system.

All other cabling, which will be routed starting at the counting house, will join the LHe supply lines at the end of the rails system of the TS at the eastern wall. The temperature of the building will be moderately controlled. More stringent requirements with respect to temperature and humidity for the detectors have to be maintained locally. To facilitate cooling and avoid condensation, the Target Spectrometer will be kept in a tent with dry air at a controlled temperature.

1.3 The Charged Particle Tracking System

There are different tracking systems for charged particles at \bar{P} ANDA, positioned inside the target spectrometer and in the forward region around the dipole magnet. Main tasks of the global tracking system are the accurate determination of the particle momenta, a high spatial resolution of the primary interaction vertex and the detection of displaced secondary vertices. Therefore, measurements of different subdetectors have to be merged in order to access the full tracking information.

1.3.1 Basic Approach

The magnetic solenoid field in the target spectrometer results in a circular transverse motion of charged particles with non-zero transverse momentum. The particle momentum then can be extracted via the determination of the bending radius. However, tracks with a small polar angle will exit the solenoid field too soon to be measured properly. For this case, the particle deflection induced by the subsequent dipole magnet is used to measure the particle momentum. Basically it can be deduced from a combined straight line fit before and after the dipole.

Due to the different analysing magnets, different track fitting algorithms have to be applied for central and forward tracks. Central tracks are reconstructed by combining hit points in the MVD layers with the hit information of the STT or the GEM stations. For the reconstruction of small angle tracks the straw tube layers in the forward spectrometer have to be used. In overlap regions the MVD, the additional forward disks or the GEM stations can contribute to the forward tracking because the delivery of an additional track point closer to the IP significantly improves the precision of the fitting results. After the global identification of individual tracks an event mapping have to be performed to match different tracks of the same event to a common vertex which either corresponds to the primary interaction vertex or a delayed decay of short-lived particles.

The luminosity monitor at the downstream end of the experiment is a tracking device of its own right. It was introduced to measure the time integrated luminosity, which is essential for the determination of cross sections for different physics processes. Therefore, elastically scattered antiprotons are measured under small angles corresponding to small momentum transfers. The associated differential cross sections are well known and thus provide an ideal reference channel. Additional information from the MVD will eventually improve the measurement by taking advantage of the reconstructed slow recoil proton at polar angles of around 90° , which is correlated with the highly energetic antiproton detected in the luminosity monitor.

1.3.2 Optimisation Criteria

The different topics of the \bar{P} ANDA physics program will impose specific optimisation criteria and requirements to design and performance of the tracking system. The optimum design thus depends on

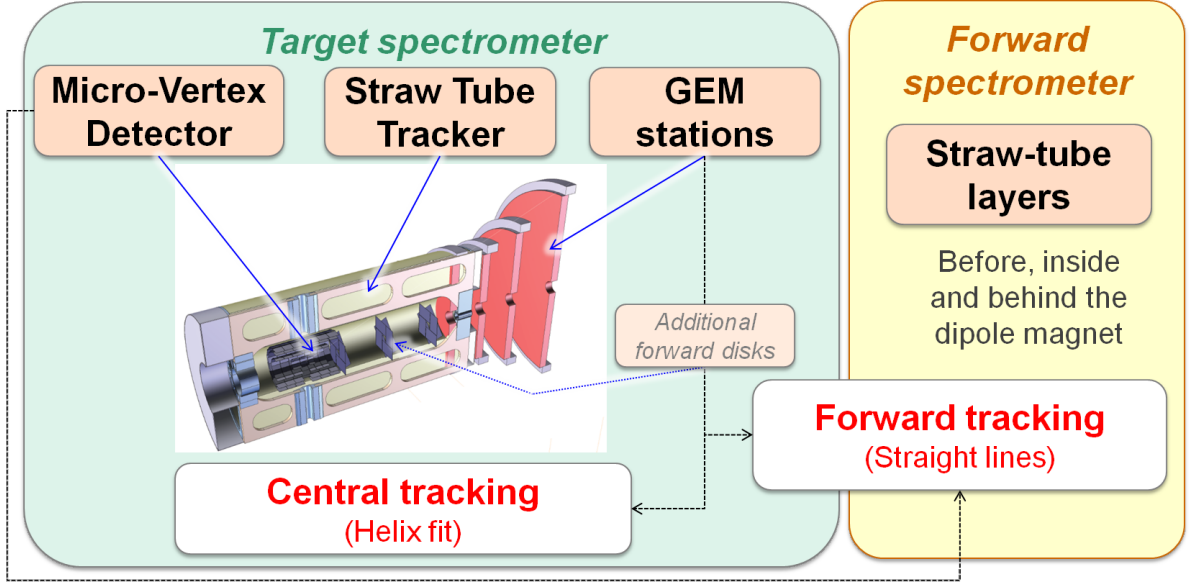


Figure 1.14: Overview of the $\bar{\text{PANDA}}$ tracking system, including the option of the additional forward disks.

the relative weight which is given to the different physics aspects. Main criteria for the optimisation will be discussed in the following.

Acceptance

Full 2π azimuthal coverage is mandatory in order to allow identification of multi-particle final states and studies of correlations within the produced particles. In particular, the spectroscopy program of charmed and strange hadrons relies on the measurement of Dalitz plot distributions of three-body final states, which requires a smooth acceptance function across the full phase space. Particular care has to be taken to avoid gaps in the acceptance function and to minimise the effect of discontinuities induced by the transition between adjacent sub-detector components, by detector frames or by mechanical support structures.

The fixed-target setup at $\bar{\text{PANDA}}$ implies a Lorentz boost γ_{CM} of the centre of mass ranging from 1.20 to 2.92. This large dynamic range in the Lorentz boost corresponds to a large difference in the typical event topologies at low and at high antiproton momenta. At higher antiproton beam momenta the vast majority of the produced particles in the final state will be emitted into the forward hemisphere. However, light particles like e^\pm , μ^\pm or π^\pm may well be emitted into the backward hemisphere even at highest beam momentum. As an example, pion backward emission is possible for a centre of mass momentum $p_{cm} > 93 \text{ MeV}/c$ at $p_{\bar{p}} = 1.5 \text{ GeV}/c$, and

for $p_{cm} > 380 \text{ MeV}/c$ at $p_{\bar{p}} = 15 \text{ GeV}/c$.

Backward charged particle tracking is needed for various measurements foreseen at $\bar{\text{PANDA}}$. For instance, for the independent determination of the electric and magnetic parts of the time-like proton form factor in the reaction $\bar{p}p \rightarrow e^+e^-$ the full angular distribution has to be measured. At $q^2 = 14 \text{ GeV}^2/c^2$, that is at $p_{\bar{p}} = 6.45 \text{ GeV}/c$, a polar angle of 160° in the centre of mass frame corresponds to electrons with a momentum of $0.70 \text{ GeV}/c$ at $\theta_{lab} = 113^\circ$. Detection of pions in the backward hemisphere is important in studies of strange, multi-strange and charmed baryon resonances in $\bar{p}p \rightarrow Y^* \bar{Y}' (+c.c.)$ reactions where the excited hyperon Y^* decays by single or double pion emission. Also higher charmonium states may emit pions with decay energies above the critical value for backward emission in the laboratory. The $\bar{\text{PANDA}}$ tracking detectors therefore have to cover the full range of polar angles between 0° and about 150° .

Besides the solid angle of the detector also the acceptance in momentum space has to be considered. Often the final state contains charged particles with very large and with very small transverse momentum components which need to be reconstructed at the same time. Given the strength of the solenoid field of 2 T required to determine the momentum vector of the high transverse momentum particle, the radius of the transverse motion of the low transverse momentum particle may be small. Sufficient tracking capability already at small distance from the beam axis is therefore mandatory. As an exam-

ple one may consider the reaction $\bar{p}p \rightarrow D^{*+}D^{*-}$ close to threshold with $D^{*+} \rightarrow D^0\pi^+$ (& c.c.). Assuming 39 MeV/c momentum of the decay particles in the $D^{*\pm}$ rest frame, particles of the subsequent decay $D^0 \rightarrow K^-\pi^+$ (& c.c.) have 61 MeV/c momentum in the D^0/\bar{D}^0 rest frame. In the solenoid field of the TS, the charged pions and kaons from the D^0/\bar{D}^0 decay may have helix diameters up to almost 1.5 m. The transverse motion of the charged pion from the $D^{*\pm}$ decay stays within a distance of almost 7 cm from the beam axis and therefore need to be reconstructed based on the track information from the MVD only.

Delayed Decay Vertex Detection

An important part of the \bar{P} ANDA physics program involves final states consisting of hadrons with open charm or strangeness which decay by weak interaction and thus have macroscopic decay lengths. The decay length of charmed hadrons is of the order of 100 μm ($\approx 310 \mu\text{m}$ for D^\pm , $\approx 150 \mu\text{m}$ for D_s^\pm , $\approx 120 \mu\text{m}$ for D^0 , $\approx 130 \mu\text{m}$ for Ξ_c^\pm , $\approx 60 \mu\text{m}$ for Λ_c^+ , and $\approx 30 \mu\text{m}$ for Ξ_c^0). Therefore, the design of the tracking system aims on a detection of decay vertices of particles with decay lengths above 100 μm . In order to achieve sufficient separation of the reconstructed decay vertex, the inner part of the tracking system has to be located very close to the interaction point, both in longitudinal and in radial direction. This requirement is fulfilled in the design of the MVD.

The identification of hyperons and K_S mesons requires the reconstruction of delayed decay vertices at much larger distances. Λ and Ξ hyperons have comparatively large decay lengths of about 8 cm and 5 cm, respectively. Due to the Lorentz boost this may result in vertices which are displaced by tens of centimetres from the interaction point mostly in the downstream direction. The considerations in the previous section concerning the required acceptance thus apply with respect to the shifted emission points of charged particles. The inner part of the \bar{P} ANDA tracking system, therefore needs sufficient extension to the downstream direction in order to deliver sufficient track information for charged particle tracks originating from these displaced vertices.

Momentum and Spatial Resolution

The spatial resolution of the tracking detectors is important in two aspects. In the vicinity of the interaction point it directly determines the preci-

sion to which primary and displaced decay vertices can be reconstructed. Further on, based on the deflection of charged particles in both solenoid and dipole magnetic fields, it is an essential contribution to the momentum resolution of charged particles in all three coordinates.

The detection of displaced vertices of charmed hadrons imposes particular requirements to the spatial resolution close the interaction point. With a typical Lorentz boost $\beta\gamma \simeq 2$, D meson decay vertices have a displacement of the order of a few hundreds micrometres from the primary production point. Hence, to distinguish charged daughter particles of D mesons from prompt particles a vertex resolution of 100 μm is required. The position resolution is less demanding for the reconstruction of strange hadrons having decay lengths on the scale of centimeters. In this case a vertex resolution of a few millimetres is sufficient. Due to the significant Lorentz boost and the small opening angle between the decay particles of hyperons the resolution in transverse direction is required to be much better than the one for the longitudinal component.

The achievable momentum resolution is a complex function of the spatial resolution of the tracking sub-detectors, the number of track-points, the material budget of active and passive components resulting in multiple scattering, the strength and homogeneity of the magnetic field, and of the particle species, its momentum and its emission angle. Due to the respective momentum dependence, it is generally expected that multiple scattering limits the momentum resolution of low energy particles, whereas for high energy particles the smaller curvature of the tracks is the dominant contribution to the resolution.

The resolution in the determination of the momentum vectors of the final state particles directly determines the invariant or missing mass resolution of the particles that are to be reconstructed. Typically, the width of hadrons unstable with respect to strong interaction (except for certain narrow states like e.g. charmonium below the $D\bar{D}$ threshold) is of the order of 10 MeV/ c^2 to 100 MeV/ c^2 . As an instrumental mass resolution much below the natural width is without effect, a value of a few 10 MeV/ c^2 seems to be acceptable for the identification of known states or for the mass measurement of new states. With a typical scale of GeV/ c^2 for the kinematic particle energy this translates to a relative momentum resolution σ_p/p of the order of 1% as design parameter for the \bar{P} ANDA tracking detectors.

Count Rate Capability

The expected count rates depend on the event rate as discussed in chapter 1.1.4 and the multiplicity of charged particles produced in the events. While the total rate is of importance for DAQ design and on-line event filtering, the relevant quantity for detector design and performance is the rate per channel, which is a function of the granularity per detector layer and of the angular distribution of the emitted particles. The latter depends on the beam momentum and the target material.

The nominal event rate at $\overline{\text{PANDA}}$ is given by $2 \cdot 10^7$ interactions per second. In case of $\bar{p}p$ annihilations typically only a few charged particles are produced. Even if secondary particles are taken into account, the number of charged particles per event will not be much larger than 10 in most cases. Thus the detector must be able to cope with a rate of $2 \cdot 10^8$ particles per second within the full solid angle. Particular attention has to be paid to elastic $\bar{p}p$ scattering since this process contributes significantly to the particle load in two regions of the detector: scattering of antiprotons at small forward angles and the corresponding emission of recoil protons at large angles close to 90° . This affects primarily the inner region of the MVD disc layers and the forward tracking detector as well as the MVD barrel part and the central tracker.

The use of nuclear targets will not create significantly higher count rates than obtained with a hydrogen or deuterium target. This is due to single Coulomb scattering which dramatically increases with the nuclear charge ($\propto Z^4$) and results in \bar{p} losses with no related signals in the detector. In contrast to $\bar{p}p$ collisions in $\bar{p}A$ collisions no high rate of recoil particles close to 90° is expected. The emission angles of recoil protons from quasi-free $\bar{p}p$ scattering are smeared by Fermi momentum and rescattering, while recoil nuclei, if they at all survive the momentum transfer, are too low energetic to pass through the beam pipe.

Particle Identification

Charged particle identification over a wide range of momentum and emission angle is an essential prerequisite for the capability of $\overline{\text{PANDA}}$ to accomplish the envisaged physics program. Charged particles with higher momenta will be identified via Cherenkov radiation by the DIRC detector in the Target Spectrometer and by the forward RICH detector in the Forward Spectrometer. For positive charged kaon-pion separation in the DIRC about

800 MeV/ c momentum is required. While almost all particles emitted within the acceptance of the Forward Spectrometer are above the Cherenkov threshold due to the forward Lorentz boost, a number of interesting reaction channels have final states with heavier charged particles (K^\pm, p, \bar{p}) at larger angles with momenta below the DIRC threshold. In order to separate these low energy kaons from the much more abundant pions, particle identification capability based on energy loss information has to be supplied by the central tracking detector.

Material Budget

Any active or passive material inside the detector volume contributes to multiple scattering of charged particles, electron bremsstrahlung and photon conversion, and thus reduces the momentum resolution for charged particles in the tracking detectors, and detection efficiency and energy resolution for photons in the EMC. Therefore the material budget has to be kept as low as possible. Following the more demanding requirements to meet the performance criteria of the EMC, a total material budget of MVD and Central Tracker below 10% is still considered to be acceptable [?].

References

- [1] \bar{P} ANDA collaboration, Letter of intent for: \bar{P} ANDA - Strong Interaction Studies with Antiprotons, Technical report FAIR-ESAC, 2004.
- [2] GSI Helmholtzzentrum für Schwerionenforschung, FAIR - An International Accelerator Facility for Beams of Ions and Antiprotons, Baseline technical report, 2006, <http://www.gsi.de/fair/reports/btr.html>.
- [3] Technical report, http://www.fair-center.de/fileadmin/fair/publications_FAIR/FAIR_GreenPaper_2009.pdf.
- [4] P. Spiller and G. Franchetti, Nucl. Instrum. Methods **A561**, 305 (2006).
- [5] W. F. Henning, Nucl. Instrum. Methods **A805**, 502c (2008).
- [6] \bar{P} ANDA Collaboration, Physics Performance Report, 2009, [arXiv:0903.3905v1](https://arxiv.org/abs/0903.3905v1).
- [7] FAIR Technical Design Report, HESR, Technical report, Gesellschaft für Schwerionenforschung (GSI), Darmstadt, 2008, http://www-win.gsi.de/FAIR-EOI/PDF/TDR_PDF/TDR_HESR-TRV3.1.2.pdf.
- [8] A. Lehrach et al., Int. J. Mod. Phys. E **18**, 420 (2009).
- [9] B. Gålnander et al., Proc. of the European Accelerator Conference EPAC2008, GenoaProc. of the European Accelerator Conference EPAC2008, Genoa **THPP**, 3473 (2008).
- [10] H. Stockhorst, D. Prasuhn, R. Maier and B. Lorentz, AIP Conf. Proc. **821**, 190 (2006).
- [11] B. Lorentz et al., Proceedings of European Accelerator Conference EPAC, Genova **MOPPC**, 325 (2008).
- [12] D. Welsch et al., Closed Orbit Correction and Sextupole Compensation Schemes for Normal-Conducting HESR, in *the European Accelerator Conference EPAC2008, Genoa, THPC076*, p. 3161, 2008.
- [13] A. Lehrach, O. Boine-Frankenheim, F. Hinterberger, R. Maier, and D. Prasuhn, Nucl. Instrum. Meth. **A561**, 289 (2006).
- [14] F. Hinterberger, in *Beam-Target Interaction and Intra-beam Scattering in the HESR Ring*, Report of the Forschungszentrum Jülich, 2006, Jül-4206, ISSN 0944-2952.
- [15] O. Boine-Frankenheim, R. Hasse, F. Hinterberger, A. Lehrach, and P. Zenkevich, Nucl. Instrum. Meth. **A560**, 245 (2006).
- [16] D. Reistad et al., Calculations on High-Energy Electron Cooling in the HESR, in *Proceedings of the Workshop on Beam Cooling and Related Topics COOL2007, Bad Kreuznach, MOA2C05*, p. 44, 2007.
- [17] H. Stockhorst et al., Stochastic Cooling Developments for the HESR at FAIR, in *Proceedings of EPAC08, Genoa, Italy THPP055*, p. 3491, 2008.
- [18] A. Täschner et al., Nucl. Instrum. Meth. **A660**, 22 (2011).
- [19] C. Bargholtz et al., Nucl. Instrum. Methods **A587**, 178 (2008).
- [20] M. Büscher et al., AIP Conf. Proc. **814**, 614 (2006).
- [21] M. Büscher et al., Int. J. Mod. Phys. E **18**, 505 (2009).
- [22] A. Smirnov et al., Effective luminosity simulation for \bar{P} ANDA experiment at FAIR, in *Proceedings of COOL2009, Lanzhou, China, THPMCP002*, 2009.
- [23] \bar{P} ANDA collaboration, Technical Design Report for the Solenoid and Dipole Spectrometer Magnets, [arxiv:0907.0169v1](https://arxiv.org/abs/0907.0169v1), 2009.
- [24] H. Staengle et al., Nucl. Instrum. Meth. **A397**, 261 (1997).
- [25] K. Mengel et al., IEEE Trans. Nucl. Sci. **45**, 681 (1998).
- [26] R. Novotny et al., IEEE Trans. Nucl. Sci. **47**, 1499 (2000).
- [27] M. Hoek et al., Nucl. Instrum. Meth. **A486**, 136 (2002).
- [28] \bar{P} ANDA collaboration, EMC Technical Design Report, Technical report, Darmstadt, 2008, [arXiv:0810.1216v1](https://arxiv.org/abs/0810.1216v1).
- [29] N. Akopov et al., Nucl. Instrum. Meth. **A479**, 511 (2002).

- [30] I.-H. Chiang et al., (1999), KOPIO Proposal.
- [31] F. P. et al., IEEE Trans. Appl. Supercond. **9**,
N. 2, 847 (1999).

2 Overview of the Forward Tracker

2.1 Basic requirements and performance goals

2.2 General layout

2.2.1 Straw tube description

Straws are gas-filled cylindrical tubes with a conductive inner layer as cathode and an anode wire stretched along the cylinder axis. A high electric field between the wire and the outer conductor separates electrons and positive ions produced by a charged particle along its trajectory through the gas volume. Usually, the wire is on positive voltage of a few kV and collects the electrons while the ions drift to the cathode. By choosing thin wires, with a diameter of few tens of μm , the electric field strength near the wire is high enough to start further gas ionizations by electron collisions with gas molecules. Depending on the high voltage set and the gas characteristics an amplification of about $10^4 - 10^5$ of the primary charge signal is possible, which is then high enough to read out the signal.

By measuring the drift time of the earliest arriving electrons one gets the information about the minimum particle track distance from the wire. The isochrone contains all space points belonging to the same electron drift time and describes a cylinder around the wire axis. The characteristic relation between drift time and isochrone is given by the electron drift velocity, depending on specific gas parameters, electric and magnetic field. Therefore, this fundamental relation has to be calibrated using reference tracks with known space and drift time information. The particle track is reconstructed by a best fit to the isochrones measured in a series of several straw tubes with the same orientation. Additional skewed straw layers provide a full stereo view of the particle trajectory.

The specific energy loss of a charged particle in the straw gas volume can be used to identify the particle species and can be derived from the number of ionization electrons which generated the straw signal. Since the specific ionization in gas with about 100 ion-electron pairs per cm for minimum ionizing particles is quite low and shows in addition a strong fluctuation described by an asymmetric Landau distribution, a higher number of measurements is needed to get a sufficient precision for the particles energy loss. The truncated mean method, which reject from many samples those with the largest energy losses due to the fluctuations, can help to improve the resolution.

Straw detectors exhibit the most simple geometry of highly symmetric, cylindrical tubes and have several advantages which are summarized in the following:

- robust electrostatic configuration. The shielding tube around each high voltage wire suppresses signal cross-talk and protects neighbor straws in case of a broken wire;
- robust mechanical stability if the straws are arranged in close-packed multilayers;
- high tracking efficiency due to minimal dead zones ($\sim 1\%$) at tube ends and between neighbor straws if close-packed;
- high spatial resolution, $\sigma_{r\phi} < 150\mu\text{m}$ depending on tube diameter and gas characteristics. Simple calibration of space-drift time relation due to the cylindrical isochrone shape;
- small radiation length, $X/X_0 \sim 0.05\%$ per tube, if straws with thinnest ($\sim 30\mu\text{m}$) film tubes are used;
- high rate capability can be improved by reducing the occupancy using smaller tube diameter and/or choosing a fast drift gas.

2.2.1.1 Straw materials

The straw tubes foreseen for the Forward Tracker have a length of up to 1500 mm, 10 mm inner diameter, and a total wall thickness of $27\mu\text{m}$. They are made of two layers of $12\mu\text{m}$ thin aluminized mylar [?] films by wrapping two long film strips around a rotating mandrel and gluing the two half-overlapping strips together. Then the cylindrical film tube is stripped off. The aluminization at the inner tube wall is used as the cathode whereas the aluminization of the second, outer strip layer is used to prevent light incidence.

A gold-plated tungsten-rhenium wire with $20\mu\text{m}$ diameter is used as anode. Cylindrical precision end plugs made from ABS [?] with a wall thickness of 0.5 mm close the tube at both ends (Fig. 2.1). They are glued to the mylar film leaving a small 1.5 mm film overlap on both ends. There, a gold-plated copper-beryllium spring wire is inserted to provide the electric cathode contacting. The springs allow 2 mm tube elongation with a typical spring force equivalent to 10 g. The end plugs have a central hole with a 3 mm thick cylindrical nose to insert and glue a crimp pin for the wire. A micro PVC (medical quality grade) tube is fed through another hole and glued in the end plugs to provide a gas flow through the tube. The total weight of a fully assembled straw is 2.5 g. The anode wire is stretched by a weight of 50 g and crimped in the copper pins at a gas overpressure in the straw tube of 1 bar.

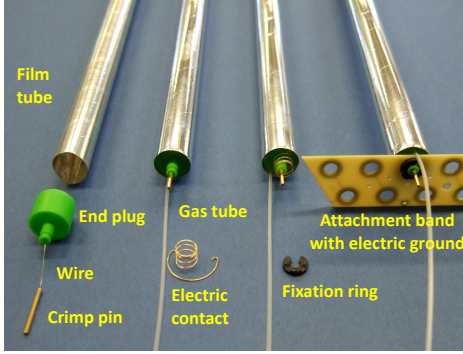


Figure 2.1: A straw consists of a mylar film tube which is closed by two end plugs, each containing a crimp pin to fix the anode wire in the center and a gas tube to provide a gas flow through the tube. The contact springs inserted in the small film overlap at both tube ends provide the electric cathode contact. The straw ends are fixed by a plastic ring to an attachment band which contains on the inner side the electric ground.

Table 2.1 lists the different straw components and their thickness in radiation lengths. The chosen film tubes are the thinnest used for straw detectors, but still show sufficient mechanical stability for the assembly to self-supporting double-layers. For the proposed \bar{P} ANDA straw tracker the total radiation length of the straw volume is 1.2 % with a maximum number of 27 hit straw layers for a traversing particle track in radial direction.

2.2.1.2 Pressurized straws

Both, efficiency and resolution of a straw are best for a perfect cylindrical shape of the film tube and the wire being highly concentrically in the cylinder axis. With a wire tension¹ of about 50 G inside a 1.5 m long straw tube inclined at 5° with respect to the vertical direction, as planned in the tracking station FT6 - the largest one in the FS, the maximum sag due to gravitation in the tube center is less than 3 μ m. For the 4736 straws of the FT6 this adds up to a wire tension equivalent to about 237 kG which must be maintained. Usually, this is done by fixing the straw tubes inside a strong and massive, surrounding frame or by adding reinforcement structures like CF-strips along the tubes to keep them straight. All methods inevitably increase the detector thickness given in radiation length by this additional materials.

Therefore a new technique based on self-supporting

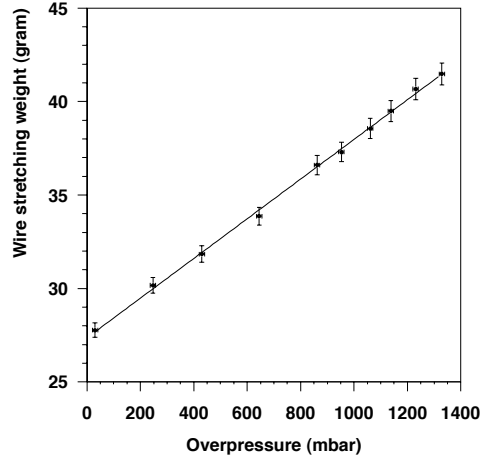


Figure 2.2: Measured wire tension (weight equivalent) at different gas overpressure inside a straw. The nominal tension is 40 G at 1.2 bar overpressure for the COSY-STT straws.

straw layers with intrinsic wire tension developed for the COSY-TOF straw tracker [?] has been adopted for the \bar{P} ANDA Central Tracker and is also used for the Forward Tracker. The straw tubes are assembled and the wire is stretched by 50 G at an overpressure of about 1 bar. Then the tubes are close-packed and glued together to planar double-layers on a reference table which defines a precise tube to tube distance of 10.1 mm. At the gas overpressure of 1 bar the double-layer maintains the nominal wire tension of 50 G for each tube, i.e. becomes self-supporting.

The precision of the tube and wire stretching method by the gas overpressure for the used thin film tubes was studied in great detail for the COSY-TOF straw tubes. Fig. 2.2 shows the measured tension with decreasing gas overpressure. A well-defined tension is seen, even down to vanishing overpressure where only the stiffness of the mylar film tube maintains a wire tension of 28 G. The nominal tension for the COSY-TOF 1 m long straws was 40 G at 1.2 bar overpressure. For the \bar{P} ANDA 1.5 m long straws the nominal tension is 50 G at 1.0 bar overpressure.

1. Usually given as the mass weight used to stretch the wire.

Table 2.1: Mean thickness in radiation lengths of the different straw tube components. The number for the gas mixture is evaluated at 20° and 2 atm.

Element	Material	X[mm]	X ₀ [cm]	X/X ₀
Film Tube	Mylar, 27 μm	0.085	28.7	3.0×10^{-4}
Coating	Al, 2×0.03 μm	2×10^{-4}	8.9	2.2×10^{-6}
Gas	Ar/CO ₂ (10 %)	7.85	6131	1.3×10^{-4}
Wire	W/Re, 20 μm	3×10^{-5}	0.35	8.6×10^{-6}
\sum_{straw}				4.4×10^{-4}

2.2.1.3 Gas mixture

The need of high spatial resolution in the FT requires high amplitude anode signals even for the single electron clusters, thus requiring high gas gain. On the other side, a high gas gain significantly reduces the chamber lifetime. For the optimum gas amplification choice both these factors should be taken into account properly. Table 2.2 shows the main parameters of some of the most used gases and gas mixtures. In order to select the most suited gas mixture for the FT detector, it is useful to consider two essentially different situations. Some gas mixtures, if a low electric field is set up, can effectively quench the electron kinetic energy, preventing them to gain enough energy between collisions. In this case, electrons are in thermal equilibrium with the surrounding medium and the drift velocity is proportional to the electric field tension. Such gases are usually called “cold” for that given electric field strength.

On the contrary, if the electron average kinetic energy differs from the thermal energy, the drift velocity behavior becomes more complicated. In many gas mixtures the drift velocity becomes saturated and does not depend on the electric field strength. That makes the reconstruction of the track coordinates easier. However, to get high spatial resolution in this “hot” gas mixtures become difficult, in principle, due to the large diffusion. The standard choice of many experiments is to have a “hot” or “warm” gas mixture, that has a weak dependence of the drift velocity on the applied electric field. In this case, the electric field inhomogeneities do not play a significant role, which makes the calibration simpler. An overpressure can be used in these cases to reduce the diffusion.

The main requirements, that should be taken into account for the choice of the most suited gas mixture, are:

- good spatial resolution;
- rate capability;
- radiation hardness;
- radiation length;
- chemical inactivity;
- working voltage;
- working pressure;
- accessibility on the market and price.

For the \bar{P} ANDA FT the spatial resolution, the rate capability and the radiation hardness are the points of highest importance. Initially a “cold” gas mixture of He + 10% i C₄H₁₀ was proposed for the Conceptual Design Report [?]. Although this gas mixture has one undoubted advantage, the long radiation length X₀, it provides a relatively low drift velocity, which is a disadvantage more or less peculiar for all “cold” gases. As a result, a gas mixture based on Ar + 10%CO₂ has been suggested.

In Fig. 2.3 and Fig. 2.4 are shown the results of the simulation for the spatial resolutions achievable for the Ar + 10%CO₂ and He + 10%iC₄H₁₀ for 1 and 2 atm gas pressure. The simulations have been performed using the GARFIELD program and the build-in MAGBOLTZ package [?]. The good agreement of these simulation data with the experimental results obtained by the KLOE drift chamber prototype [?], as shown in Fig. 2.4, can be interpreted as a proof of the validity of the simulations of the straw tube parameters.

The spatial resolution of the Ar + 10%CO₂ mixture is satisfactory even at 1 atm pressure, while the spatial resolution in the He + 10%iC₄H₁₀ is worse than the required 150 μm, and only an increase of the pressure could improve this situation. The total drift time is also an important parameter. The

Table 2.2: Properties of different gases and gas mixtures. Z and A are charge and atomic weight, for molecules the total number have to be taken, N_p and N_t are the number of primary and total electrons per cm, respectively, E_x and E_i are the excitation and ionization energy, respectively, W_i is the average energy required to produce one electron-ion pair in the gas, $(dE/dx)_{mip}$ is the most probable energy loss by a minimum ionizing particle and X_0 is an radiation length. For gas mixtures, weighted average value have to be taken.

Gas or gas mixture	Z	A	E_x [eV]	E_i [eV]	W_i [eV]	dE/dx [keV/cm]	N_p [cm ⁻¹]	N_t [cm ⁻¹]	X_0 [m]
He	2	4	19.8	24.5	41	0.32	4.2	8	5299
Ar	18	40	11.6	15.7	26	2.44	23	94	110
CO ₂	22	44	5.2	13.7	33	3.01	35.5	91	183
iC ₄ H ₁₀	34	58	6.5	10.6	23	5.93	84	195	169
Ar+10%CO ₂	-	-	-	-	26.7	2.5	24.6	93	117
He+10%iC ₄ H ₁₀	-	-	-	-	39.2	0.88	12.7	26.7	1313
He+20%iC ₄ H ₁₀	-	-	-	-	37.4	1.44	20.6	45.4	749

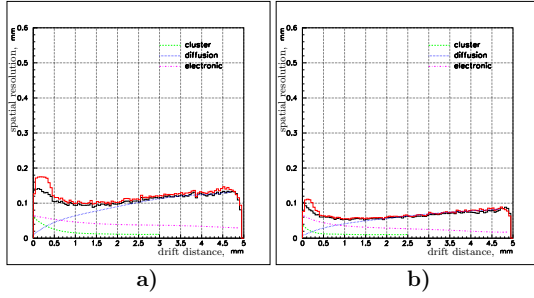


Figure 2.3: The spatial resolution for the Ar+10%CO₂ gas mixture for 1 a) and 2 atm b) pressures. The red line corresponds to an ideal $r(t)$ relation, the black one to the measured. The main contributions to the resolution are also shown in different colors

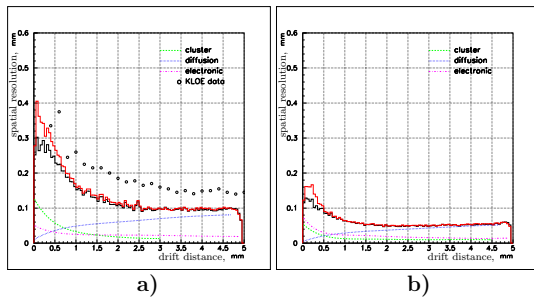


Figure 2.4: Spatial resolution in He+10% i-C₄H₁₀ with 1 a) and 2 atm b). The red line corresponds to an ideal $r(t)$ relation, the black one to the measured. The main contributions to the resolution are also shown in different colors. The experimental spatial resolution of the KLOE drift chamber, denoted by the open circles, is given for comparison [?]

Ar+10%CO₂ mixture has a drift time of 80 ns for a 4 mm drift path. The He+10%iC₄H₁₀ has double

the drift time. Since the average time between two events in PANDA will be ~ 100 ns, when using the He+10%iC₄H₁₀ gas mixture, the information from two consecutive events could be contained in the STT at any time. This event mixing in the tracker will result in a significant complication of the trigger logic and of the pattern recognition algorithm. By increasing the pressure two times, the drift time for the He+10%iC₄H₁₀ grows by 50 ns, while for the Ar + 10%CO₂ only by 10 ns. That makes the situation with the event mixing even more difficult.

The effect of the electronics threshold on the spatial resolution has also been studied. The average gas gain has been reduced by a factor two using the same electronic threshold. Fig. 2.5 shows only a small deterioration of the Ar+10%CO₂ resolution and a strong worsening in the case of the He+10%iC₄H₁₀ gas mixture. This is one more argument in favor of the Ar + 10%CO₂ usage.

All these considerations shows strong advantages for the Ar + 10%CO₂ gas mixture for the \bar{P} ANDA STT compared with He + 10%iC₄H₁₀ gas composition.

The possibility to use higher percentages of CO₂ has been investigated. Fig. 2.6 shows the space-time relation with two different CO₂ percentages: 10% and 30%, respectively. A greater percentage of CO₂ produces an increase of the electron diffusion which worsen the achievable space resolution. For completeness, we must notice that a greater percentage of quencher will reduce the effect of the magnetic field on the mixture (Lorentz angle). Therefore the final concentration of CO₂ component could be defined only after test with magnetic field.

The variations of the gas mixture performance due to changes of the absolute temperature have

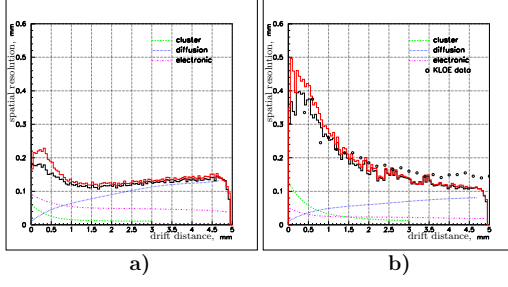


Figure 2.5: The spatial resolution for the Ar+10%CO₂ a) and the He+10%CO₂ b) gas mixtures at 1 atm pressures. The gas gain has been reduced by a factor two compared with Fig. 2.3 and Fig. 2.4. The red lines correspond to an “ideal” $r(t)$ relation, while the black one corresponds to the measured one. Contributions from the main limiting process are shown by dashed lines. The spatial resolution of the KLOE drift chamber, denoted by the open circles, is given for comparison [?].

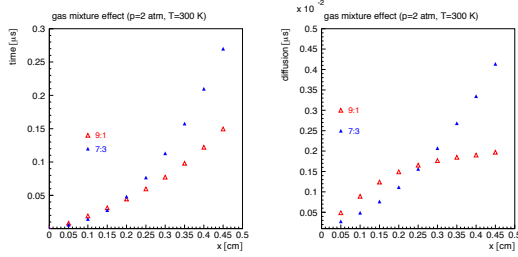


Figure 2.6: Space time relation (left) and diffusion (right) of two gas mixtures with different CO₂ percentage, red points correspond to a percentage of 10%, blue to 30% one.

been studied. The space time relation for the Ar+10%CO₂ mixture at 1 atm for two different temperatures, 250 and 300 K, is shown in Fig. 2.7. No significant differences are present between the two curves. Therefore, it will not be necessary to keep under control the temperature variation.

2.2.2 Straw tube module

The detection planes are built of separate modules, each containing 32 straws arranged in two layers. A schematic drawing of a single straw module is shown in Fig. 2.8. Each module is equipped with its own preamplifier-discriminator card. It has also its own high voltage supply and gas supply lines. In this way a straw module constitutes an autonomous mechanical and electrical unit.

Straw modules arranged side by side as schematically shown in Fig. 2.9 form a detection plane. Further on we refer to it as a “double layer”.

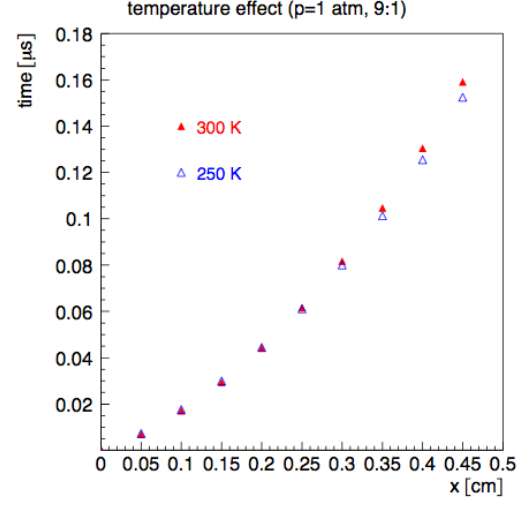


Figure 2.7: Space time relation for the Ar+10%CO₂ mixture at 1 atm for two different temperatures.

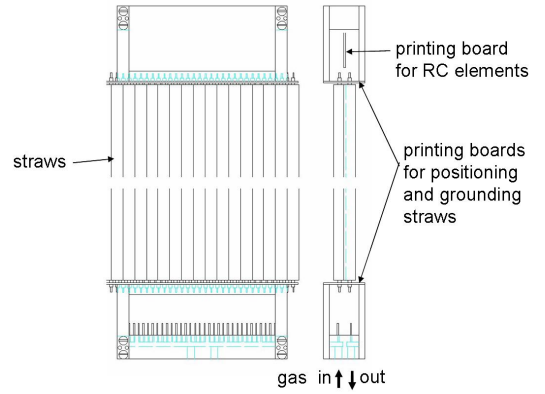


Figure 2.8: Schematic drawing of straw module.

During assembly of straw layers and also for repairs, the straw modules can be mounted or dismantled from the support frame without the need to remove the neighbouring modules as it is explained in Fig. 2.10.a.

2.2.3 Layer arrangement

Each of the six tracking stations of the Forward Spectrometer contain four double layers: the first and fourth layer contain vertical straws (0°) and the two intermediate layers - the second and the third one - contain straws inclined respectively at +5° and -5°. This arrangement of straws allows for a three dimensional reconstruction of multiple track events. It contains also some redundancy allowing to compensate the lower detection efficiency at track distances from the sense wire close to the

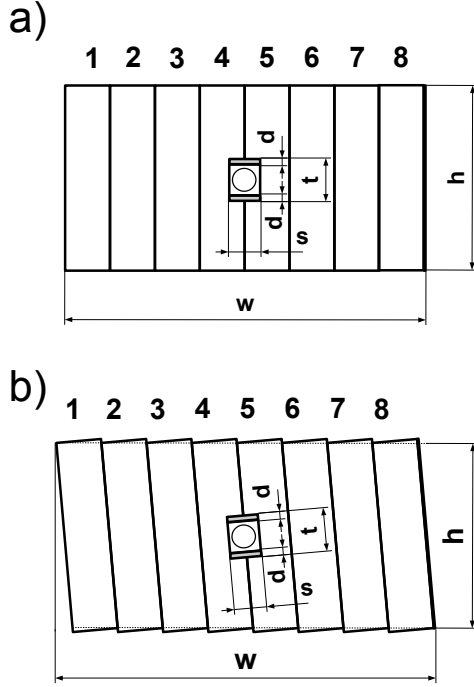


Figure 2.9: Arrangement of straw modules in double layer with vertical modules (a) and with modules inclined at 5° (b). The central rectangular opening is foreseen for the beam pipe.

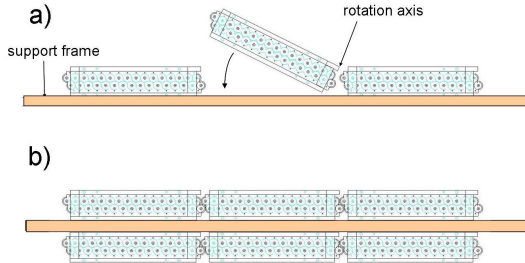


Figure 2.10: (a) Method of bringing in position on support frame a single straw module. In order to avoid clashes with neighbouring modules, the module is rotated around axis defined by one of the edges of its housing. (b) Two double layers mounted on common support frame.

straw radius. In the tracking stations DC1, DC2, DC5, DC6 one support frame is used for a pair of double layers. In the tracking stations DC3 and DC4 each double layer is mounted on separate support frame. Each module can be mounted and dismounted from the support frame without the need to remove the neighboring modules which simplifies the assembly and the repairs of the tracking

stations.

The double layers in the tracking stations DC1, DC2 consist of 8 modules, in DC3, DC4 - of 12 modules, in DC5 of 25 modules and in DC6 of 37 modules.

3 Construction of tracking stations

3.1 Tracking stations before the dipole magnet

text

3.2 Tracking stations inside the dipole magnet gap

text

3.3 Tracking stations after the dipole magnet

Deformation of the FT6 support frame under its own weight is shown in Fig. 3.1.

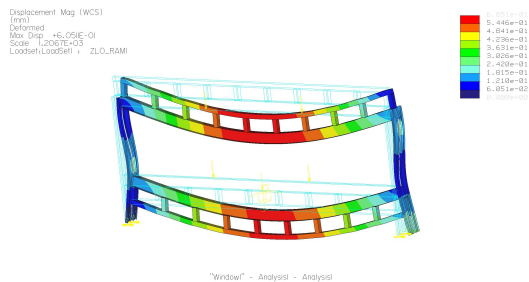


Figure 3.1: Deformation of the FT6 support frame under its own weight.

4 Infrastructure

4.1 The gas system

The preferred gas mixture for the $\bar{\text{PANDA}}$ -FT is argon with an admixture of about 10–20 % CO_2 as the quenching component. The details that brought to this choice are illustrated in Sec. 2.2.1.3. This gas mixture has also good capability to tolerate high irradiation levels (see Sec. ??) since no deposits on the straw tube electrodes from polymerisation reactions occur, provided that there is a clean gas environment including all materials and parts of the detector and gas supply system in contact with the gas. For both gas components a high purity grade is required (argon with grade 5.0, CO_2 with 4.8). The supply lines consist of polished stainless steel pipes and thermoplast (PA) tubings where a higher flexibility is needed. Since argon and CO_2 are non-flammable, not expensive, and components of the atmosphere, no recirculation and containment of the gas mixture is needed, and the gas supply of the detector is done in flushing mode. The FT will be operated at a gas pressure of about 2 bar (absolute) and preferably at room temperature. The total FT gas volume of about 1 m³ is exchanged typically every six hours with a flow rate of about 100 l per minute to refresh the gas mixture and to prevent an accumulation of contaminants in the detector and gas system.

The gas system of the FT consists of high pressure, supply gas bottles for each mixture component, cleaning filters in the gas lines, a mixing section with ratio-based mass flow controllers, regulated by a pressure transducer inserted in the FT volume to set a constant absolute pressure of about 2 bar in the detector, the supply lines in and out of the detector and outlet valves to a dedicated exhaust line at the $\bar{\text{PANDA}}$ experimental area. The scheme of the gas distribution system is shown in Fig. 4.1. The mass flow controller and meter devices [?] are based on digital electronics. In these devices the analog sensor signal is sent directly to a micro processor. By doing so, optimum signal stability and accuracy is achieved. An integral alarm function continuously checks the difference between the set point and the measured value. If the supply pressure drops the instrument gives a warning. In addition the instrument runs a self diagnostics routine, and controller settings can be remotely adjusted with a hand terminal or a computer using an RS-485 busline. For the Ar/ CO_2 gas mixture

the required accuracies of the settings and control have to be better than 0.3 % (absolute) for the mixture ratio, about 1-2 mbar for the pressure, and 1 K for the temperature.

The $\bar{\text{PANDA}}$ FT straw tubes are arranged in six tracking stations. Each station is sub-divided in four double-layers. Each double-layer is connected to individual supply line. In this way 24 supply lines are needed. To flux the straws with the required, pressurized, two components gas mixture, the following guidelines have been followed:

- reducing the redundancy of the system to lower the costs and the complexity of the system;
- keeping the space needed for the system within reasonable boundaries (\sim few cm);
- assure a minimal redundancy to guaranty, in case of failure, the operation of at least parts of any sector;
- automatization and remote control of the flux parameters, with the possibility to switch to manual/local operation for:
 - proportion the two-components of the gas mixture;
 - quantify the fluxed mixture;
 - setting mixture overpressure;
 - controlling the temperature.

With this selection of multiplicity and topology, in case of failure of one line, it is assured that at least one half of any sector remains operative. This is particularly important for the stereo tubes that allow to determine the z-coordinate of particle trajectories. These gas lines are then connected to gas distributors that finally bring the gas to each straw. Fig. 4.1 shows a first prototype of these distributors. It consist of a stainless steel pipe having a wall thickness of 0.1 mm and a diameter of 3 or 4 mm. On it, small capillaries (diam. 0.55 mm) are welded and will be connected to the individual straws. By connecting 2 straws in series it is possible to arrange the in- and outlet gas manifolds at the same end of the detector, preferable at the backward end.

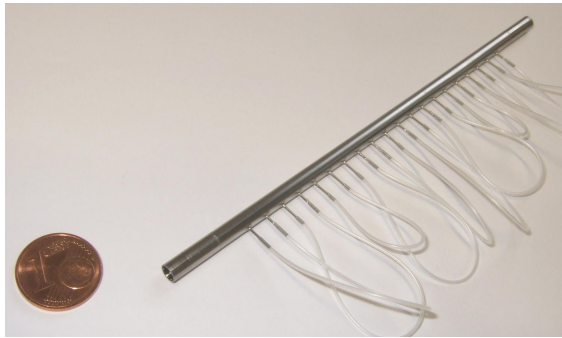


Figure 4.1: Prototype of a gas distributor consisting of a stainless steel pipe (4 mm diameter, 0.1 mm wall thickness) with small capillaries (0.55 mm diameter) for connecting the individual straws.

4.2 The readout electronics

4.2.1 Requirements

The input characteristics of the front end electronics should match the electrical properties of the straw tubes. The basic properties of the straws are listed in Table 4.1.

Capacitance	8.9 pF/m
Sense wire resistance	258 Ω /m
Inductance	1.24 μ H/m
Impedance	373 Ω
Analog cross talk	$\leq 1\%$

Table 4.1: Straw electrical properties.

From the point of view of the pulse propagation the straw tube acts as a coaxial lossy transmission line with an impedance given by the formula:

$$Z = \sqrt{\frac{R + i\omega L}{i\omega C}}, \quad (4.1)$$

where R is the electrical resistance, L is the inductance, C is the capacitance and ω is the angular frequency. For high frequencies (> 100 MHz), the impedance of the straw tubes tends to the limit $Z \rightarrow \sqrt{\frac{L}{C}} = 373 \Omega$ (see Fig. 4.2).

The Forward Tracker consists of ≈ 13500 straw tubes grouped in 6 tracking stations (see Sect. 2.2.3). The maximum counting rate is expected in the vicinity of the beam pipe in the first tracking station (FT1) and it reaches 400 kHz at the highest energy and 2×10^7 interactions/s. It rapidly decreases with increasing distance from the beam axis (see *figure has to be added*). The maximum

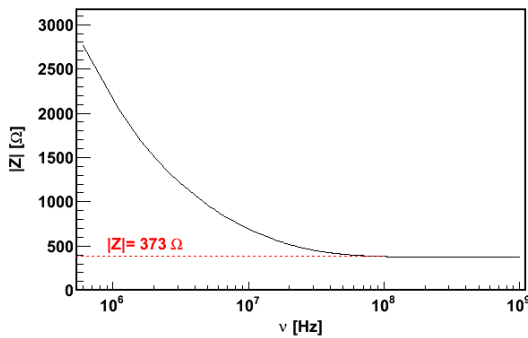


Figure 4.2: Straw tube impedance as a function of frequency $\nu = \omega/2\pi$ (solid black line). The high frequency limit is indicated with the red dashed line.

drift time of electrons in the straw tubes placed outside a strong magnetic field (tracking stations FT1, FT2, FT5 and FT6) is about 140 ns. In turns, in the straws tubes working in the magnetic field of the dipole magnet reaching up to 0.9 T (tracking stations FT3 and FT4) it extends to 180 ns (???). An average double-hit probability is smaller than 10 % for the straw tubes in the vicinity of the beam pipe. The requested electronic time resolution should be around 1 ns and the intrinsic noise level below 1 fC. The maximum analog pulse duration should be comparable to the maximum drift time of 180 ns. Basic requirements of the front end electronics are listed in Table 4.2.

Peaking time	≤ 20 ns
Double pulse resolution	~ 100 ns
Intrinsic electronic noise	< 1 fC
Discrimination threshold	≈ 5 fC
Max. drift time	200 ns
Max. occupancy	$< 10\%$
TDC resolution	~ 1 ns
Neutron exposure (10 years)	??? 1/cm ²
Radiation dose (10 years)	??? krad

Table 4.2: Front end electronics requirements.

4.2.2 General concept

To fulfill all these requirements, the proposed straw tube read-out organization comprises 3 stages:

1. Analog Front End Electronics (FEE) cards hosting, depending on radial distance from the beam, 36-80 channels. FEE is composed of preamplifier, amplifier with analog signal shaping and discriminator unit with differential output.
2. Digital Board (DB) for time and amplitude (or charge) measurements, local logic resources for noise suppression, fast hit detection, memory buffer for hit storage, serial Gbit optical links for the data transmission and slow control;
3. Detector Concentrator Board (DCB) (optional) receiving and merging inputs from several DB in local memory buffer and sending it to the \bar{P} ANDA DAQ system.

The data from the DCBs will be transferred via fast optical links to Compute Nodes for the on-line

track reconstruction and subsequently, after merging with the information from other PANDA detector systems, for the event selection. It will be possible to perform some local correlations on the data inside the single DB to suppress noise and reduce the amount of data sent from the board.

The PANDA data acquisition and filtering systems will implement a trigger-less architecture. Instead of having a hardware trigger signal, which indicates the occurrence of a valid event, each DB will receive a precise clock signal distributed centrally from a single source: the Clock and Timing Distribution System (CTDS). The DB boards will continuously monitor the detector channels and will generate data packets whenever the number of the input signals exceeds programmed thresholds. These data will be tagged with time-stamps obtained from the CTDS.

The data acquisition system will profit from the structured running mode of the HESR operation. Periods of $2\mu\text{s}$ with antiproton interactions will be interleaved with periods of 400 ns of idle time. The information on the accelerator activity will be distributed to DCBs via the Clock and Timing Distribution System. The data recorded during the interaction intervals will be grouped together in DCB to form a burst which will be then uniquely tagged. Grouping of data from many bursts into predefined epoques (e.g. $500\mu\text{s}$) inside DB is also considered in order to reduce network traffic. Data from all PANDA detectors tagged with the same burst identification number will be grouped together and will be made accessible to filtering algorithms implemented in the Compute Nodes (CN). Decisions produced by these algorithms will thus be based on the complete detector data with full granularity.

4.2.3 Analog front-end electronics

An Application Specific Integrated Circuit (ASIC) is being developed in order to read out the straw tube pulses. The main specifications of this chip are summarized in Table 4.3.

The ASIC's channel comprises a charge preamplifier stage, a pole-zero cancelation network (PZC), a shaper stage, a tail cancelation network, a discriminator circuit, a baseline holder (BLH), a fast differential LVDS output and an analog output. The block diagram of the designed readout channel is shown in Fig. 4.3.

The solution for the FEE should provide both, the timing and the amplitude information. Since it is still under study whether the Time Over Threshold

Table 4.3: Main parameters of the new straw tube front-end readout chip (see text for more details).

Technology	0.35 μm CMOS
Number of channels	16
Input Resistance	$\sim 120\ \Omega$
Default gain	$\sim 10\ \text{mV/fC}$
Peaking time (for delta)	20 ns
Timing resolution	1-2 ns
Equivalent (delta) input range	0-200 fC
Noise ENC	$\leq 0.4\ \text{fC}$
Output standard	LVDS and analog
Power consumption	$\sim 30\ \text{mW}$

(TOT) technique or the analog amplitude information will be used for the energy-loss measurement, the first ASIC prototype provides both the amplitude and TOT information.

A typical simulated analog response of the amplifier for straw tube pulses (generated with GARFIELD) for different charge depositions is shown in Fig. 4.4. The charge depositions are expressed both as equivalent charges of "delta-like" pulses and as integrated charge carried by the pulses. The tail cancelation network assures that the pulse length is shorter than about 150 ns.

The design of the first version of the ASIC channel was completed and a first prototype containing 4 readout channels has been fabricated and delivered in the second part of 2011. Signals from an ^{55}Fe source measured with the ASIC prototype connected to the illuminated straw tube, for different settings of the ion cancelation network, are shown in Fig. 4.5. It is seen that, with optimized parameters of the network, the long tail can be eliminated.

Preliminary measurements of the front-end gain and noise are shown in Fig. ?? and Fig. 4.7. The gain characteristics have been measured with a step-like voltage pulse injected into the ASIC channel via a capacitance ("delta-like" pulse).

Both results stay well within the requested specifications. The discriminator circuit uses a simple leading edge configuration. A preliminary measurement of the discriminator time-walk, shown in Fig. 4.8, shows the typical leading edge behavior.

The charge vs Time Over Threshold (TOT) behavior of the ASIC is shown in Fig. 4.9. It has been measured with "delta-like" pulses for an input charge range of 10-80 fC. It shows a non-linearity

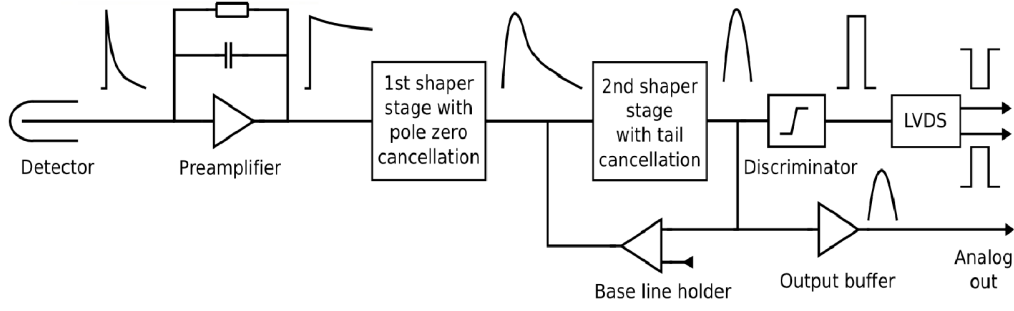


Figure 4.3: Block diagram of ASIC proposed for straw-tube read-out

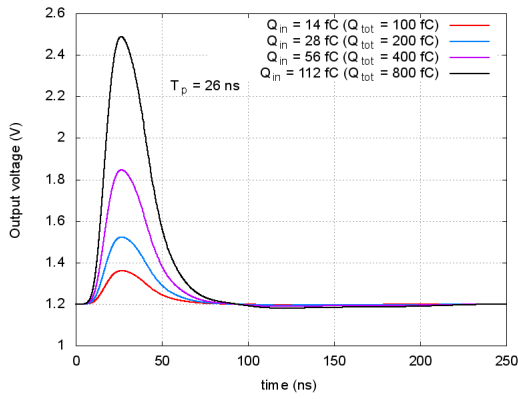


Figure 4.4: Examples of the simulated analog responses for different input charges.

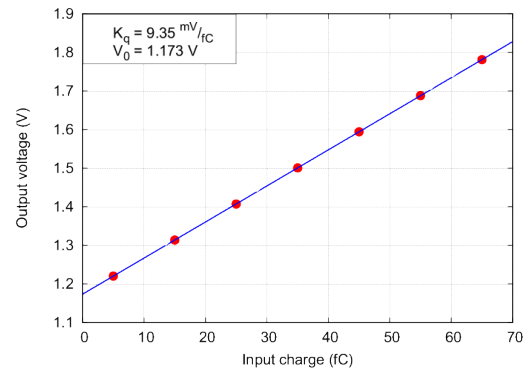


Figure 4.6: Examples of the front-end gain measurement for default settings with 'delta-like' current pulses.

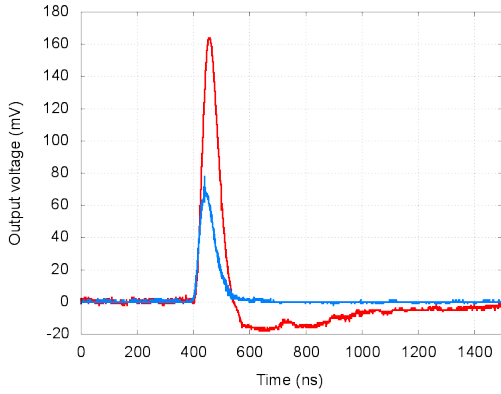


Figure 4.5: Examples of front-end pulses for not optimized (red) and optimized (blue) settings of the ion cancellation network.

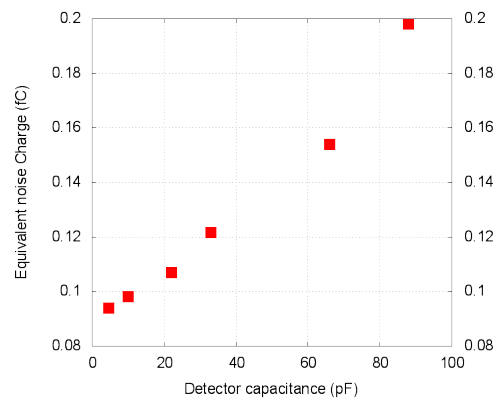


Figure 4.7: Examples measurement of the front-end noise vs input capacitance.

which is typical for gaussian like pulses. It can be optimized in a future version by implementing a linear discharge of the front-end output capacitance. A discharging capacitance by a constant current provides a linear shape of the analog pulse and then the width of the discriminator response may be proportional to the collected charge. A sim-

ilar idea was successfully used in previous reported designs [?, ?].

However, it should be noted that already with the present design, the amplitude spectrum measured with an ^{55}Fe source exhibits two clearly separated peaks corresponding to the characteristic 2.9 and 5.8 keV energy deposits of the source, as shown in

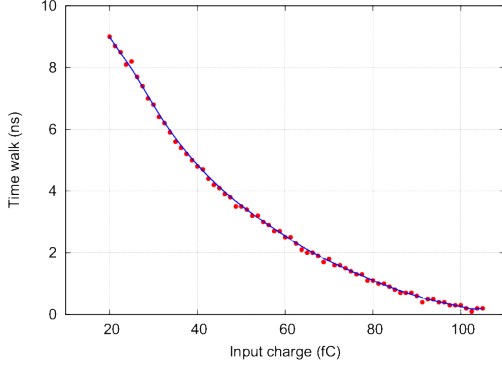


Figure 4.8: Example measurement of the discriminator time walk.

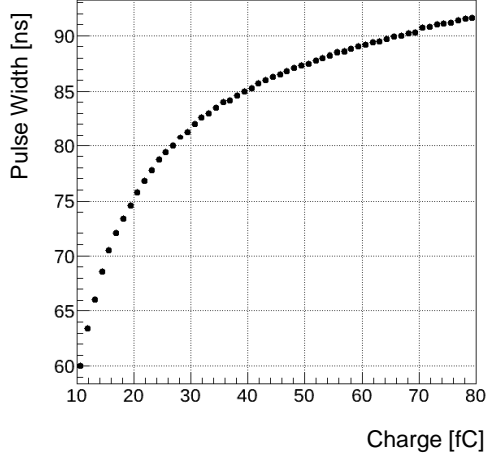


Figure 4.9: Time-over-threshold vs charge measured with "delta-like" current pulses.

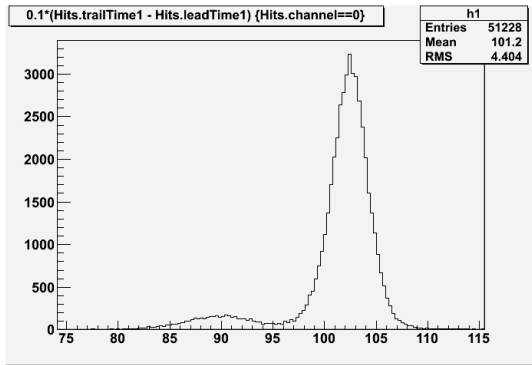


Figure 4.10: Time-over-threshold spectrum measured with an ^{55}Fe source and the straw tube at HV=1750 V.

Fig. 4.10. Further simulations are needed to answer the question whether the present non-linearity is acceptable for particle identification without losing too much performance.

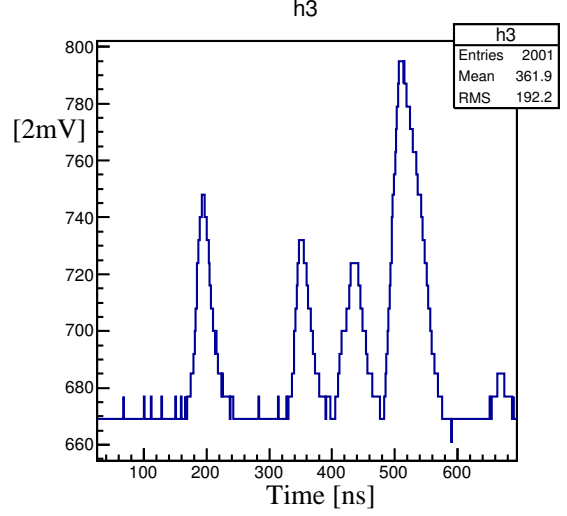


Figure 4.11: Example of the ASIC analog signal output measured at a high (few MHz) hit rate.

Despite the expected large counting rate and long time constant related to the ion propagation it is very crucial to demonstrate that the ion tail cancellation and the base holder circuits work according to the design. Recently, first measurements with a high-intensity proton beam were performed in Juelich in order to verify the signal readout at high rates. As an example, Fig. 4.11 shows the analog output of the ASIC recorded by an oscilloscope. No baseline distortion and a clear separation of the four individual signals can be seen within a time window of about 700 ns, which corresponds roughly to a proton rate of 6 MHz in the single straw.

A further optimization of the ASIC with a systematic study of the design parameters is still going on. In addition, a thorough analysis of the two different methods of the signal amplitude measurement will be done by comparing the TOT information with the analog signal shape, which are both provided by the ASIC. Depending on the result, the final architecture of the ASIC-chip including the specific method for the amplitude measurement will be determined.

Apart from the not yet decided method for the amplitude measurement, some other design aspects have to be considered. In particular the DAC converters need to be designed and added to each channel in order to tune independently the discrimination threshold of each channel, the reference voltage source needs to be designed and added, the digital part of the ASIC needs to be implemented. Although the present ASIC was designed in 0.35μm technology, the final technology choice has not yet

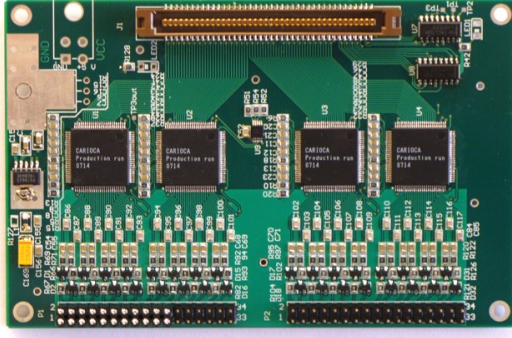


Figure 4.12: Prototype board of a 32-channel preamplifier/discriminator based on CARIOCA-10 chips.

been done. The final ASIC will probably contain 16 channels.

The multi-layer printed circuit board (PCB) for the FEE will contain 2 to 5 ASICs (for 16 channels each), a dedicated logic for the ASIC configuration and connectors for flat twisted-pair cables with signal inputs (for slow control) and outputs to the DB. The inputs from the single straws will be provided by thin single-ended, coaxial cables. Since the mechanical frame structure of the STT has two support flanges with a six-fold symmetry, a back plane with the analog read-out will be composed out of six independent sectors, each serving 768 straws. Thus, 13 FEE boards with a varying number of channels, from 36 (innermost) to 80 (outermost), are needed for the read-out of one complete sector.

During the design phase of the new ASIC several FEE prototypes, based on CARIOCA chips, have also been tested with prototype chambers and showed satisfactory performance.

The CARIOCA is an 8 channel, radiation hard (up to 20 Mrad dose) ASIC, featuring preamplifier, shaper, base line restorer and discriminator. One single FEE board consists of four CARIOCA chips for the read-out of 32 channels. The FEE board provides a LVDS differential output which is connected by a flat cable to the DB. The threshold for the CARIOCA's leading-edge discriminators is set by the on-board DAC, which is controlled by dedicated lines in the cable connection to the DB. The total power consumption per channel of the CARIOCA chip is 25 mW.

The most recent, second version of the preamplifier/discriminator board is shown in Fig. 4.12. Its basic parameters are given in Table ??.

The main limitation of the CARIOCA chip is the lack of the signal amplitude information which is

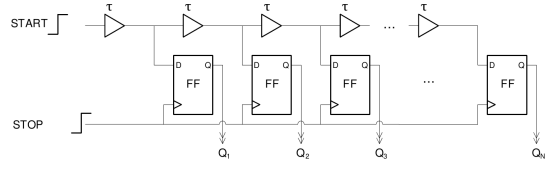


Figure 4.13: Scheme of TDC-FPGA implementation with carry chain usage.

crucial for the STT for the dE/dx measurement. However, it is still considered as a back-up solution for the \bar{P} ANDA Forward Tracker (FT) where a dE/dx measurement is not required.

4.2.4 Time-to-digit converters

The DB readout will be located 2-3 meters outside the chambers. It will contain multi-hit TDC measuring the signal arrival time with respect to the external clock provided to the DB by the \bar{P} ANDA CTDS. For the amplitude measurement and depending on the test results, either the TDC will provide the sufficient pulse length information (TOT) or the DB will contain an additional fast sampling ADC for the analog signal.

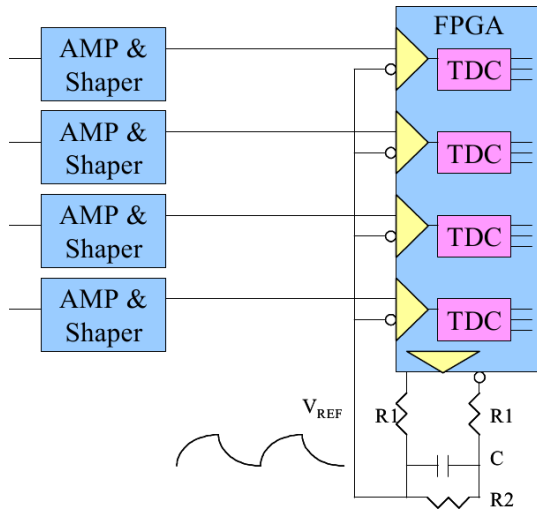
A time measurement system based on FPGA is foreseen for the FT. Recently, a time measurement board (TRBv3-see below) based on the Lattice ECP3 family, has been developed at GSI, University of Frankfurt and Jagiellonian University. The implementation of a TDC in FPGA allows for a large flexibility in the selection of main measurement parameters like time range, binning etc., and makes this approach very attractive for a broad range of applications. The implementation of the TDC functionality in FPGA is achieved by using its internal architecture elements - carry chains [?], [?], [?].

As presented in Fig. 4.13, the time measurement is based on the information (from the carry chain - START signal in Fig. 4.13) saved in the flip-flops ($Q_1 - Q_n$) on the rising edge of the system clock (STOP signal in Fig. 4.13). Each carry chain element delays the signal in average by 30 ps. Time measurements done at GSI demonstrate a ~ 17 ps resolution. For the STT detector, a TDC binning of 0.5 ns will be sufficient. To have all needed information about the signal from the detector it will be required either to measure the amplitude/charge of the straw signal via TOT or even, if it will turn-out necessary, sample its shape. This is possible since the FEE-ASIC can provide both, the digital (time and TOT) and analog signals.

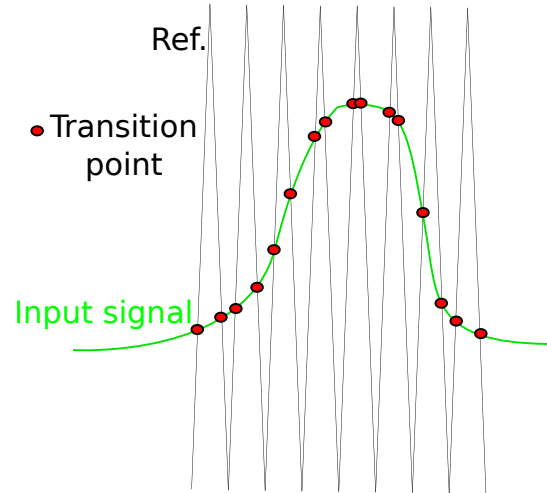
General parameters	Number of channels Radiation resistance Technology	8 20 Mrad IBM CMOS 0.25 μm
Input parameters	Input impedance Range of input charge Peaking time Sensitivity with detector capacitance 220 pF for positive input negative input Width of output pulse for charge < 300 fC at positive input negative input Minimum charge positive input negative input	45 Ω 2.5 \div 300 fC 14 ns 8.21 mV/fC 7.7 mV/fC 55 ns 65 ns 2.4 fC (rms 0.37 fC) 2.4 fC (rms 0.24 fC)
Output parameters	Standard of pulses	LVDS

Table 4.4: Basic technical parameters of the CARIOCA-10 chip.

Supply voltage	+4.5 \div +12 V DC
Supply current	560 mA
Power consumption	3.3 W
Number of channels	32
Dimensions of board	124 mm x 80 mm x 16 mm

Table 4.5: Technical characteristics of the prototype preamplifier/discriminator board - version-2.**Figure 4.14:** ADC-FPGA implementation [?].

Therefore, along with the development of the TDC-FPGA measurement techniques the utilization of the ADC functionality into the FPGA is under

**Figure 4.15:** Example of the input and reference signal. The red points mark the transition point when the FPGA should see a change from the logical 0 (1) to the 1 (0) level.

investigation. The TDC implementation together with just a few components (resistors and capacitors) allows to perform an additional ADC measurement. Fig. 4.14 shows a scheme of such an approach. The differential input of the FPGA is used as a comparator. If a defined signal generated by the FPGA (V_{ref} in Fig. 4.14 and Fig. ??) is larger than the input signal, the FPGAs logic sees a 0, otherwise a 1 level. The transitions from the 0 to the 1 level are again saved in the flip-flops chain (see Fig. 4.13). At the end the time measurement of the

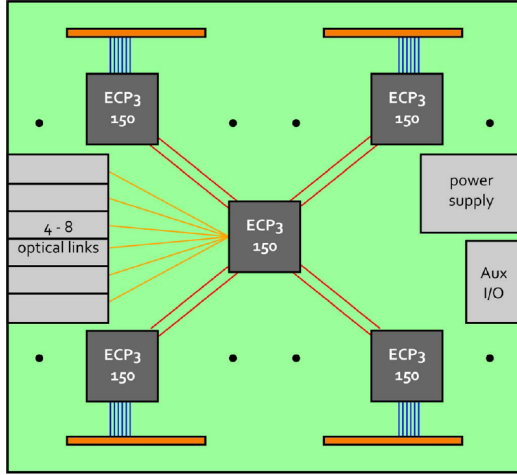


Figure 4.16: Block diagram of TRBv3.

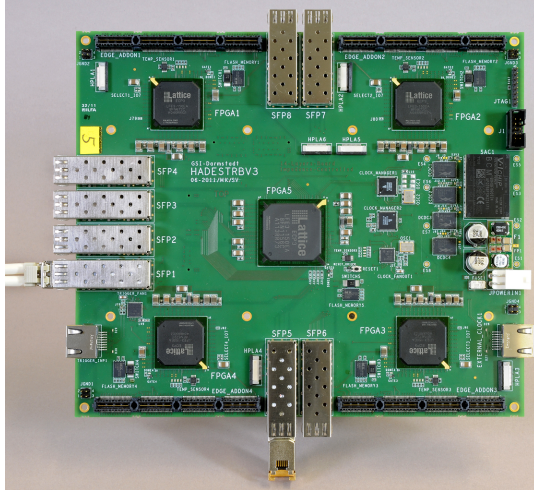


Figure 4.17: Produced TRBv3 board.

transition can be translated to a voltage. The advantage of this solution compared to the usage of a standard sampling ADC is the smaller power consumption and price. The decision about the final method of the ADC measurement will be taken after thorough tests. Consequently, appropriate mezzanine cards will be build. Such mezzanine cards can be added as an add-on to the basic Time Read-out Board (TRB-see below) containing the TDC.

The block diagram and a recently produced TRBv3 board are shown in Fig. ?? and Fig. ??, respectively. Four out of five FPGAs on the TRBv3 are located along the edges of the board. Each of them has a 208-pin input/output connector assigned. The fifth FPGA is located in the center of the board and coordinates the work of the edge FPGAs as

well as communicates with the data acquisition system. The TRBv3 board is equipped with eight optical SFP connectors. The maximum transmission speed of each optical connector is 3.2 Gbit/s. The input/output connectors are used to plug in mezzanine cards. The connector contains 188 general purpose lines and 6 high speed serial connections between edge FPGA and a mezzanine board. Eight lines are connected to the central FPGA from each connector. The design of the mezzanine card is left for future TRBv3 users. It may differ from a simple flat cable adapter to a sophisticated board (e.g multichannel ADC). A set of two connectors is placed on the bottom side of the TRBv3 allowing for yet another mezzanine card connection. All 160 general purpose lines from the bottom connectors are controlled by the central FPGA. Both top and bottom connectors provide a power and ground for mezzanine cards.

The edge FPGA may contain up to 64 time measurement channels. The DB based on TRBv3 for the STT will have 48 TDC channels in FPGA, giving the total number of 192 channels per board. Thus, four TRBv3 boards will be sufficient to collect data from one STT sector.

The former version of the TRB (TRBv2), containing four HPTDC chips is presently used for straw detector tests (as for example shown above). It has been built for the HADES experiment at GSI [?] (schematics and photograph of TRBv2 are shown in Fig. ?? and Fig. ??, respectively). The HPTDC chip (32 channels) has been developed at CERN for LHC experiments. The HPTDC can operate with a maximum trigger rate of 1 MHz and a maximum of 2 MHz hit rate per channel. Four TDC binning widths (25, 100, 195 or 785 ps) can be selected by software during the chip initialization. For the straw tubes, a binning of 785 ps has been selected. The measured hit times together with the trigger time stamp are stored in the local TDC memory (up to 256 hits/shared by 8 channels can be stored) and read-out from the TDC read-out FIFO (also 256 hits deep) with 40 MHz clock (8 bit parallel bus). Noise suppression and a fast hit detection on single wires is performed in FPGA located on the board. The HPTDC allows also to measure the time over threshold which is used for a noise suppression. The FPGA controls also the data flow. The data are transmitted from the DB via 8b/10 serial 2.5 Gbit optical link driven by TLK2501 transceiver from Texas Instruments.

For tests an external trigger (clock) was connected to the TRBv2 by a dedicated line, not shown in the schematics. The slow control is provided by

the Etrax FS CPU running LINUX OS and EPICS client.

4.3 Data rate

An average maximum hit rate of 800 kHz per channel is expected for the innermost straws when operating at an interaction rate of 2×10^7 proton-antiproton annihilations per second. One DB, with 196 channels, will provide on average 157 Mhits/s. The TDC will require 11 bits in order to measure a $1 \mu\text{s}$ range with a 0.5 ns binning with. The Time-Over-Threshold will require 8 bits to cover a range up to 200 ns. The channel number (1-48) will require 86 bits and the encoding of the time stamp (1-500) will require 9 bits. The latter assumes that epoques of $500 \mu\text{s}$ are stored in the DB buffer. Sufficient memory (400 kB) for one epoques can be easily implemented in the FPGA.

Altogether 34 bits represent one TDC channel result in a given TDC on the DB. Two more bits are necessary to distinguish the FPGA. Thus a 5 byte word is generated for each hit on the DB. Assuming 800 khits per second a data rate of 4 MB/s is generated in each TDC channel. This results in a 784 MB/s data rate from one DB. This data rate can be handled by four 3.2 GBit/s optical serial links. Twenty four 196-channel DBs will be necessary for the full CT read-out.

It seems reasonable to merge the data from the straw layers belonging to one STT-sector and sent them to a common DCB. Such a layout can be more favorable for a cluster search but is not mandatory since the DB have also features of the Detector Concentrator (grouping of bursts in epoques).

A board which could be considered as a prototype of the PANDA DCB has also been developed by the HADES DAQ group (so called the optical hub module) and is currently installed in the Krakow straw tube test set-up. The prototype is equipped with several Small Form-factor Pluggable Transceivers (SFTP) serving as optical connectors and FPGAs controlling the data transfer. An attractive feature of this unit is the possibility to create groups of links (4 in the present prototype) into one protocol standard. This is provided by FPGA controlling data flow (*i.e.* Lattice SCM 50 chip) which currently supports 8b/10b and GBit Ethernet format. Optical links used on this prototype can send data with a maximal speed of 3.8 Gbit/s.

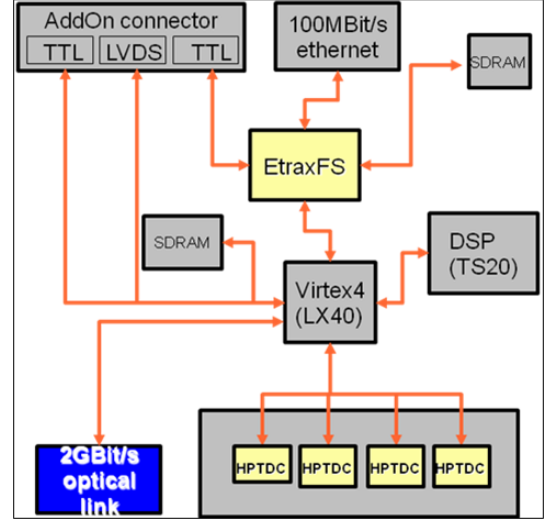


Figure 4.18: Schematics of the TRBv2 HADES board used for the time-of-flight measurements.

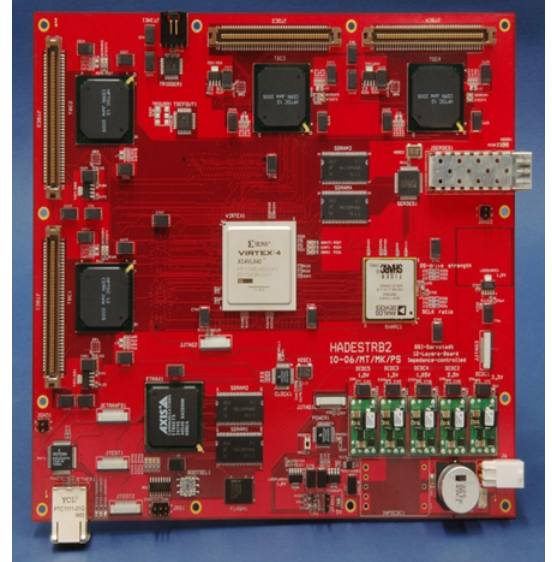


Figure 4.19: HADES TRBv2 board.

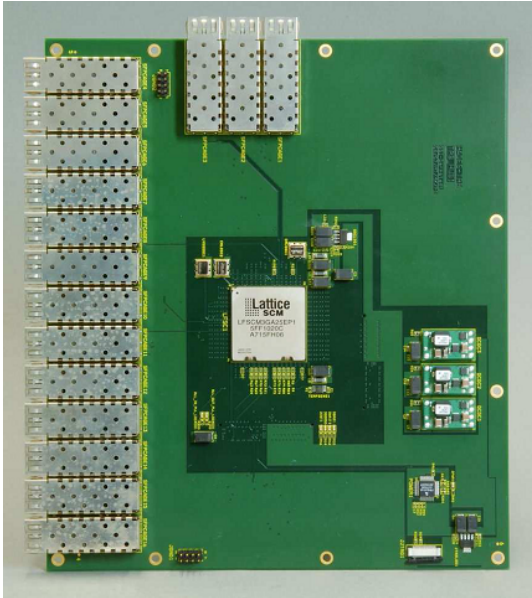


Figure 4.20: Optical HUB board for the HADES experiment.

4.4 The power systems

4.4.1 High-voltage system

4.4.2 Low-voltage system

4.5 Detector integration

4.5.1 Mechanical supports

4.5.2 Cables routing

4.5.3 Gas tubes routing

4.5.4 Installation and alignment

4.5.5 Access

4.6 Monitoring

5 Tests of prototypes

5.1 Jülich small-scale setup

5.1.1 Experimental setup

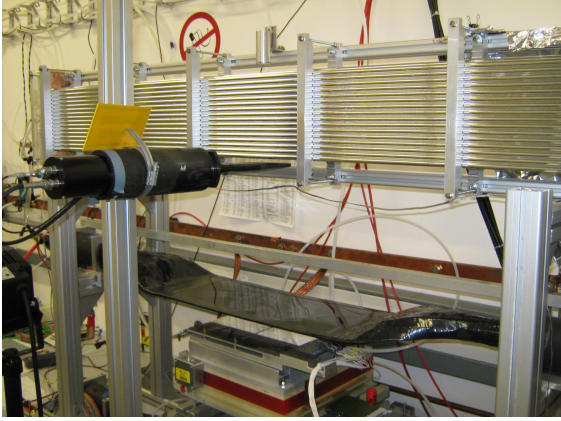


Figure 5.1: Straw tube prototype used at the Institut für Kernphysik at Forschungszentrum-Jülich. Design and construction by IKP-Jülich.

The setup is shown in Fig. 5.1: it consists of a dense array of 128 PANDA-type straw tubes, arranged in four double-layers of 32 straws each. The tubes, with an aluminized mylar wall $30\ \mu\text{m}$ thick, are 150 cm long and have a diameter of 10 mm; in the centre of the tubes, a $20\ \mu\text{m}$ anode wire is stretched. The tubes can be filled with different gas mixtures, like ArCO_2 or ArC_2H_6 (see the detail of the gas manifolds in Fig. 5.2), and can be operated at different conditions of high voltage and pressure. In addition, a drift chamber with two-dimensional readout for particle tracking, a hybrid drift chamber with a GEM amplification stage for clustering investigations and a small straw tube detector (24 cm long, 4 mm diameter) are included [?]. Finally, two scintillators are placed below the double-layers and used for triggering time to select the signal events when a coincidence occurs. Half of the channels are equipped with the amplifier-discriminator chip CMP16¹ connected with the 64 channels time-to-digital converter based on the F1 TDC chip of the type used at WASA-at-COSY [?]. The anode signals of the other 64 channels are processed by modular fast current amplifiers with 8 ns rise time; thus, individual cluster or groups of few overlapping clusters created along the ionized track became visible in the signal structure. The flash charge-to-digital

converters FQDC analyse signals in terms of charge and pulse-height and disentangle signals into components originating from ionized clusters or groups of clusters in gaseous detectors. The FPGA² controlling the readout of the QDC module are programmed for high flexibility to permit also total readout in the “oscilloscope mode” and to record single spectra in a self triggering mode for calibration measurements with $\text{Fe-55}\ \beta^+$ sources. In view of the limited number of oscilloscope channels several amplifiers were fed via analog OR into the oscilloscope and then the data were transferred to a computer.

The actual number of firing straws in each event can be deduced from a multiplicity signal delivered by the 8-channel discriminator [?].

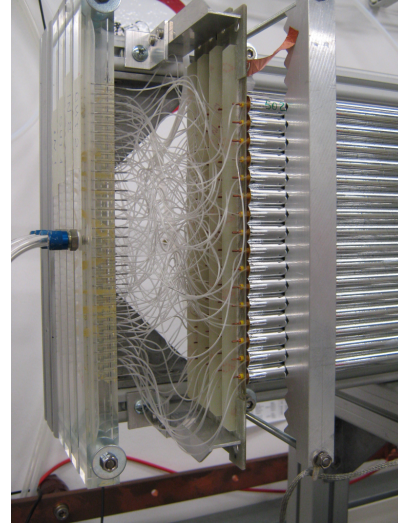


Figure 5.2: Detail of the prototype shown in Fig. 5.1.

5.1.2 Spatial resolution

By analyzing the experimental data sets collected with the straw tube prototype described above, it has been possible to derive the spatial resolution σ

1. The CMP16 board is based on an analog-to-digital converter chip with 16 channels which transforms analog signals to LVDS (Low-voltage Differential Signaling) standard. It can run at very high speed at reduced electromagnetic noise. The transfer characteristics of the amplification and discrimination are presented in [?]

2. Field Programmable Gate Array.

for single straw tubes shown in Fig. 5.3 as a function of the drift distance [?]. It has been obtained in the

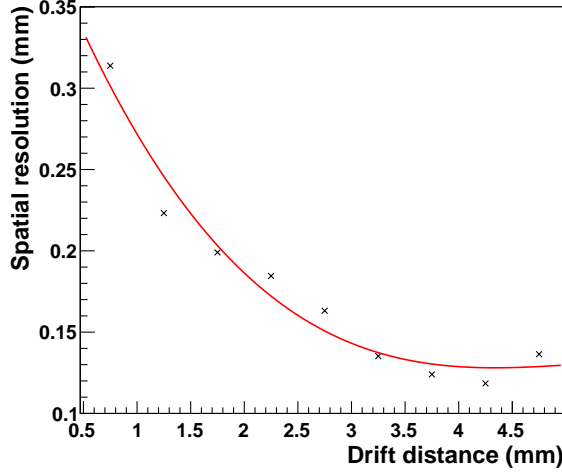


Figure 5.3: Mean spatial resolution σ for single tubes, obtained as explained in the text. The red line is the fit with a third order polynomial.

following way: after the last iteration of the autocalibration procedure (Sec. ??-insert proper reference), the tracking has been performed and a track hypothesis has been found, event by event. Depending on the track to wire distance, the corresponding distribution of the residuals has been filled.

For each interval, the obtained residual distribution has been fitted with two functions (two Gaussian or one Gauss function and a third order polynomial) in order to better describe both the peak and the tails of the distribution. An example of residual distribution for one interval is shown in Fig. 5.4.

The values of σ of each Gauss function that fits the peaks of the residual distributions has been then used to derive the single tube resolution shown in Fig. ??.

The mean value of the spatial resolution curve is in agreement with the deviation σ of about $177 \mu\text{m}$ (parameter p_5 of the fit) of Fig. 5.5. It shows the distribution of the mean residuals of 162385 straw hits after the sixth iteration of the autocalibration procedure, whatever the value of the corresponding track to wire distance was.

The distribution has been fitted with two Gauss functions, whose parameters are reported in the statistics box in figure: the first three refer to the Gauss function that fits the tails of the distribution, the other three refer to the one that fits the peak.

The distribution of the residuals is highly symmet-

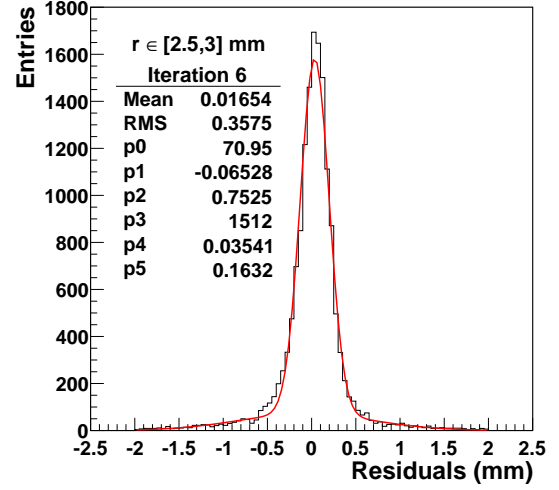


Figure 5.4: Distribution of the residuals for r in the range $[2.5, 3]$ mm at the last step of the autocalibration. The distribution has been fitted with two Gauss functions; the parameters of the fit are in the box (p_3 , p_4 and p_5 are the ones of the Gauss function that fits the peak).

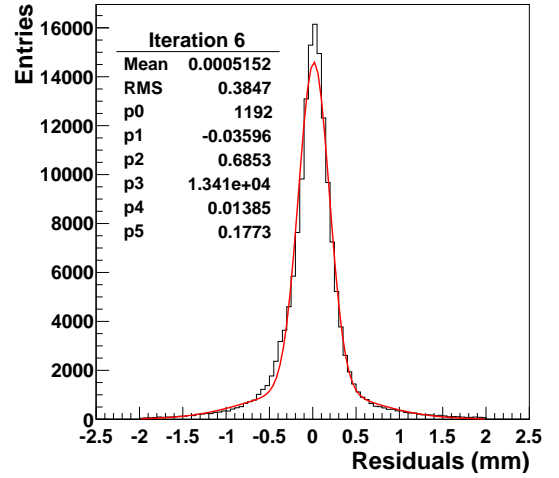


Figure 5.5: Distribution of the mean residuals after the sixth iteration of the autocalibration procedure. The parameters of the fit (red curve) are in the box: p_0 , p_1 and p_2 are referred to the fit of the distribution tails; p_3 , p_4 and p_5 are the parameters of the Gauss function that fits the peak.

ric around a mean of about $14 \mu\text{m}$ (parameter p_4 of the fit), indicating no systematic errors. The deviation σ of about $177 \mu\text{m}$ (parameter p_5 of the fit) is a measure of the mean spatial resolution of a single straw and is compatible with the mean of the resolution curve in Fig. ??.

The obtained spatial resolution is strongly affected

by the time resolution of the electronics the prototype was equipped with. Therefore, by using a dedicated electronics a better single tube resolution will be achieved.

5.1.3 Single tube resolution

The single tube resolution as a function of the drift distance obtained in the way previously described is “biased”, since the tube whose resolution we are studying has not been excluded from the tracking. In addition, the errors on the parameters of the best fit line have not been subtracted.

In order to calculate the “unbiased” spatial resolution σ of a single tube, another method has been implemented and used. First off, tracks with $N \geq 16$ hits have been selected and fitted using $N - 1$ space points. Then, the distribution of the residuals for the tube excluded from the fit has been computed as a function of the drift distance (see Fig. 5.6).

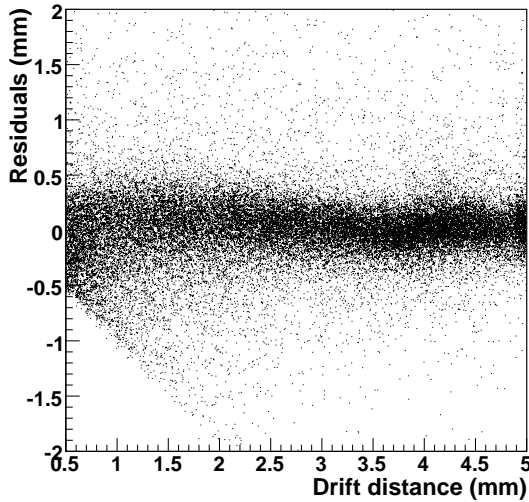


Figure 5.6: Residuals vs. drift distance.

This distribution is the convolution of the resolution of the tube and the track extrapolation errors, due to the fit. In fact, both the intercept a and the slope b of the best fit line are affected by an error σ_a and σ_b , respectively, given by the covariance matrix of the Minuit fit in the refit step. Their correlation is expressed by the term $\rho \doteq \sigma_{ab}^2$. So the error on the distance of each point (x, y) to the best fit line can be computed as:

$$\sigma_d^2 = \left(\frac{\partial d}{\partial a} \right)^2 \sigma_a^2 + \left(\frac{\partial d}{\partial b} \right)^2 \sigma_b^2 + 2\rho \frac{\partial d}{\partial a} \frac{\partial d}{\partial b} \quad (5.1)$$

where

$$\frac{\partial d}{\partial a} = -\frac{1}{\sqrt{1+b^2}}, \quad (5.2)$$

$$\frac{\partial d}{\partial b} = -\frac{x+by-ab}{(1+b^2)^{3/2}}. \quad (5.3)$$

In order to disentangle the intrinsic resolution of the tube from the other contribution, we have proceeded in the following way.

First off, the distribution of Fig. 5.6 has been sliced; for each interval, the residual distributions have been fitted with two Gauss functions, as in Fig. 5.7, and the mean value of σ_d has been calculated with Eq. 5.1, using all the space points belonging to that interval. Then, interval by interval, the obtained mean value of the error on the distance σ_d has been quadratically subtracted to the σ of the Gauss functions that fit the residual distribution of that interval.

The obtained values of σ are the ones used for the single tube spatial resolution, shown in Fig. 5.8.

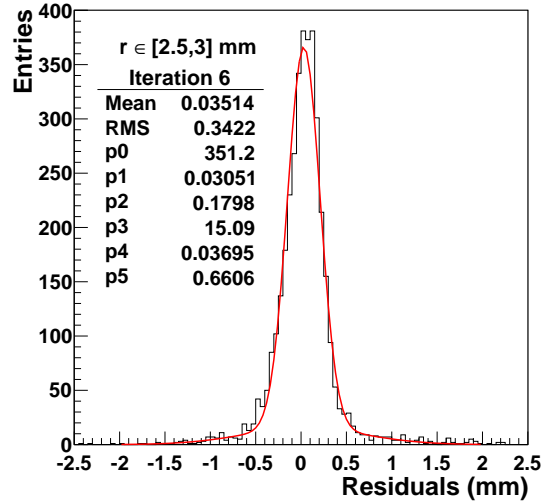


Figure 5.7: Distribution of the residuals for r in the range $[2.5, 3]$ mm after the sixth iteration of the auto-calibration, in case the hit tube is taken out from the track reconstruction (it is the analogous of Fig. 5.4). The distribution has been fitted with two Gaussian; the parameters of the fit are in the box (p_0 , p_1 and p_2 are the ones of the Gaussian that fits the peak).

5.1.4 Contribution of tubes mispositioning to spatial resolution

The resolution shown in the previous paragraph is the sum of two contributions:

$$\sigma_{overall}^2 = \sigma_{cal}^2 + \sigma_{pos}^2, \quad (5.4)$$

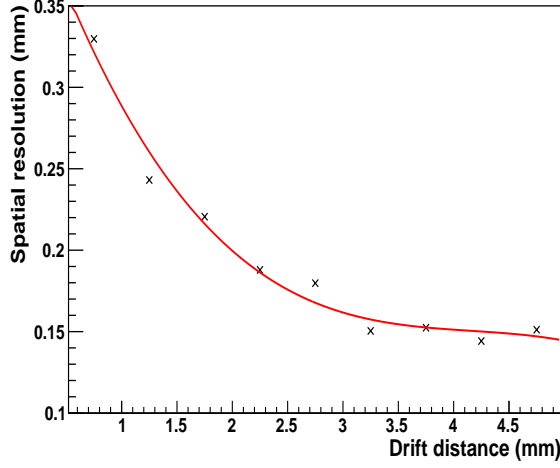


Figure 5.8: Single tube spatial resolution σ as a function of the drift distance.

where σ_{cal} contains the contribution of the calibration but also of the electronic time measurements, primary ionization cluster effect and gas diffusion effect and σ_{pos} is due to the wire mispositioning ($\simeq 50 \mu\text{m}$). In the following, it is explained how the last contribution has been estimated.

For each track, all the tubes have been taken out from the track reconstruction one by one and the distribution of the residuals of the single tubes has been computed. Fig. 5.9 shows two examples of residual distributions for two tubes: (a) tube 3 in layer 0 and (b) tube 7 in layer 2. The mean value of each histogram is a measure of the mispositioning of the single straws: if the wire positions were correct, the distributions should be centered around 0. As it is clear from Fig. 5.9.a, it does not always happen: in particular, in this case, the mispositioning ranges from few micrometers to more than $150 \mu\text{m}$. The displacements from 0 are taken into account with their sign, meaning that the wires are shifted to the right and to the left with respect to their nominal positions.

To have an idea of the mean position error, the distributions of the residuals for each tube have been fitted with two Gauss functions and the mean values of the one that fits the peak have been reported in Fig. 5.10.a: the mean wire deviation is about $14 \mu\text{m}$, which is negligible. This is in agreement with the mean value of the residuals shown in Fig. ?? ($13.85 \mu\text{m}$). These deviations are within $50 \mu\text{m}$, as indicated by the RMS of the figure; this value is comparable with the mean of Fig. 5.10.b, where the absolute values of the wire deviations are reported. With $\sigma_{pos} \sim 50 \mu\text{m}$ and $\sigma_{overall} \sim 177 \mu\text{m}$ (see σ

of the distribution in Fig. 5.5), it results:

$$\sigma_{cal} = \sqrt{\sigma_{overall}^2 - \sigma_{pos}^2} \simeq 170 \mu\text{m}. \quad (5.5)$$

So the main contribution to the overall resolution comes from the calibration and the position error has a very small influence on the global one. Hence, it is not necessary to iteratively correct the wire position of the individual straws.

5.1.5 Detector performance at high counting rates

The results described above were obtained with monoenergetic beams of protons of intensity up to $\cdot 10^4$ protons/s. At $\bar{\text{PANDA}}$ the experimental conditions foreseen predict for the innermost layer of $\bar{\text{PANDA}}$ -STT a load up to 0.8 MHz/straw. Therefore, the problem of stability and quality of the output signals at such extreme conditions has been addressed as well. The experimental setup was exposed to a proton beam of momentum of 2.7 GeV/c of intensity up to 2.4 MHz. The actual beam intensity was monitored by counting the signals of each of the first straw in the layer. Due to the high beam divergence a stable high intensity beam could not be kept on the whole detector. Therefore, a variation of the instantaneous beam intensity was observed, that can even better simulate the experimental conditions at $\bar{\text{PANDA}}$. Examples of the spreads of the beam intensity are given in Fig. 5.11.

The short integration constant of the front-end electronics permits to observe an almost undistorted shape of the anode current signal of the straws. These shapes were recorded by means of 240 MHz flashADC in long, $5 \mu\text{s}$ windows. Fig. 5.12 shows the signals recorded for one complete layer (16 straws) of STT prototype. The individual groups of signals may consists of up to 16 components.

During the high intensity test none of the unfavorable phenomena, expected when some ionization density in the detector volume is exceeded, were observed. Even at very high beam intensities of 2.2 MHz, which are significantly beyond the expected rates of operation of the $\bar{\text{PANDA}}$ -STT, the signal's baseline was stable. No onset of space-charge effect was recognized as well. At the normal operational voltage with particle fluxes of the order of 0.8 MHz/straw, both space- as well as energy resolution of the tracker will not be deteriorated.

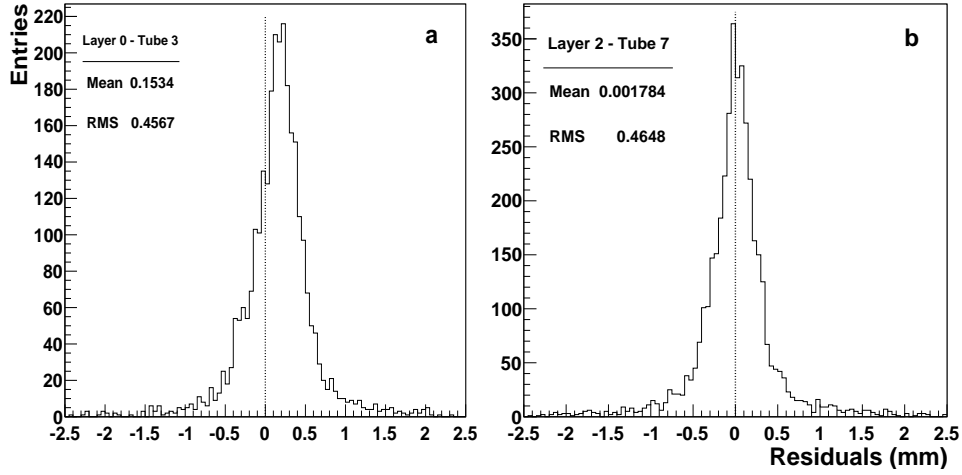


Figure 5.9: Examples of residual distributions for single tubes, which have been taken out from track reconstruction: (a) tube 3 in layer 0 and (b) tube 7 in layer 2. The distributions should be centered around 0 (dotted line).

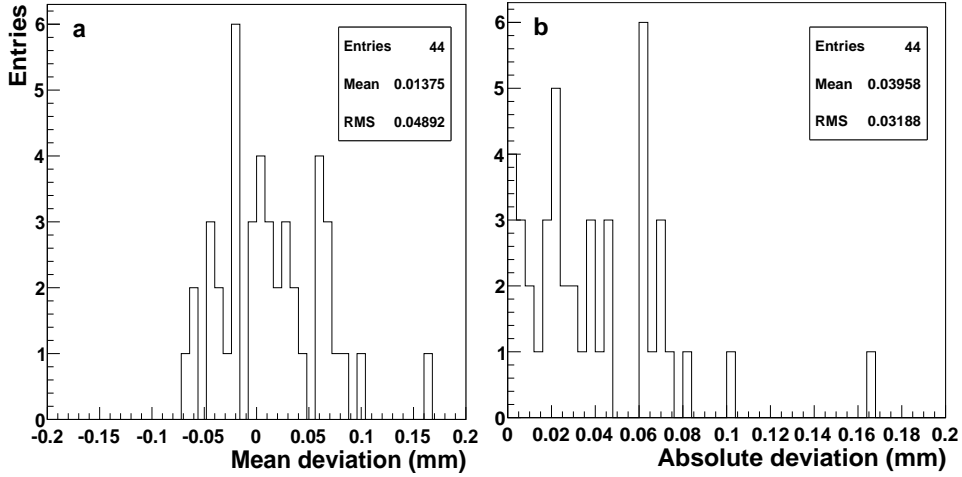


Figure 5.10: (a) Distribution of the mean deviations (with sign) of the wire positions from their nominal ones: this is a measure of the systematic shift of the wires. (b) Distribution of the absolute values of the deviations plotted in (a).

5.1.6 Aging tests

A degradation of the straw tube properties like a specific gas gain reduction or high voltage instabilities during operation caused by irradiation is expressed as aging. In general, aging is induced by the plasma-chemical processes during the gas amplification processes with a high density of ions, electrons, excitation photons, free radicals and possible molecular dissociations and polymerizations. A complete overview and description of the aging phenomena in gaseous detectors can be found in [?] which is a summary of a dedicated workshop with about 100 detector experts, held at DESY (Ham-

burg, Germany) in 2001. In the following the main aspects relevant for the \bar{P} ANDA-STT are discussed.

Two main sources of aging have been identified in wire chambers. A growth of polymeric deposits on the electrodes which can change the electric field, create sparking, produce dark- or even self-sustaining (Malter) currents. At high irradiation densities and high gas gains already trace contaminations on the sub-ppm level in the gas can lead to such deposits. Another aging source is a possible oxidation of the sense wire. Usually the wire is protected by an outer gold-plating layer which makes the wire highly inert to chemical reactions. If oxy-

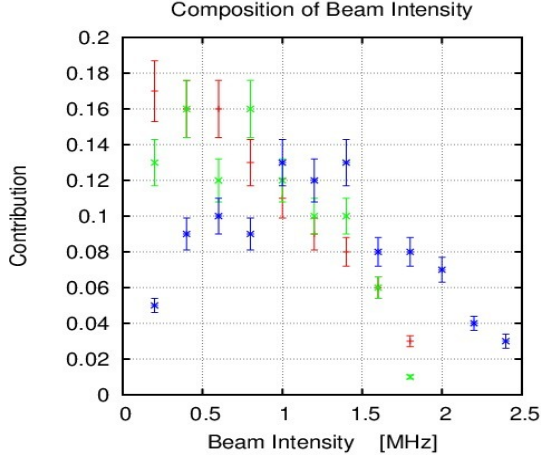


Figure 5.11: Examples of beam intensity variation during the high rate test of the $\bar{\text{PANDA}}\text{-STT}$ prototype. Different colors give the distributions of beam intensity measured on different straws. Beam intensities greater than 1 MHz/straw were observed.

gen produced in the amplification avalanche penetrates through the gold-layer to the inner wire by permeation or at imperfection spots (holes) it can oxidize the wire with a swelling of the inner wire diameter and a cracking of the gold-plating layer [?]. The increased wire diameter reduces the gas gain at a given voltage by the lower electric field strength on the wire surface. A quantitative description of the aging process is difficult due to the high complexity with an influence for instance of the gas mixture and purity, trace contaminations, construction materials, gas flow, irradiation area and intensity, ionization density, high voltage setting, particle type and energy.

The proposed Ar/CO₂ gas mixture is known as being one of the best gas mixtures for high-rate hadronic environments due to the absence of polymerisation reactions of the components. Contaminations of the gas or detector materials with silicone, e.g. from lubricants must be avoided, since they produce a strong growth of non-volatile SiO₂ crystals on the wire. An admixture of CF₄ to the gas can remove such SiO₂ deposits, but due to its high additional wire etching capability special care is needed. Hydrocarbons are better quenching agents compared to CO₂, but not considered for the $\bar{\text{PANDA}}\text{-STT}$ because of their high polymerisation rate, which can lead to deposits on the electrodes. In particular deposits on the cathode can produce self-sustaining currents with a possible high voltage breakdown (Malter-effect) [?]. In general a moderate gas gain of about 5×10^4 is recommended which

reduces the occurrence of limited streamer mode pulses with an increased avalanche size and possible accelerated aging [?].

The behaviour of the straw tubes under very high irradiation was studied at COSY with a proton beam. The goal was to check the influence of the beam exposure and charge deposition on the straw gas gain, high voltage operation stability and to verify that all assembled materials including the gas system do not create harmful pollution, e.g. by out-gassing. Within the short time of about 10 days beam irradiation it was possible to collect a charge deposition in single tubes up to about 1.2 C/cm comparable to several years of operation of the $\bar{\text{PANDA}}$ detector at full luminosity.

The straw setup consisted of a planar double-layer of 32 close-packed tubes installed behind the COSY-TOF apparatus and exposed to the residual proton beam with a momentum of about 3 GeV/c. The straw design and all materials were the same as used for the COSY-TOF straw tracker assembly, i.e. 30 μm thick mylar film tubes with 10 mm diameter and a length of 105 cm. For the $\bar{\text{PANDA}}$ detector the same straw tube design is proposed, but with a length of 150 cm. Due to the horizontal placement of the double-layer and a beam spot of about $2 \times 2 \text{ cm}^2$ the particle rate through all tubes was almost the same. The surrounding alignment frame consisted of sandwich bars with a Rohacell core reinforced by Carbon fiber skins [?]. Therefore, interaction of the beam with this low-density foam material ($\rho=0.05 \text{ g/cm}^3$) was negligible.

The gas supply was divided into four parallel gas lines, each serving eight straws. Thus, it was possible to test at the same time straws filled with four different gas mixtures and gas gains with the same particle rates. The chosen gas mixtures were argon based, with different fractions of CO₂ (10% and 30%) and one mixture with 10% ethane. The gas pressure for all mixtures was 1650 mbar. The typical gas flow was one volume exchange per hour. In total, 16 high voltage supply channels (one channel per two straws) allowed to operate the straws at different voltage levels and gas gains. The current of every voltage channel was monitored with a resolution of 2 nA. All straws were equipped with preamplifiers and 30 m long signal cables ending in the counting room. Therefore, it was possible to check analog signal shapes and signal rates during beam irradiation for every straw. Table ?? lists the straw settings during the beam test.

The expected particle rates for the individual tubes in the $\bar{\text{PANDA}}$ central tracker volume were derived from a simulation of $\bar{p}p$ interactions and assum-

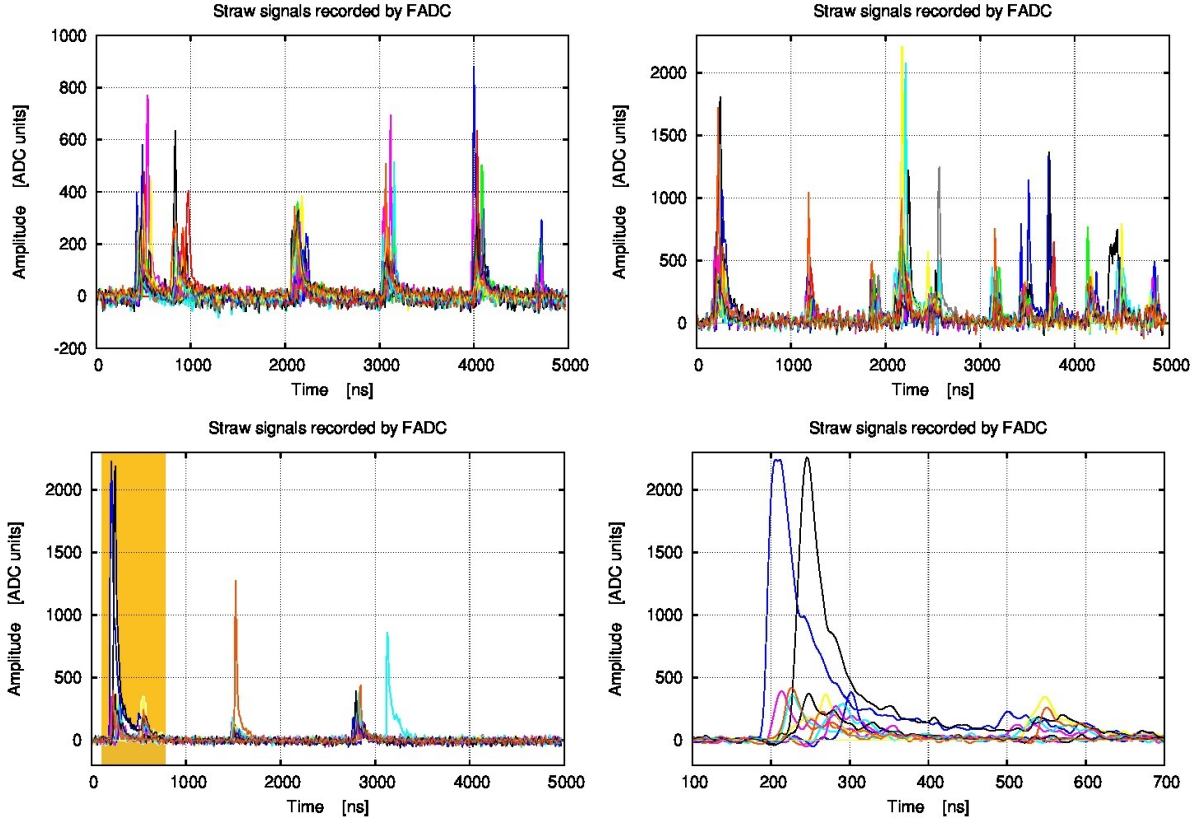


Figure 5.12: Signals from straw tubes recorded in $5\ \mu\text{s}$ windows of 240 MHz flashADC at high beam intensities: (left-hand side, upper) 6 groups of signals are comprised within the window. The relevant beam intensity is equal to 1.2 MHz; (right-hand side, upper) the same for beam intensity of 2.2 MHz; (left-hand side, lower) example of the signal pileup. Colored region is blown up in the: (right-hand side, lower) blown up region of the neighboring figure presenting the pile-up of the signals. Remarkable is lack of any unfavorable effects like baseline shift or signal shape deterioration even at very high beam intensities.

ing an event rate of $2 \times 10^7\ \text{s}^{-1}$ (see Fig. 5.13). The mean particle flux for straws in the innermost layer was $\simeq 800\ \text{kHz}$ per 1500 mm long tube and about $\simeq 7\ \text{kHz/cm}$ in the forward region ($z > 0\ \text{cm}$). The maximum flux of $\simeq 14\ \text{kHz/cm}$ in the tube was concentrated within $z = 2 \pm 1\ \text{cm}$ (target position at $z = 0\ \text{cm}$) coming from $\bar{p}p$ elastic interactions with a laboratory scattering angle $\theta \simeq 90^\circ$ and relatively low momentum. These particles crossing the tubes around $z = 2 \pm 1\ \text{cm}$ were highly ionizing and produced a high charge load of $\simeq 1\ \text{C/cm}$, if one assumed a typical gas gain inside the tubes of 5×10^4 . At all other positions, which represent 99.7% of the STT volume, the mean charge load was about $0.2\ \text{C/cm}$. All quoted charge loads were equivalent to an expected typical beam time for \bar{P} ANDA of one year with 50% live-time.

The total live-time with beam on the straws was 199 hours after correcting the COSY spill time structure and beam breaks. All straws were exposed to

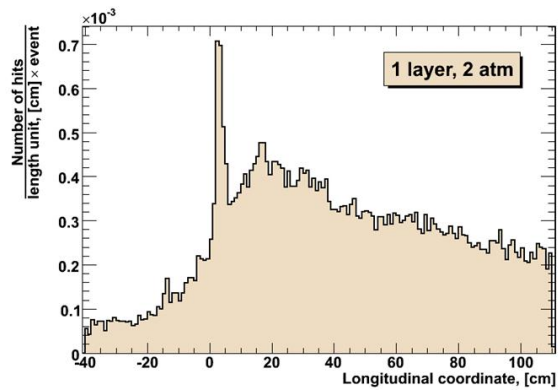


Figure 5.13: Simulation of $\bar{p}p$ reactions and number of hits per event and per cm along the tubes in the innermost layer of the \bar{P} ANDA straw tube tracker. The target position is at $z = 0\ \text{cm}$.

the proton beam at the same longitudinal position, in the middle of each tube. The beam rate and cross section profile was measured by a scintillating fiber hodoscope placed behind the COSY-TOF apparatus and in front of the straw setup. The derived proton intensity per straw diameter during extraction was about $2.3 \times 10^6 \text{ s}^{-1}$. The slightly lower pulse rate of $\simeq 2.0 \times 10^6 \text{ s}^{-1}$ measured for the single straws could be explained by losses of low amplitude signals due to the damping inside the 30 m long cables.

During the beam time no high voltage failures, dark currents or broken wires due to the high charge load were observed. A high maximum current of a single straw wire of up to $2.3 \mu\text{A}$ was measured.

A possible gas gain reduction due to the proton beam irradiation was checked after the beam time by exposing all straw tubes to a ^{55}Fe radioactive source with 5.9 keV γ -emission. In the argon-based gas mixtures the photo-absorption produces a localized ionization spot with a characteristic number of about 220 electrons. Therefore, the recorded signal amplitude height was a direct measure of the gas gain. The amplitude heights were checked for each straw at different longitudinal positions around the beam irradiation spot and normalized to the amplitude heights far from the irradiation spot (see Fig. 5.14). A lower amplitude height indicates a reduction of the gas gain ($\Delta A/A_0 = \Delta G/G_0$). The estimated resolution error of the measurement was about 2 % of amplitude height.

It can be seen that for all straws filled with 30 % CO_2 or 10 % ethane in argon no gas gain reduction was measured, even for the highest charge loads up to 1.2 C/cm. Some but not all straws filled with 10 % CO_2 in argon showed a small gas gain loss of up to 7 % at the beam irradiation spot. A clean spatial correlation between the reduced gas gain and beam intensity distribution, measured by the scintillating fiber hodoscope in front of the straws, was observed. The results of the gas gain measurement together with the total charge loads for all 32 straws are summarized in Table 5.1.

The absence of any aging in the straws filled with ethane or the higher CO_2 percentage in argon indicated no general problem with the gas purity, and a pollution by the used straw materials or gas system could be excluded. The small gas gain reduction observed only for some of the straws operated with the lower 10 % CO_2 admixture might be explained by the known poor quenching capabilities of CO_2 , together with the very high irradiation perpendicular to the wire and concentrated at a small spot of about 2 cm along the wire during the beam test.

Table 5.1: List of straw settings and charge load during the beam test. The last column shows the normalized gas gain reduction in the irradiated straw region with a measurement resolution of about 2%. The aging intervals give the minimum and maximum gain reductions, e.g. 0–7% means that at least one straw showed no gain reduction and one a maximum of 7%.

Straw no.	Gas mixture	Voltage (V)	$\sum Q$ (C/cm)	Aging $\Delta G/G_0$
1–8	Ar/CO ₂ (10 %)	1750	0.72	0–3 %
9–16	Ar/CO ₂ (10 %)	1700	0.58	0–7 %
17–20	Ar/CO ₂ (30 %)	2200	1.23	no
21–24	Ar/CO ₂ (30 %)	2100	0.79	no
25–32	Ar/C ₂ H ₆ (10 %)	1550	0.87	no

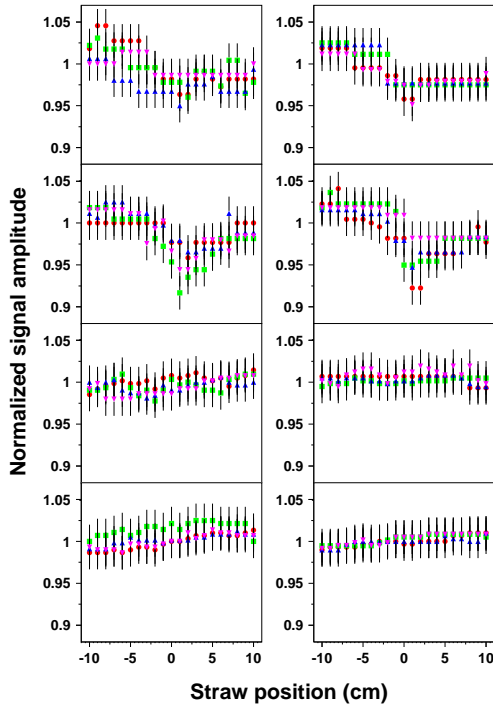


Figure 5.14: Measured normalized gas gain reduction ($\Delta G/G_0$) along the tube for all 32 straws, shown in groups of 4 straws. Straw no. 1–4 (upper left) to straw no 29–32 (lower right). The beam hit all tubes around 0 cm longitudinal position.

result the electric field strength at the wire surface was reduced ($E \propto 1/r$) which lowered the gas gain at the same high voltage setting. Since the observed gas gain reduction was very small the occurring aging processes were rather weak. To clearly identify the sources of aging, dedicated investigations with a higher charge load over a much longer time period would be needed.

Ar/CO₂ is the preferred gas mixture for the \bar{P} ANDA–STT since it is highly tolerant to highest irradiation, not expensive, and non-flammable. The measurements confirm that the straw design and all used materials are suited and will not limit the life time of the detector. No aging in the straws is expected at moderate gas gains of about 5×10^4 for 99.7% of the STT volume during more than 5 years of \bar{P} ANDA operation at full luminosity. A small aging on the low percent level may start first in the region at $z = 2 \pm 1$ cm (= 0.3% of STT volume) after about 2 years of operation, caused by low energy protons from elastic scattering. The modular mechanical design of the \bar{P} ANDA–STT allows to replace even single straws showing aging or other failures inside the layer modules after some years of operation during the \bar{P} ANDA maintenance time.

Due to the incomplete avalanche quenching the occurrence of limited streamer mode pulses, with the characteristic double-peak signal shape, was higher for that gas mixture. The high ionization density with a large number of produced oxygen ions and radicals increased the probability of oxygen permeation through the gold-layer to the inner wire. The oxidation of the inner tungsten-rhenium wire caused a swelling of the wire diameter, and as a

5.2 The COSY-TOF Straw Tube Tracker

The technique of pressurized, self-supporting straw tube layers was first developed for the Straw Tube Tracker of the COSY-TOF experiment (COSY-STT) at the COSY-accelerator (Juelich, Germany). The used straw tube materials and dimensions, and the geometry of planar, close-packed multi-layers are the same or quite similar as for the $\bar{\text{PANDA}}$ -STT. Although the COSY-STT is a non-magnetic spectrometer, the calibration methods for the straw tube positions and isochrone radius - drift time relation are similar for both detectors. The operation of the COSY-STT with about 275 l gas volume in surrounding vacuum is an outstanding technical challenge. The required minimal leakage of the detector in vacuum is a strong and sensitive proof of all straw materials, glueing and assembly techniques, which are also crucial for the $\bar{\text{PANDA}}$ -STT. The COSY-STT is considered to be a global test system for the $\bar{\text{PANDA}}$ -STT and its properties and performance results are summarized in the following.

The COSY-STT was installed in 2009 as an upgrade of the COSY-TOF spectrometer, which consists of a large 25 m³ vacuum barrel with a liquid hydrogen target cell at the entrance, followed by a start detector, silicon-microstrip detector, the straw tube tracker (STT), and scintillator hodoscopes covering the barrel walls and end cap. The apparatus allows to measure kinematically complete the time-of-flight and space directions of the reaction particles of hyperon production in proton-proton and proton-deuteron collisions with polarized proton beam. The vacuum ensures lowest background produced by beam and reaction particles with up to 3.5 m track lengths. More details about the experimental program and the STT installation can be found in [?] and [?]. A first experiment beam time of hyperon production with polarized proton beam was carried out in 2010.

The COSY-STT consists of 2704 straw tubes, each with a length of 1050 mm, inner diameter of 10 mm, and 32 μm wall thickness of aluminized mylar film. The tubes are arranged as a vertical stack of 13 close-packed double-layers with three different orientations ($\phi=0^\circ, 60^\circ, 120^\circ$) for a 3-dimensional track reconstruction. A $15 \times 15 \text{ mm}^2$ beam hole in the center of every double-layer is realized by splitting the 4 central straws into 8 straws with about half length (see Fig. 5.15). The straws are filled with a gas mixture of Ar/CO₂ (80/20%) at a pressure of 1.25 bar. The typical operation voltage is 1840 V. The electronic readout consists of low-power trans-

Figure 5.15: The COSY-STT mounted at the front cap of the COSY-TOF spectrometer. The detector consists of 2704 straw tubes of 1 m length and 10 mm diameter, arranged as a vertical stack of 13 close-packed double-layers at three different orientations.

impedance preamplifiers directly connected to each straw in vacuum and feeding the signals through 13 m coaxial signal cables to ASD8B-discriminators and TDCs, which are located outside the vacuum barrel.

The COSY-STT is now since two years in surrounding vacuum and no real leakage sources of the detector, caused by dissolving glue spots, brittle materials, or loose gas connections, have been observed. The gas leakage stays on the permeation level, which is caused by the flow of the gas molecules inside the straws through the thin mylar film wall to outside vacuum. Fig. 5.16 shows the gas loss by measuring the pressure drop inside the straws in surrounding vacuum if the STT is filled with pure argon and pure CO₂. The difference in the gas loss rate for argon and CO₂ of about a factor of 10 is characteristic for the different permeation of the specific gas molecules through the mylar film and in accordance with reference measurements by the manufacturer (DuPont Teijin Films, USA). For the used gas mixture of Ar/CO₂ (80/20%) the total leakage is about 2 % of the STT volume per day. The typical gas flow during the high voltage operation is about four times the STT volume per day (=1000 l/day).

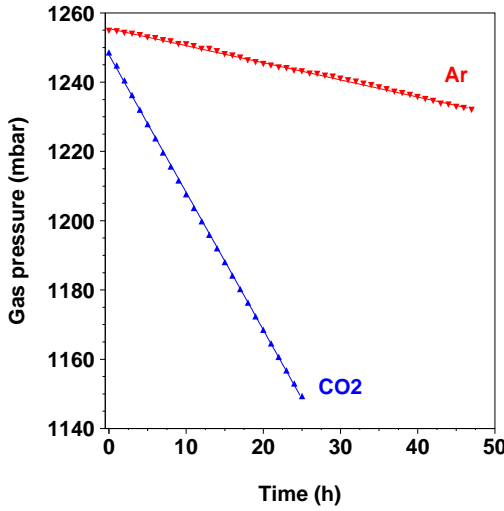


Figure 5.16: Gas leakage of the COSY-STT filled with pure argon (red) and pure CO₂ (blue), measured by the gas pressure drop of the straws in surrounding vacuum.

The calibration of the STT consists of the determination of the isochrone radius - drift time relation and the adjustment of the straw positions and is performed as an iterative procedure. At first, the isochrone - drift time relation ($r_{iso}(t)$ in the following) is parametrized as a polynomial function of 4th order and obtained by an integration of the time offset corrected drift time spectrum (see Sec. ??)

$$r_{iso}(t) = \sum_{i=0}^4 P_i \times t^i. \quad (5.6)$$

Then, tracks are reconstructed as straight lines with a least squares fit (χ^2) to the isochrones calculated from the measured drift times using the defined $r_{iso}(t)$ -relation. Fig. 5.17 shows for all reconstructed tracks the distances to the fired straw wires versus the measured drift times. A systematic deviation in the track distance for single straws or straw groups from the expected $r_{iso}(t)$ -relation is corrected by adjusting the straw position accordingly. Here, the assembly technique of the STT simplifies the position calibration to a large extent. Individual deviations of single tubes in the close-packed double-layers are not possible and only the vertical position of the 13 double-layers have to be adjusted. The track reconstruction is repeated using the new straw layer positions, the distances are checked and the positions are corrected again until the systematic deviations vanish. Finally, also the $r_{iso}(t)$ -relation is verified by a new parameter fit of the reconstructed track to wire distances to the measured drift times.

The distribution of the finally obtained residuals

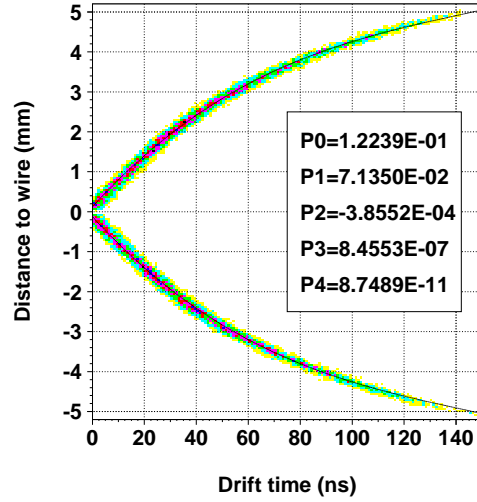
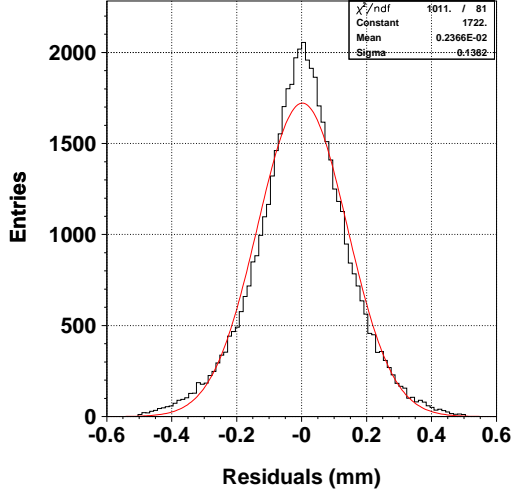


Figure 5.17: Track to wire distances and measured drift times for the reconstructed tracks. The $r_{iso}(t)$ -relation (black line) is parametrized as a polynomial function of 4th order with the parameters P_0 – P_4 .

of the reconstructed tracks to the isochrones is a measure of the spatial resolution of the STT and is shown in Fig. 5.18. Only a simple filter for single hits from delta-electrons with large distortions to the fitted track has been applied. No drift time correction due to the signal propagation time along the wire and the particle time-of-flight have been made. The estimated drift time error is about $\Delta t = 2$ ns. Also the reconstruction of a straight line track does not take into account multiple-scattering inside the STT which contributes to a maximum of about $100 \mu\text{m}$ for the first and last layers. The spatial resolution of the STT is given by the width of the residual distribution, which is $138 \mu\text{m}$ (σ) for the gas mixture of Ar/CO₂ (80/20%) at an absolute pressure of 1.25 bar. The shape of the distribution is nicely symmetric with a low mean of $2 \mu\text{m}$, showing no distortion by additional systematic errors.

The variation of the spatial resolution depending on the radial distance to the wire is shown in Fig. 5.19. Close to the wire the resolution is about $190 \mu\text{m}$, dominated by the primary ionization cluster spacing and time jitter together with higher drift velocities. Both effects are reduced more and more for larger distances to the wire and the resolution improves to about $100 \mu\text{m}$ close to the straw cathode, where the electron diffusion during their drift to the anode is the limiting factor.

The results obtained from the COSY-STT can be extrapolated to the \bar{P} ANDA-STT. Both detectors have a similar material budget and number of straw



is expected to be better than $140 \mu\text{m}$.

Figure 5.18: Distribution of the residuals of all reconstructed tracks as a measure of the COSY-STT spatial resolution. The width of $138 \mu\text{m}$ (σ) and mean of $2 \mu\text{m}$ are the results from the gaussian fit (red line).

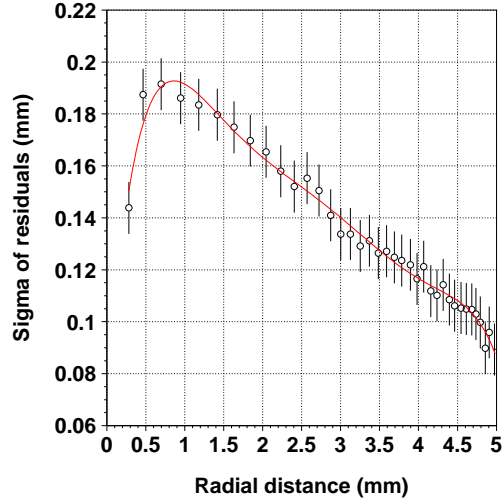


Figure 5.19: Width (sigma) of the residual distributions for different intervals of the radial distances to the wire.

layers for the tracking. The main differences are the operation of the $\bar{\text{PANDA}}$ -STT inside a solenoid field and at a higher straw gas pressure of about 2 bar. The additional Lorentz force will change the radial drift path for the electrons inside a straw to a longer, spiral drift path and increased drift times. Still the isochrones have a cylindrical shape, only the $r_{iso}(t)$ -relation will be different. The higher gas pressure will increase the maximum drift times and the ionization density which improves the spatial resolution. Therefore, assuming a comparable resolution of the drift time measurement of about $\Delta t = 2 \text{ ns}$ the spatial resolution of the $\bar{\text{PANDA}}$ -STT

5.3 Ferrara prototype modules

5.4 Krakow prototype module

5.4.1 Construction

Photographs taken after glueing the first layer of 16 straws of straw module and after glueing the second layer is shown in Fig. 5.20.

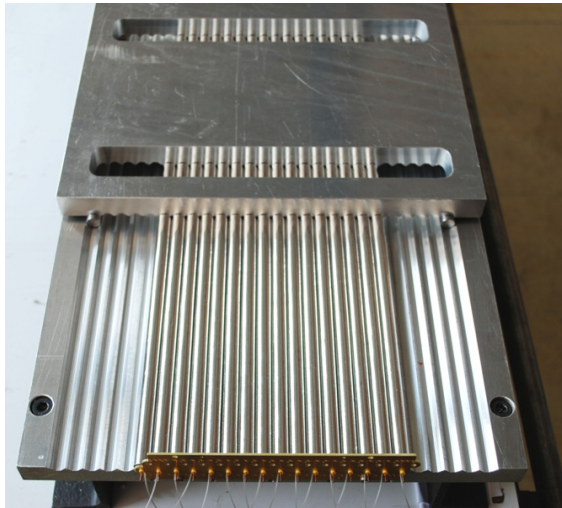


Figure 5.20: Glueing the first layer (top) and the second layer (bottom) of straw module.

The prototype module fixed to the transfer frame is shown in Fig. 5.21.

The prototype module fixed to the transfer frame is shown in Fig. 5.22.

5.4.2 Tests with radioactive sources

High voltage characteristics with ^{55}Fe X-ray source is show in Fig. 5.23.

High voltage characteristics with ^{60}Co β source is show in Fig. 5.24.

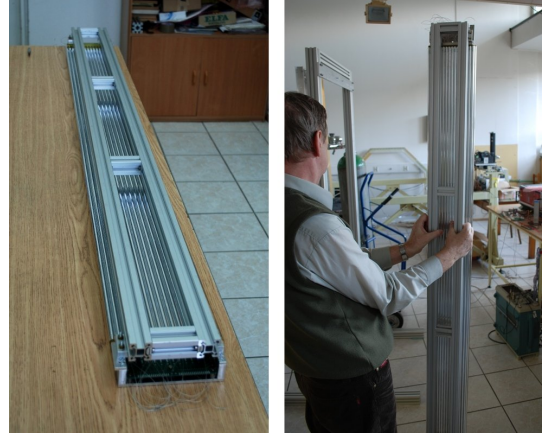


Figure 5.21: Prototype module mounted on the transfer frame (left) and the way of transferring (right).

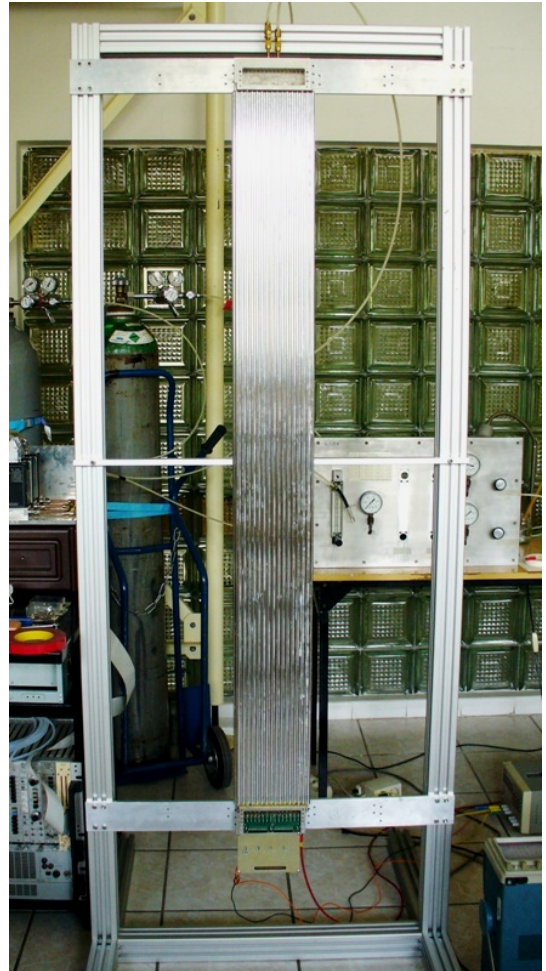


Figure 5.22: Prototype module mounted on support frame.

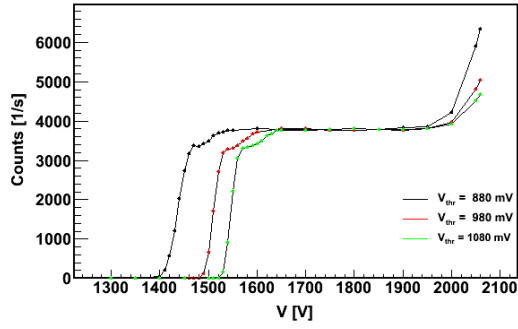


Figure 5.23: High voltage characteristics with ^{55}Fe X-ray source.

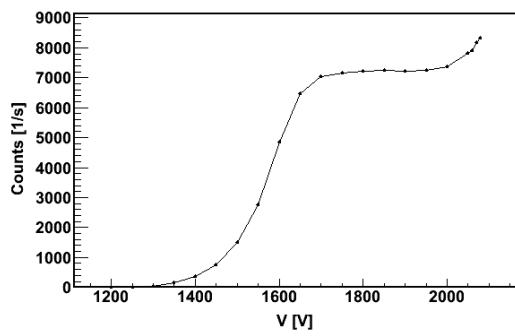


Figure 5.24: High voltage characteristics with ^{60}Co β source.

5.5 Summary and conclusions

6 Computer simulations and expected performance

6.1 The single straw tube simulation

6.1.1 The charge released into the tube

We have performed a detailed simulation of the charge generation and collection in a single straw tube.

In correspondence of an incident charged particle, we sample from the exponential distribution the point where an electron cluster is generated and from the proper distribution (see below) the number of electrons in the cluster. By stopping when the particle leaves the tube, we have the number of free electrons generated from a poissonian number of clusters. The mean number of clusters/cm is taken from ref. [?] (25 for *Ar* and 35.5 for *CO*₂). For the reliability of the simulation, it is crucial to know the cluster size distribution, that is the number of electrons per cluster. We use the theoretical calculations of [?] for *Ar* and the experimental data on *Ar* and *CO*₂ from [?]. The comparison with some available results in gas has shown that this choice is in reasonable agreement with data (see Fig. 6.1). By knowing the mean value of the en-

absorbers [?, ?]. The results, reported in Fig. 6.3, show good agreement with our simulation.

6.1.2 The drift process from GARFIELD

The tube response has been studied in detail giving as input to the GARFIELD code the tube size, wire radius, high-voltage, gas mixture and magnetic field.

The mixture and the high voltage determine the kind of behaviour of a gas. In the weak electric field or in a mixture with high quenching the electrons are in thermal equilibrium with the surrounding medium and the drift velocity is proportional to the electric field intensity. Such gases are usually called “cold”.

On the contrary, if the electron average kinetic energy differs from the thermal energy, the drift velocity behaviour becomes saturated and tends to be constant and independent of the electric field strength, that is of the distance from the wire anode. In this way the main sources of systematic errors are removed and the track reconstruction is easier. Such gases are called “hot”. However, the high spatial resolution in the hot gas mixtures is limited by the large diffusion, and cannot be better than 50 μm .

The drift velocity as a function of the wire distance is reported in Fig. 6.4 showing that the increase of the *CO*₂ percentage tends to cool the gas, with a corresponding stronger dependence of the velocity from the wire distance. This effect could be recovered by an accurate self-calibration (see below), but makes the tube stability more critical, requiring a precision control of temperature and pressure.

The effect of the magnetic field transforms the small segment motion between two collisions of a moving charge into circular trajectories. With obvious notation, the electron Lorentz angle is [?]:

$$\tan \alpha = \tan \omega \tau = \frac{eB}{m_e} \tau$$

where τ is the average time between collisions and ω is the Larmor frequency of the electron. In cold gases the drift velocity tends to be linear with the electric field E and τ is almost constant, whereas

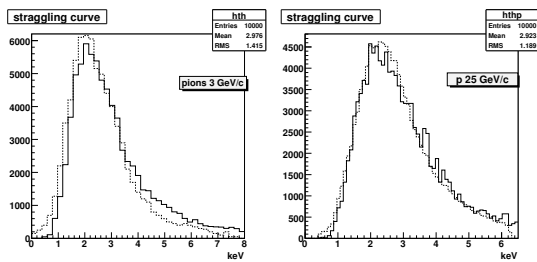


Figure 6.1: Comparison between the simulation of the energy lost in a 1.5 cm *Ar/CO*₂ layer (line) and the experimental values of Allison et al. [?] (dotted line).

ergy spent per free electron (i. e. to create a ion pair), the overall energy loss of the projectile on the whole path can be calculated. The assumed values are 27 eV for *Ar* and 33.5 eV for *CO*₂ [?].

As a further check, we compared the energy lost in the tube, for a variety of projectiles and energies, with the Urban model [?], which is used in GEANT3 and GEANT4 in the case of gaseous thin

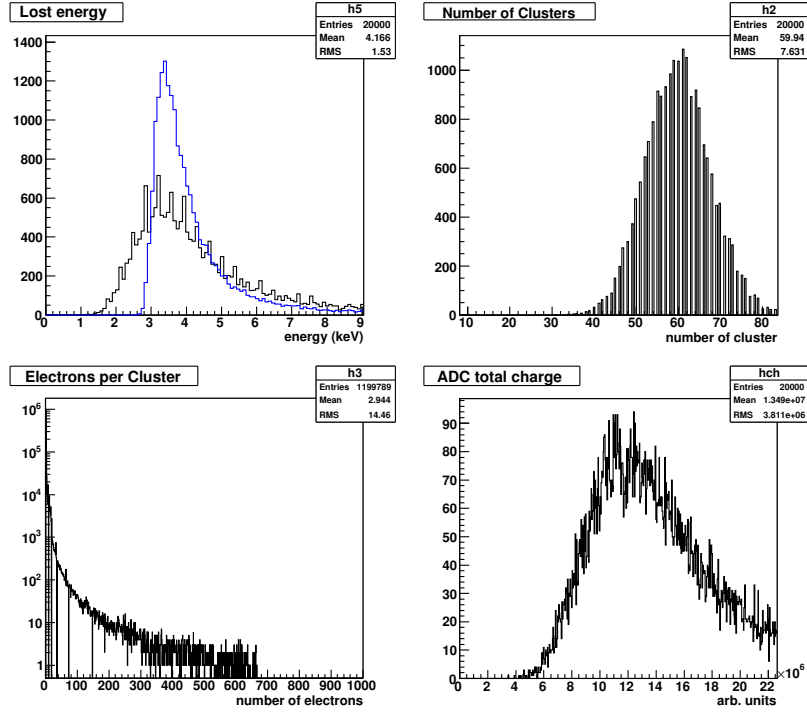


Figure 6.2: Results of the single tube simulation for a 1 GeV pion in a 2 atm pressure straw tube with a 90/10 Ar/CO_2 gas mixture. Upper left: energy lost in a tube compared with the sharper Landau distribution; upper right: poissonian distribution of the number of clusters; bottom left: cluster size distribution calculated as discussed in the text; bottom right: charge collected on the wire assuming a multiplication mechanism from the Polya distribution. By multiplying the number of clusters with the mean number of electrons per cluster, a mean number of primary electrons of about 200 is obtained.

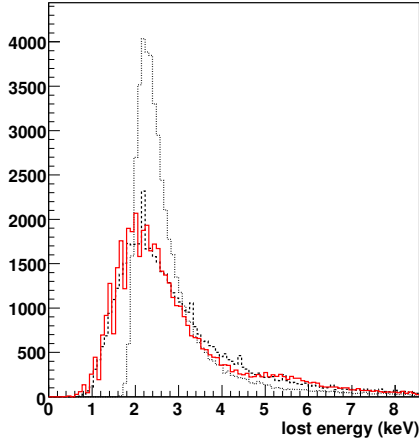


Figure 6.3: Energy loss of 1 GeV pion traversing a 1 cm of 90 % Ar 10 % CO_2 gas mixture at NTP. Solid line: Urban distribution; dashed line: specific simulation model; dotted line: Landau distribution.

in hot gases, where the drift velocity is more constant, τ is inversely proportional to E . Due to the much lower elastic cross section, τ in hot gases is about one order of magnitude higher. Estimation

from experimental data show that, for a 2T magnetic field and a 5 mm drift distance, the drift time for a CO_2/C_4H_{10} 90/10 mixture increase of 15 % in a magnetic field, that for a Ar/CO_2 90/10 mixture increases up to 50 % [?].

All these effects are reproduced in the GARFIELD results.

Typical time vs distance curves for a hot gas mixture like Ar/CO_2 90/10, with and without magnetic field, are reported in Fig. 6.5, where the increase of the drift time due to the field is clearly visible.

The increase in the drift time while increasing the CO_2 percentage is also clearly shown in Fig. 6.6.

Another important input to the simulation are the transverse and longitudinal diffusion curves, due to the thermal spreading of the electron clouds during the drift. The GARFIELD results show that the high diffusion values of the hot gas ($Ar/CO_2 = 90/10$) are partially compensated by increasing the pressure. At 2 atm pressure the longitudinal and transverse diffusion coefficients, at 5 mm distance from the wire, are 100 and 140 μm , whereas at 1 atm pressure the same coefficients are 120 and 220

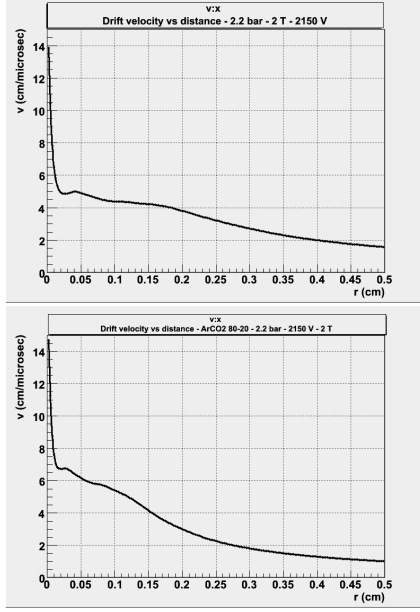


Figure 6.4: Drift velocity vs wire distance in a straw tube of 0.5 cm radius, 1850 V voltage, 2.2 bar pressure and 2 T magnetic field for different gas mixtures: (top) 90 – 10 % Ar – CO₂, (bottom) 80 – 20 % Ar – CO₂.

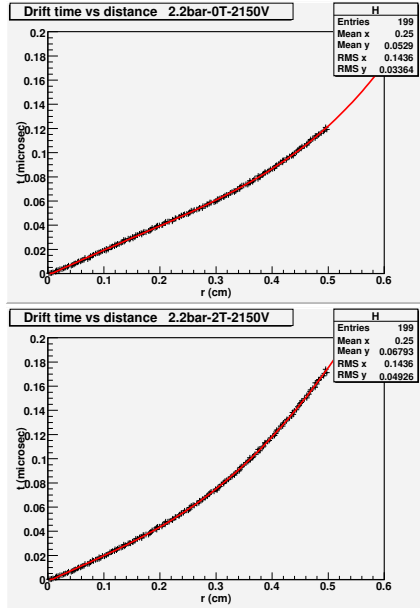


Figure 6.5: Drift time vs wire distance in a 90 – 10 % Ar – CO₂ straw tube of 0.5 cm radius and 2.2 bar pressure: up, without magnetic field; down, with magnetic field of 2 T (from GARFIELD).

μm , respectively.

Finally, the necessary input to the simulation is the gas amplification, that is the multiplication factor of the avalanche which is formed in the last tens of microns of the primary electron path in its drift to

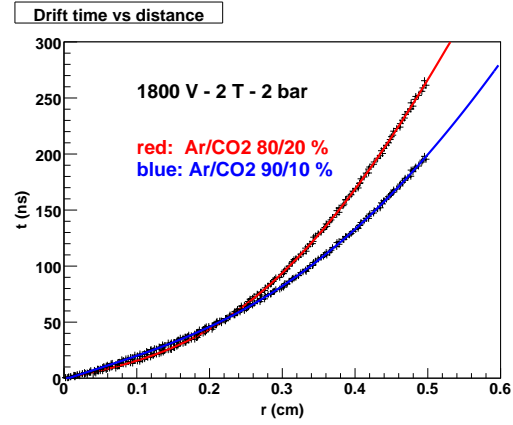


Figure 6.6: Time vs wire distance for two different Ar/CO₂ mixtures in the presence of magnetic field (from GARFIELD).

the anode wire. This multiplication factor is given by [?]:

$$G = \exp \left(\int_a^x \alpha(x) dx \right),$$

where $\alpha(x)$ is the Townsend coefficient (inverse of the mean free path for ionization), a is the anode wire radius and the integral is taken along the whole drift path. A typical behaviour of the gas gain, measured for our mixtures of interest is shown in Fig. 6.7, where one sees that in our case the tube remains in the region of direct proportionality.

6.1.3 Simulation of the drift process

Once the free electrons have been created in some points of the tube, their position is dispersed both longitudinally and transversally according to the GARFIELD diffusion curves and the time of arrival on the wire is calculated from the GARFIELD distance-time curves.

The arrival of each electron gives rise to a charge, which is obtained by sampling from a Polya distribution [?] having as a mean value the gain or multiplication factor (around $5 \cdot 10^4$). Then, by summing this signal over the number of electrons we obtain the total charge, as shown in Fig. 6.2.

6.1.4 The electrical signal

By taking into account the arrival time of each electron and assigning a Gaussian-shaped electrical response to each charge multiplication, we can reproduce also the shape of the electrical signal. We added also a white noise component equal to the 3% of the primary signal peak value.

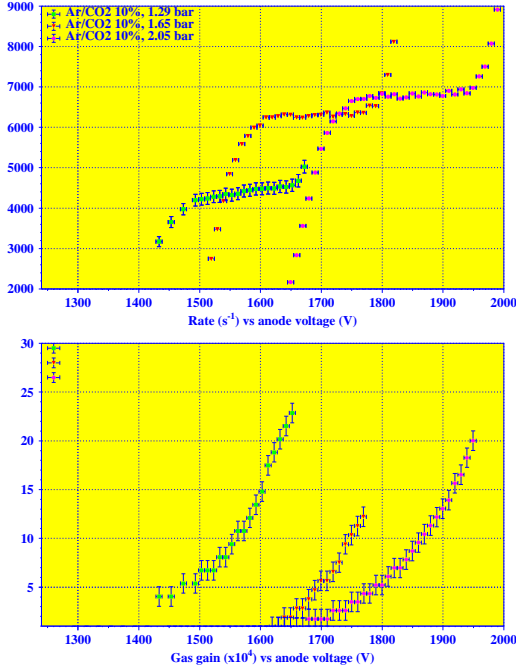


Figure 6.7: Experimental plots of the tube rate and gas gain relative to a 90 – 10 % $Ar - CO_2$ mixture.

Some examples are shown in Fig. 6.8, where two typical signals are shown: the first one is generated from a track 1 mm near to the wire, the second one from a track 4 mm far from the wire. In the first case the clusters arrive dispersed in time, giving rise to an irregular structure of the signal. In this case the discrimination technique is crucial for a good time resolution. In the second case the cluster arrival is more concentrated and the signal structure appears more regular. These example show the importance of the electronic treatment of the signal and of the discrimination technique to be used for obtaining the drift time.

We consider two discrimination techniques: fixed (F) and constant fraction (CF) thresholds. The F threshold is set to about 5 % of the mean primary electron value, that is to 10 primary electrons in the 2 atm case (see Fig. 6.2). This is compatible with previous studies [?, ?]. The CF threshold is set to 5 % of the peak value of the current signal.

In the following, when no explicitly specified, the displayed results are obtained with the standard F threshold.

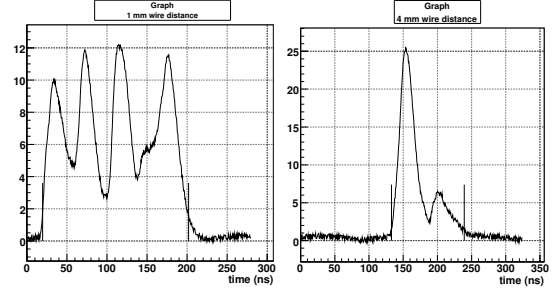


Figure 6.8: Straw tube signal simulated from a track near to (left) and far from (right) the wire.

6.1.5 Simulation of the self-calibration procedure

The primary information from the tube is the drift time distribution of the arriving signals, that is the number of tracks dN within the time interval dt . A typical distribution of this quantity, in the case of a parallel and uniform illumination of the tube is shown in Fig. 6.9 and in Fig. 6.10 (left) in the case of the absence and the presence of the magnetic field, respectively.

The self-calibration method exploits the properties of this distribution. Since the track density is constant over the tube diameter, one can write

$$\frac{dN}{dr} = \frac{N_{\text{tot}}}{R}, \quad (6.1)$$

where N is the number of tracks, r is the wire distance, N_{tot} is the total number of tracks and R the tube radius. The number of tracks in a time interval can be obtained directly from the above relation:

$$\frac{dN}{dt} = \frac{dN}{dr} \frac{dr}{dt} = \frac{dr}{dt} \frac{N_{\text{tot}}}{R}. \quad (6.2)$$

After integration, one obtains the desired space-time relation $r(t)$ by integration of the time spectrum up to t :

$$r(t) = \frac{R}{N_{\text{tot}}} \int_0^t \frac{dN}{dt} dt. \quad (6.3)$$

The time spectrum and the space time relation $r(t)$ are shown in Fig. 6.9 (without magnetic field) and in Fig. 6.10 (with magnetic field). The result of this method of calibration is shown in Fig. 6.11.

This simulated procedure corresponds, during the real calibration, to have an accurate knowledge of the relationship between the measured drift time and the minimum approach distance of the particle trajectory to the wire. The mean value of the residuals of tracks is then used to correct the measured drift times until the residual distribution is symmetric about zero.

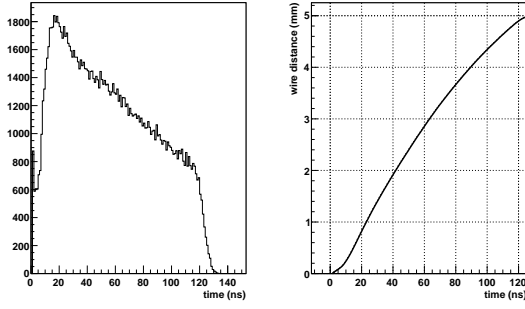


Figure 6.9: Simulated TDC spectrum without magnetic field of a single tube uniformly illuminated (left) and space-time relation obtained with the self-calibration method of Eq. 6.3.

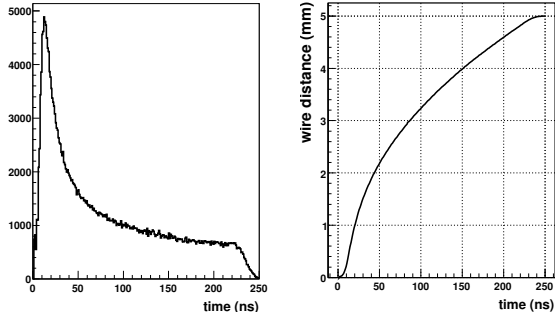


Figure 6.10: Simulated TDC spectrum for a 2T magnetic field of a single tube uniformly illuminated (left) and space-time relation obtained with the self-calibration method of Eq. 6.3.

To explore the effect of the electronic threshold, we simulate also the resolution obtained by applying to the signal a constant fraction discrimination technique, simulated as a fixed percentage (5 %) of the peak of the current signal.

The improvement in the resolution, showed in Fig. 6.12, demonstrates the importance of the discrimination of the tube signals.

6.1.6 Full and fast simulation

The full simulation reproduces the time output from the drift tube and the ADC response on the charge collected starting from the primary cluster formation as discussed in the sections above. Since the time required for each event is long, we also implemented into the simulation software a fast simulation option.

The spatial resolution is simply obtained through the MC truth for the true wire distance, which is used as the abscissa in Fig. 6.13 to extract the σ for the Gaussian smearing to obtain a realistic position

determination of the tube.

The second important quantity, the charge collected on the wire, is simulated in a fast manner by sampling the energy lost from the Urban distribution as in Fig. 6.3, avoiding in this case the charged cluster generation.

In this way the time spent in the tube response simulation result to be negligible when compared with the other part of the software.

6.1.7 Performance in magnetic field

Drift of electrons in the drift detectors can be considerably influenced by magnetic field components perpendicular the electric field. The trajectories of the electrons have in this case a form of spirales and the drift time is longer compared to the case of absence of the magnetic field. For a precise reconstruction of the particle trajectories on the basis of the measured drift time, corrections to the distance-drift time relation - $r(t)$ might be needed if the effect of the drift time elongation due to the magnetic field is comparable or larger than the drift time resolution. In order to estimate this effect we performed simulations of the drift of electrons in the straw tubes using the GARFIELD code. The simulations were performed for straw tubes oriented vertically (y -direction) and particle tracks going in the z -direction. Results of these simulations are shown in Fig. ?? in a form of distance-drift time relation - $r(t)$ calculated for various values of magnetic field components in the range from 0 to 1 T. The largest variations in the $r(t)$ relation is caused by the vertical magnetic field B_y . For distances from the sense wire close to the straw radius (5 mm) setting on 1 T field prolongs the drift time from about 130 ns to about 140 ns. The corresponding drift path $\Delta r = dr/dt \Delta t$ equals to about 0.5 mm. Much smaller effect is caused by the horizontal field component B_x .

The information about the magnetic field at the position of individual straws in the tracking stations we derived from 3-dimensional field maps calculated for the PANDA solenoid and dipole magnet. As an example, Fig. ?? shows the magnetic field distribution in the $y = 0$ plane with indicated active volumes of the tracking stations.

The tracking stations DC1, DC2 and DC5, DC6 stay in stray magnetic field of the solenoid and the dipole magnet. In the active volumes of these stations the x -, y - and z -components of the magnetic field are smaller than 0.35 T and the resulting corrections to the $r - t$ relation lie below 0.05 mm and

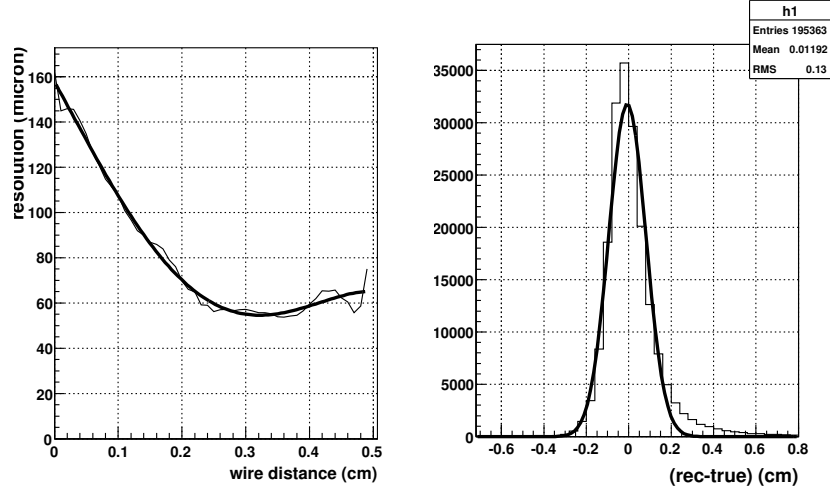


Figure 6.11: Simulated average residual width as a function of the track distance from the wire (left) and residual distribution of (reconstructed-true) wire distance. The bold line is the smoothing polynomial.

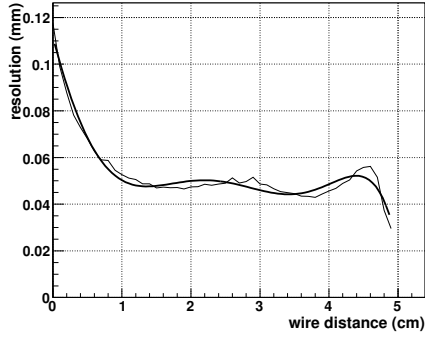


Figure 6.12: As in Fig. 6.11 with a constant fraction electronic discrimination.

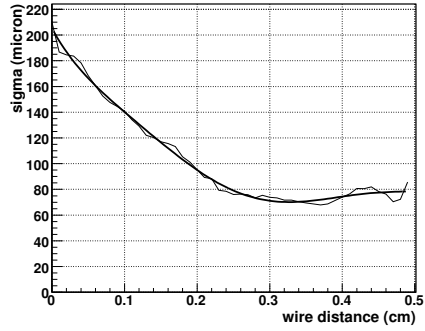


Figure 6.13: Standard deviation corresponding to the residual width resolution of Fig. 6.11 (left).

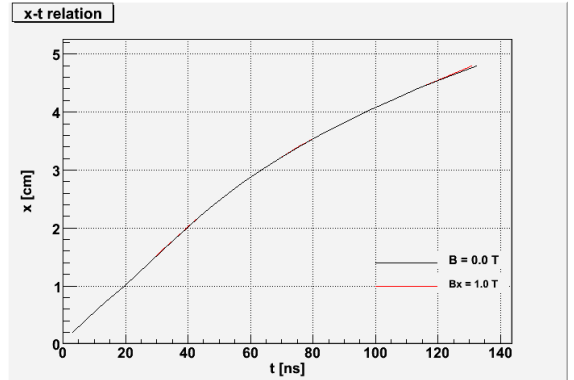
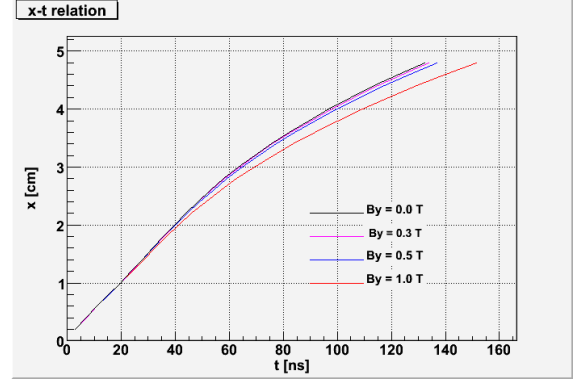


Figure 6.14: x-t relation for magnetic field in y-direction (top) and x-direction (bottom).

and can be neglected in view of the expected position resolution of about $\sigma = 0.1$ mm. For the two tracking stations DC3 and DC4 inside the dipole magnet gap, for the maximum setting of the magnet field corresponding to the field integral of 2 Tm the corrections to the $r - t$ relation are up to 0.35 mm. These corrections will be tabulated for each straw

layer on a grid of x - and y - coordinates and will be applied during the track reconstruction.

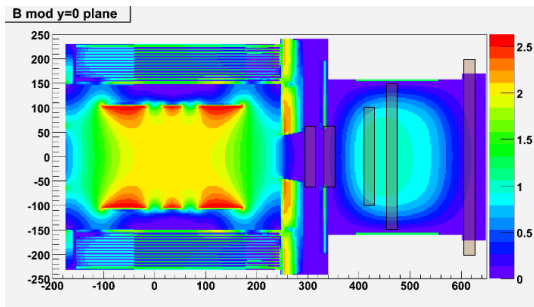


Figure 6.15: Magnetic field distribution in the Target Spectrometer and in the Forward Spectrometer in the horizontal symmetry plane $y = 0$ for the maximum setting of the field in the magnets.

6.2 Simulation and reconstruction software

6.3 Track and momentum reconstruction

6.4 Optimization of the tracking system

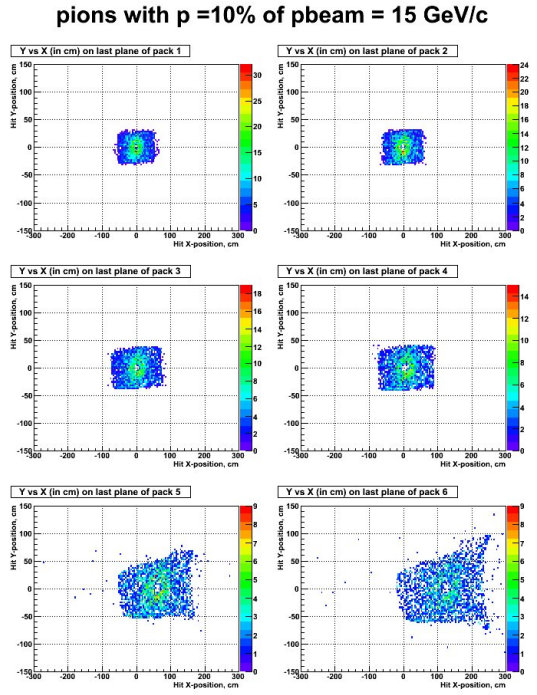


Figure 6.16: Deformation of the DC6 support frame under its own weight.

6.5 Physics channels analysis

Intensity distribution of 1.5 GeV/c pions at the positions of the tracking stations is shown in Fig. 6.16.

7 Organization

7.1 Production logistics

7.1.1 Production of straws

7.1.2 Assembly of straw tube modules and detection layers

7.1.3 Quality control

7.2 Work-packages

7.3 Timelines

8 Appendices

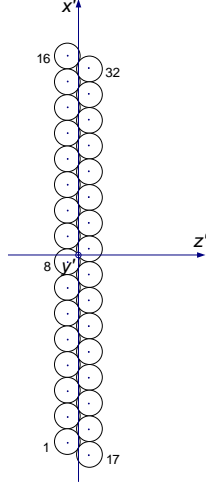


Figure 1: Arrangement of straws in one module. The origin of local righthanded coordinate system (x', y', z') is located in the symmetry plane perpendicular to the straws.

stations calculated in the reference frame associated with the PANDA target are given in Table 1.

Table 1 contains also dimensions of active area defined in Fig. ?? for individual double-layers.

.1 Description of geometry of tracking stations

The detection planes are built of separate modules, each containing 32 straws arranged in two layers as shown in Fig. 1.

The sense wires in neighboring straws are spaced by 10.1 mm which is equal to the straw diameter at the planned gas overpressure of 1 bar. In a local reference system (x', y', z') associated with a single module (see Fig. 1), the sense wires in the first and in the second straw layer are located at $z' = -4.373$ [mm] and $z' = +4.373$ [mm], respectively. In the x' direction the layers are staggered by a distance equal to the straw radius (5.05 mm) in order to resolve the "left-right ambiguity" of track position with respect to the sense wire. The x' coordinates of the sense wires in the first and in the second straw layer are given respectively by the two following equations:

$$\begin{aligned} x'_i &= -73.225 + 10.1(i - 1) \text{ [mm]}, \quad (i = 1..16), \\ x'_i &= -78.275 + 10.1(i - 17) \text{ [mm]}, \quad (i = 17..32). \end{aligned}$$

The the inclination and positions of individual modules from consecutive double layers of the tracking

Table 1: Inclination, coordinates and length of straw modules from individual double layers of the tracking stations. The coordinates x , y , z describe position of centers of modules (defined in Fig. ??) in right-handed coordinate system with the origine located in the nominal beam-target crossing point, the y -axis oriented in the vertical direction and the z -axis pointing along the beam direction.

FT	Double layer	Wire incl. θ	z pos. [mm]	N mod.	x position of i 'th module ($i = 1..N$) [mm]	Act. area		Straw length [mm]
						w [mm]	h [mm]	
1	1	0°	2954	8	$-565.600 + (i - 1)161.6$	1297.9	640.0	640.0
	2	$+5^\circ$	3004	8	$-567.760 + (i - 1)162.217$	1358.8	640.0	657.0
	3	-5°	3054	8	$-567.760 + (i - 1)162.217$	1358.8	640.0	657.0
	4	0°	3104	8	$-565.600 + (i - 1)161.6$	1297.9	640.0	640.0
2	1	0°	3274	8	$-565.600 + (i - 1)161.6$	1297.9	640.0	640.0
	2	$+5^\circ$	3324	8	$-567.760 + (i - 1)162.217$	1358.8	640.0	657.0
	3	-5°	3374	8	$-567.760 + (i - 1)162.217$	1358.8	640.0	657.0
	4	0°	3424	8	$-565.600 + (i - 1)161.6$	1297.9	640.0	640.0
3	1	0°	3945	12	$-888.800 + (i - 1)161.6$	1944.3	690.3	690.3
	2	$+5^\circ$	4025	12	$-892.195 + (i - 1)162.217$	2013.3	704.3	721.6
	3	-5°	4165	12	$-892.195 + (i - 1)162.217$	2015.4	728.8	746.2
	4	0°	4245	12	$-888.800 + (i - 1)161.6$	1944.3	690.3	690.3
4	1	0°	4385	12	$-888.800 + (i - 1)161.6$	1944.3	767.3	767.3
	2	$+5^\circ$	4465	12	$-892.195 + (i - 1)162.217$	2020.0	781.3	798.9
	3	-5°	4605	12	$-892.195 + (i - 1)162.217$	2022.2	805.8	823.5
	4	0°	4685	12	$-888.800 + (i - 1)161.6$	1944.3	819.8	819.8
5	1	0°	6075	25	$-1939.200 + (i - 1)161.6$	4045.1	1180.0	1180.0
	2	$+5^\circ$	6125	25	$-1946.607 + (i - 1)162.217$	4163.7	1180.0	1199.1
	3	-5°	6175	25	$-1946.607 + (i - 1)162.217$	4163.7	1180.0	1199.1
	4	0°	6225	25	$-1939.200 + (i - 1)161.6$	4045.1	1180.0	1180.0
6	1	0°	7475	37	$-2908.800 + (i - 1)161.6$	5984.3	1480.0	1480.0
	2	$+5^\circ$	7525	37	$-2919.911 + (i - 1)162.217$	6136.6	1480.0	1500.2
	3	-5°	7575	37	$-2919.911 + (i - 1)162.217$	6136.6	1480.0	1500.2
	4	0°	7625	37	$-2908.800 + (i - 1)161.6$	5984.3	1480.0	1480.0

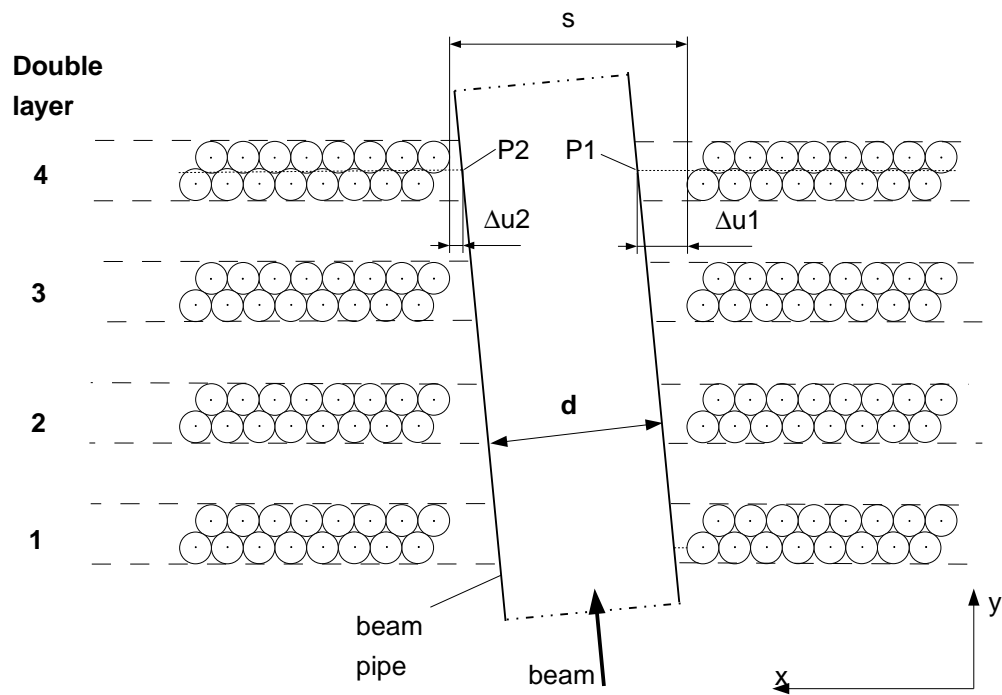


Figure 2: Opening for the beam pipe in tracking station.

Tracking station	Double layer	Beam pipe		Opening				
		$x(P1)$ [mm]	$x(P2)$ [mm]	module(straws)	s [mm]	t [mm]	Δu_1 [mm]	Δu_2 [mm]
1	1	-51	51	4(11-16,27-32), 5(1-6,17-22)	116.15	172	7	7
	2	-51	51	4(11-16,27-32), 5(1-6,17-22)	116.15	172	7	7
	3	-51	51	4(11-16,27-32), 5(1-6,17-22)	116.15	172	7	7
	4	-51	51	4(11-16,27-32), 5(1-6,17-22)	116.15	172	7	7
2	1	-51	51	4(11-16,27-32), 5(1-6,17-22)	116.15	172	7	7
	2	-51	51	4(11-16,27-32), 5(1-6,17-22)	116.15	172	7	7
	3	-51	51	4(11-16,27-32), 5(1-6,17-22)	116.15	172	7	7
	4	-51	51	4(11-16,27-32), 5(1-6,17-22)	116.15	172	7	7
3	1	-47	49	6(11-16,27-32), 7(1-6,17-22)	116.15	166	9	9
	2	-46	50	6(11-16,27-32), 7(1-6,17-22)	116.15	166	10	8
	3	-45	51	6(11-16,27-32), 7(1-6,17-22)	116.15	166	11	7
	4	-44	52	6(11-16,27-32), 7(1-6,17-22)	116.15	166	12	6
4	1	-43	53	6(11-16,28-32), 7(1-6,17-23)	116.15	166	8	10
	2	-42	54	6(11-16,28-32), 7(1-6,17-23)	116.15	166	9	9
	3	-40	56	6(11-16,28-32), 7(1-6,17-23)	116.15	166	11	7
	4	-38	58	6(11-16,28-32), 7(1-6,17-23)	116.15	166	13	5
5	1	-	-	13(5-16,21-32), 14(1-6,17-22)	181.8	238	9	10
	2	-	-	13(5-16,21-32), 14(1-6,17-22)	181.8	238	11	8
	3	-	-	13(5-16,21-32), 14(1-6,17-22)	181.8	238	13	6
	4	-27	141	13(5-16,21-32), 14(1-6,17-22)	181.8	238	15	4
6	1	23	191	19(10-16,27-32), 20(1-12,17-29)	181.8	238	5	14
	2	25	193	19(10-16,27-32), 20(1-12,17-29)	181.8	238	7	12
	3	27	195	19(10-16,27-32), 20(1-12,17-29)	181.8	238	9	10
	4	29	197	19(10-16,27-32), 20(1-12,17-29)	181.8	238	11	8

Table 2: Dimensions of rectangular openings in the tracking stations for the beam pipe.

References

Acknowledgments

thanks....

ADC Analog to Digital Converter	ENC Equivalent Noise Charge
AGATA Advanced Gamma Tracking Array	Eoc End-of-Column
AGS Alternate Gradient Synchrotron	EPR Electron Paramagnetic Resonance
APD Avalanche Photo Diode	EU European Union
API Application Programming Interface	FADC Flash ADC
AS Advanced Switching	FAIR Facility for Antiproton and Ion Research
ASIC Application Specific Integrated Circuit	FE Front-End
BGO Bismuth Germanate	FEE Front-End Electronics
BNL Brookhaven National Laboratory	FET Field-Effect Transistor
BTCP Bogoroditsk Techno-Chemical Plant	FNAL Fermi National Laboratory
CA Certification Authority	FPGA Field Programmable Gate Array
CAD Computer Aided Design	FS Forward Spectrometer
CCE Charge Collection Efficiency	FZJ Forschungszentrum Jülich
CDR Conceptual Design Report	GEM Gas Electron Multiplier
CERN Conseil European pour la Recherche Nu- cleaire	GPD Generalized Parton Distribution
CLAS Cebaf Large Acceptance Spectrometer	GSI Gesellschaft für Schwerionenforschung
CKM Cabbibo-Kobayashi-Maskawa	GSS Generic Security Service, an authentication API aka Kerberos V5
CLAS CEBAF Large Acceptance Spectrometer	HC Hadron Calorimeter
COMPASS Common Muon Proton Apparatus for Structure and Spectroscopy	HESR High Energy Storage Ring
COSY Cooler Synchrotron	HFG Hermann von Helmholtz-Gemeinschaft Deutscher Forschungszentren
CT Central Tracker	HTS High Temperature Superconductors
CVS Code Versioning System	HV High Voltage
DAQ Data Acquisition	IBP In-Beam Polarimeter
DESY Deutsches Elektronensynchrotron	IP Interaction point
DIRC Detector for Internally Reflected Cherenkov Light	IHEP Institute for High Energy Physics
DLL Delay Lock Loop	INFN Istituto Nazionale di Fisica Nucleare
DPM Dual Parton Model	KVI Kernfysisch Versneller Instituut
DSP Digital Signal Processor	LAAPD Large Area APD
DVCS Deeply Virtual Compton Scattering	LEAR Low Energy Antiproton Ring
EGEE Enabling Grids for E-science in Europe	LEC Liquid Encapsulated Czochalski
ELT Enclosed Layout Transistors	LED Light Emission Diode
EMC Electromagnetic Calorimeter	LEGS Laser Electron Gamma Source
	LHC Large Hadron Collider

LNP Low Noise Preamplifier	SSL Secure Socket Layer
LOI Letter of Intent	STT Straw Tube Tracker
LP Low-Pass	TCS Trigger Control System
LQCD Lattice QCD	TDC Time to Digital Converter
MAPS Monolithic Active Pixel Sensor	TDS Time Distribution System
MDC Mini Drift Chamber	TJNAF Thomas Jefferson National Accelerator Facility
MIP Minimum Ionizing Particle	TOF Time-of-Flight Detector
MIRAC Mid Rapidity Calorimeter	TOP Time-of-Propagation
MUD Muon Detector	ToT Time-over-Threshold
MVD Micro Vertex Detector	TPC Time Projection Chamber
NIEL Non-Ionizing Energy Loss	TRD Transition Radiation Detector
NMR Nuclear Magnetic Resonance	TS Target Spectrometer
PCB Printed Circuit Board	TSL Thermostimulated luminescence
PCI Peripheral Component Interconnect	TSL The Svedberg Laboratory
PDR Preliminary Design Report	TTC Time Trigger and Control
PED Particle Energy Deposit	UrQMD Ultra-relativistic Quantum Molecular Dynamic
PID Particle Identification	VEGA Versatile and Efficient Gamma Detector
PLL Phase Lock Loop	VME Versa Module Eurocard
PMT Photomultiplier	WLS Wave Length Shift(er/ing)
PSI Paul Scherrer Institute	
PTS Pellet Test Station	
PWO Lead Tungstate	
QA Quality Assurance	
QCD Quantum Chromo Dynamics	
QED Quantum Electrodynamics	
RICH Ring Imaging Cherenkov Counter	
RPC Resistive Plate Chambers	
SASL Simple Authentication and Security Layer	
SCT Semiconductor Tracker	
SI Semi-insulating	
SICCAS Shanghai Institute of Ceramics, Chinese Academy of Sciences	
SLAC Stanford Linear Accelerator Center	
SMD Surface Mount Device	

List of Figures

1.1	Overview of the future FAIR facility .	1	2.3	The spatial resolution for the Ar+10%CO ₂ gas mixture for 1 a) and 2 atm b) pressures. The red line corresponds to an ideal $r(t)$ relation, the black one to the measured. The main contributions to the resolution are also shown in different colors . .	28
1.2	Layout of the $\bar{\text{PANDA}}$ detector . . .	2	2.4	Spatial resolution in He+10% i-C ₄ H ₁₀ with 1 a) and 2 atm b). The red line corresponds to an ideal $r(t)$ relation, the black one to the measured. The main contributions to the resolution are also shown in different colors. The experimental spatial resolution of the KLOE drift chamber, denoted by the open circles, is given for comparison [?]	28
1.3	Layout of the High Energy Storage Ring HESR	4	2.5	The spatial resolution for the Ar+10%CO ₂ a) and the He+10%iC ₄ H ₁₀ b) gas mixtures at 1 atm pressures. The gas gain has been reduced by a factor two compared with Fig. 2.3 and Fig. 2.4. The red lines correspond an “ideal” $r(t)$ relation, while the black one corresponds to the measured one. Contributions from the main limiting process are shown by dashed lines. The spatial resolution of the KLOE drift chamber, denoted by the open circles, is given for comparison [?].	29
1.4	Optical functions of HESR lattice for $\gamma_{tr} = 6.2$	4	2.6	Space time relation (left) and diffusion (right) of two gas mixtures with different CO ₂ percentage, red points correspond to a percentage of 10%, blue to 30% one.	29
1.5	Summary of the different target options foreseen at $\bar{\text{PANDA}}$	6	2.7	Space time relation for the Ar+10%CO ₂ mixture at 1 atm for two different temperatures. . . .	29
1.6	Time dependent macroscopic luminosity profile $L(t)$ in one operation cycle	8	4.3	Block diagram of ASIC proposed for straw-tube read-out	38
1.7	Maximum average luminosity vs. atomic charge Z of the target for three different beam momenta	9	4.4	Examples of the simulated analog responses for different input charges. .	38
1.8	Basic detection concept	11	4.5	Examples of front-end pulses for not optimized (red) and optimized (blue) settings of the ion cancellation network.	38
1.9	Artistic side view of the Target Spectrometer (TS) of $\bar{\text{PANDA}}$	12			
1.10	The Micro Vertex Detector (MVD) of the Target Spectrometer	12			
1.11	Straw Tube Tracker (STT) of the Target Spectrometer	13			
1.12	Artistic side view of the Forward Spectrometer (FS) of $\bar{\text{PANDA}}$	16			
1.13	Double layer of straw tubes in the tracker of the Forward Spectrometer	16			
1.14	Overview of the $\bar{\text{PANDA}}$ tracking system.	19			
2.1	A straw consists of a mylar film tube which is closed by two end plugs, each containing a crimp pin to fix the anode wire in the center and a gas tube to provide a gas flow through the tube. The contact springs inserted in the small film overlap at both tube ends provide the electric cathode contact. The straw ends are fixed by a plastic ring to an attachment band which contains on the inner side the electric ground.	26			
2.2	Measured wire tension (weight equivalent) at different gas overpressure inside a straw. The nominal tension is 40 G at 1.2 bar overpressure for the COSY-STT straws.	26			

4.6	Examples of the front-end gain measurement for default settings with 'delta-like' current pulses.	38	5.4	Distribution of the residuals for r in the range [2.5, 3] mm at the last step of the autocalibration. The distribution has been fitted with two Gauss functions; the parameters of the fit are in the box (p_3 , p_4 and p_5 are the ones of the Gauss function that fits the peak).	49
4.7	Examples measurement of the front-end noise vs input capacitance. . . .	38	5.5	Distribution of the mean residuals after the sixth iteration of the autocalibration procedure. The parameters of the fit (red curve) are in the box: p_0 , p_1 and p_2 are referred to the fit of the distribution tails; p_3 , p_4 and p_5 are the parameters of the Gauss function that fits the peak.	49
4.8	Example measurement of the discriminator time walk.	39	5.6	Residuals vs. drift distance.	50
4.9	Time-over-threshold vs charge measured with "delta-like" current pulses.	39	5.7	Distribution of the residuals for r in the range [2.5, 3] mm after the sixth iteration of the autocalibration, in case the hit tube is taken out from the track reconstruction (it is the analogous of Fig. 5.4). The distribution has been fitted with two Gaussian; the parameters of the fit are in the box (p_0 , p_1 and p_2 are the ones of the Gaussian that fits the peak).	50
4.10	Time-over-threshold spectrum measured with an ^{55}Fe source and the straw tube at HV=1750 V.	39	5.8	Single tube spatial resolution σ as a function of the drift distance.	51
4.11	Example of the ASIC analog signal output measured at a high (few MHz) hit rate.	39	5.9	Examples of residual distributions for single tubes, which have been taken out from track reconstruction: (a) tube 3 in layer 0 and (b) tube 7 in layer 2. The distributions should be centered around 0 (dotted line).	52
4.12	Prototype board of a 32-channel preamplifier/discriminator based on CARIOCA-10 chips.	40	5.10	(a) Distribution of the mean deviations (with sign) of the wire positions from their nominal ones: this is a measure of the systematic shift of the wires. (b) Distribution of the absolute values of the deviations plotted in (a).	52
4.13	Scheme of TDC-FPGA implementation with carry chain usage.	40	5.11	Examples of beam intensity variation during the high rate test of the \bar{P} ANDA-STT prototype. Different colors give the distributions of beam intensity measured on different straws. Beam intensities greater than 1 MHz/straw were observed.	53
4.14	ADC-FPGA implementation [?].	41			
4.15	Example of the input and reference signal. The red points mark the transition point when the FPGA should see a change from the logical 0 (1) to the 1 (0) level.	41			
4.16	Block diagram of TRBv3.	42			
4.17	Produced TRBv3 board.	42			
4.18	Schematics of the TRBv2 HADES board used for the time-of-flight measurements.	43			
4.19	HADES TRBv2 board.	43			
4.20	Optical HUB board for the HADES experiment.	44			
5.1	Straw tube prototype used at the Institut für Kernphysik at Forschungszentrum-Jülich. Design and construction by IKP-Jülich.	48			
5.2	Detail of the prototype shown in Fig. 5.1.	48			
5.3	Mean spatial resolution σ for single tubes, obtained as explained in the text. The red line is the fit with a third order polynomial.	49			

- 5.12 Signals from straw tubes recorded in 5 μ s windows of 240 MHz flashADC at high beam intensities: (left-hand side, upper) 6 groups of signals are comprised within the window. The relevant beam intensity is equal to 1.2 MHz; (right-hand side, upper) the same for beam intensity of 2.2 MHz; (left-hand side, lower) example of the signal pileup. Colored region is blown up in the: (right-hand side, lower) blown up region of the neighboring figure presenting the pile-up of the signals. Remarkable is lack of any unfavorable effects like baseline shift or signal shape deterioration even at very high beam intensities. 54
- 5.13 Simulation of $\bar{p}p$ reactions and number of hits per event and per cm along the tubes in the innermost layer of the PANDA straw tube tracker. The target position is at $z=0$ cm. 54
- 5.14 Measured normalized gas gain reduction ($\Delta G/G_0$) along the tube for all 32 straws, shown in groups of 4 straws. Straw no. 1–4 (upper left) to straw no 29–32 (lower right). The beam hit all tubes around 0 cm longitudinal position. 56
- 5.15 The COSY-STT mounted at the front cap of the COSY-TOF spectrometer. The detector consists of 2704 straw tubes of 1 m length and 10 mm diameter, arranged as a vertical stack of 13 close-packed double-layers at three different orientations. 57
- 5.16 Gas leakage of the COSY-STT filled with pure argon (red) and pure CO_2 (blue), measured by the gas pressure drop of the straws in surrounding vacuum. 58
- 5.17 Track to wire distances and measured drift times for the reconstructed tracks. The $r_{iso}(t)$ -relation (black line) is parametrized as a polynomial function of 4th order with the parameters P_0 – P_4 58
- 5.18 Distribution of the residuals of all reconstructed tracks as a measure of the COSY-STT spatial resolution. The width of $138 \mu m$ (σ) and mean of $2 \mu m$ are the results from the gaussian fit (red line). 59
- 5.19 Width (sigma) of the residual distributions for different intervals of the radial distances to the wire. 59
- 6.1 Comparison between the simulation of the energy lost in a 1.5 cm Ar/CO_2 layer (line) and the experimental values of Allison et al. [?] (dotted line). 64
- 6.2 Results of the single tube simulation for a 1 GeV pion in a 2 atm pressure straw tube with a 90/10 Ar/CO_2 gas mixture. Upper left: energy lost in a tube compared with the sharper Landau distribution; upper right: poissonian distribution of the number of clusters; bottom left: cluster size distribution calculated as discussed in the text; bottom right: charge collected on the wire assuming a multiplication mechanism from the Polya distribution. By multiplying the number of clusters with the mean number of electrons per cluster, a mean number of primary electrons of about 200 is obtained. . . . 65
- 6.3 Energy loss of 1 GeV pion traversing a 1 cm of 90 % Ar 10 % CO_2 gas mixture at NTP. Solid line: Urban distribution; dashed line: specific simulation model; dotted line: Landau distribution. 65
- 6.4 Drift velocity vs wire distance in a straw tube of 0.5 cm radius, 1850 V voltage, 2.2 bar pressure and 2 T magnetic field for different gas mixtures: (top) 90–10 % $Ar-CO_2$, (bottom) 80–20 % $Ar-CO_2$ 66
- 6.5 Drift time vs wire distance in a 90–10 % $Ar-CO_2$ straw tube of 0.5 cm radius and 2.2 bar pressure: up, without magnetic field; down, with magnetic field of 2 T (from GARFIELD). 66
- 6.6 Time vs wire distance for two different Ar/CO_2 mixtures in the presence of magnetic field (from GARFIELD). 66

6.7	Experimental plots of the tube rate and gas gain relative to a 90 – 10 % $Ar - CO_2$ mixture.	67
6.8	Straw tube signal simulated from a track near to (left) and far from (right) the wire.	67
6.9	Simulated TDC spectrum without magnetic field of a single tube uniformly illuminated (left) and space-time relation obtained with the self-calibration method of Eq. 6.3.	68
6.10	Simulated TDC spectrum for a 2T magnetic field of a single tube uniformly illuminated (left) and space-time relation obtained with the self-calibration method of Eq. 6.3.	68
6.11	Simulated average residual width as a function of the track distance from the wire (left) and residual distribution of (reconstructed-true) wire distance. The bold line is the smoothing polynomial.	69
6.12	As in Fig. 6.11 with a constant fraction electronic discrimination.	69
6.13	Standard deviation corresponding to the residual width resolution of Fig. 6.11 (left).	69

List of Tables

1.1	Experimental requirements and operation modes of HESR	5	5.1	List of straw settings and charge load during the beam test. The last column shows the normalized gas gain reduction in the irradiated straw region with a measurement resolution of about 2%. The aging intervals give the minimum and maximum gain reductions, e.g. 0–7% means that at least one straw showed no gain reduction and one a maximum of 7%.	56
1.2	Maximum achievable cycle averaged luminosity for different H ₂ target setups	8	1	Inclination, coordinates and length of straw modules from individual double layers of the tracking stations. The coordinates x , y , z describe position of centers of modules (defined in Fig. ??) in right-handed coordinate system with the origine located in the nominal beam-target crossing point, the y -axis oriented in the vertical direction and the z -axis pointing along the beam direction.	79
1.3	Expected luminosities for heavier nuclear targets at $\overline{\text{PANDA}}$	9	2	Dimensions of rectangular openings in the tracking stations for the beam pipe.	81
1.4	Estimate on the expected event rates at $\overline{\text{PANDA}}$	10			
2.1	Mean thickness in radiation lengths of the different straw tube components. The number for the gas mixture is evaluated at 20° and 2 atm.	27			
2.2	Properties of different gases and gas mixtures. Z and A are charge and atomic weight, for molecules the total number have to be taken, N_p and N_t are the number of primary and total electrons per cm, respectively, E_x and E_i are the excitation and ionization energy, respectively, W_i is the average energy required to produce one electron-ion pair in the gas, $(dE/dx)_{mip}$ is the most probable energy loss by a minimum ionizing particle and X_0 is an radiation length. For gas mixtures, weighted average value have to be taken.	28			
4.1	Straw electrical properties.	36			
4.2	Front end electronics requirements.	36			
4.3	Main parameters of the new straw tube front-end readout chip (see text for more details).	37			
4.4	Basic technical parameters of the CARIOCA-10 chip.	41			
4.5	Technical characteristics of the prototype preamplifier/discriminator board - version-2.	41			